FINITE ELEMENT ANALYSIS OF CONCRETE STRUCTURES SUBJECTED TO ALKALI-AGGREGATE REACTION

FINITE ELEMENT ANALYSIS OF CONCRETE STRUCTURES SUBJECTED TO ALKALI-AGGREGATE REACTION

Wenfei Wu, B.E.

A Thesis

Submitted to the School of Graduate Studies

in Partial Fulfillment of the Requirements

for the Degree

Master of Engineering

McMaster University

MASTER OF ENGINEERING (1996)   McMASTER UNIVERSITY

(Civil Engineering)   Hamilton, Ontario, Canada

TITLE: FINITE ELEMENT ANALYSIS OF CONCRETE

                              STRUCTURES SUBJECTED TO ALKALI-AGGREGATE

                              REACTION

AUTHOR: Wenfei Wu

                              B.E. (Tongji University)

SUPERVISOR: Dr. S. Pietruszczak

NUMBER OF PAGES: 197, xvii

ABSTRACT

The alkali-aggregate reaction was first reported in 1940 as a cause of severe cracking in some concrete structures. It is only in recent years that papers have been published dealing with the effects of AAR on the performance of structures. This thesis outlines a methodology for numerical simulation of the response of concrete subjected to continuing AAR. First a constitutive model is presented based on the framework proposed by Pietruszczak (1996). The formulation incorporates an assumption that the rate of expansion depends on the confining pressure, the age of concrete and the temperature. The progress in the reaction is coupled with the degradation of mechanical properties, in particular the elastic modulus and the compressive and tensile strengths. Subsequently, the procedures for generating finite element models are described, including geometric modeling, mesh generation techniques, graphical representation of the results and interfacing between pre- and post-processor and the finite element solvers. The numerical analysis, undertaken in this thesis, pertains to the Beauharnois Powerhouse, situated in Quebec, Canada. The powerhouse has been experiencing problems related to a continuing expansion of concrete due to AAR since the early 1960's. The progressive formation of macrocracks and the volumetric expansion in concrete has caused operational problems, such as the reduction in clearance between turbine runner blades and throat rings. In this study, typical structural units of the Beauharnois Powerhouse were selected for the numerical analysis. The AAR constitutive model was applied in a finite element framework. Mechanical properties of concrete were carefully evaluated based on available

experimental data. Simulations were focused on the deformation and the time history of progressive macro/microcracking due to continuing reaction. Structural responses under isothermal as well as non-isothermal conditions were simulated. The results of the numerical analyses were then compared with in-situ measurements.

ACKNOWLEDGEMENTS

TABLE OF CONTENTS

List of Figures

Chapter 1

Chapter 2

Chapter 3

Chapter 4

Chapter 5

Chapter 1

Introduction

1.1 General Remarks

Portland cement concrete may deteriorate due to chemical reactions between alkali substances and certain types of aggregates. The alkali-aggregate reaction (AAR) generates expansive gels, which destroy the concrete matrix. The reaction may cause severe damage in typical concrete structures (e.g., misalignment of structural elements, macro/ microcracking, etc.).

Since the discovery of AAR in the 1930's, an increasing number of concrete structures have been found suffering from durability problems due to AAR (Figures 1.1, and 1.2). Presently, the situation is quite alarming as there is virtually no country which can claim immunity from AAR-induced concrete deterioration in existing structures. Over the last few decades, an extensive interdisciplinary research has been carried out. One of the important aspects in the research pertains to the effect of AAR on the mechanical response of existing structures, in particular to what extent a further progress in the reaction threatens the stability of these structures.

Since the 1980's, the research has focused on explaining the AAR mechanisms and on the evaluation of variety of factors influencing the progress of the reaction. These factors include confining pressure, temperature, relative humidity, etc. The modeling of AAR at the structural level started in the early 1990's. At the initial stage, AAR expansion was modeled as an equivalent thermal expansion (Davie *et al.*, 1992; Tanner 1992; De

Beauchamp 1992; Shawinigan Lavalin Inc. 1992; Yeh *et al.*, 1993; Newell *et al.*, 1994). In these research programs, concrete was considered as a linear elastic material. Only a few attempts have been made to rationalize the effect of influence factors (e.g., Tanner, 1992) and no effort has been made to properly describe the degradation of material properties.

Recently, due to the deeper understanding of AAR, several constitutive models have been developed. Cervera *et al.* (1990, 1992) presented two similar computational models, which assumed that AAR expansion is related to water intrusion through the damaged areas. Concrete was described using an elastic-fracturing constitutive model and an isotropic continuum damage model including visco-elastic effects, respectively. Leger *et al.* (1994) proposed a methodology based on the assumption that concrete expansion is proportional to the compressive stress state, temperature, moisture, and the reactivity of the concrete constituents. Pietruszczak (1996) presented a methodology for a description of the mechanical manifestations of AAR. The approach is similar to the description of creep or thermal expansion phenomenon. The degradation of mechanical properties has been assumed to be coupled with the progress in AAR, and has been described within the framework of elastoplasticity.

Despite these efforts, many aspects of AAR are still not well-understood. Thus, it is difficult to consider all the effects of AAR in a single constitutive model. Presently, each model considers only some of the most important factors. This is largely due to the lack of a systematic testing.

1.2 Purpose and Scope

The purpose of this thesis is to study the response of concrete subjected to AAR at both the constitutive model and the structural response levels. In the constitutive model, a variety of influence factors are taken into consideration. The degradation of concrete is assumed to be coupled with the progress in AAR. Finite element simulations based on isothermal condition and a given seasonal temperature variation are carried out. The thesis is arranged in the sequence, as outlined below.

In Chapter 2, the experimental results on AAR are extensively reviewed. Expansion rates obtained from laboratory test and outdoor exposure test are compared. The effects of material degradation are discussed. A variety of influence factors, including temperature, confining pressure, relative humidity, alkali content, etc, are carefully studied.

Chapter 3 presents the formulation of a constitutive model following the framework established by Pietruszczak (1996). Numerical examples are provided illustrating the influence of the reaction on the mechanical characteristics of the material. The finite element formulation and the solution procedures are also discussed.

Chapter 4 describes the techniques for generation of finite element models, including geometric modeling, mesh generation and computer graphics. Interface operation schemes and programs are given.

The applications of finite element modeling are provided in Chapter 5. Two components of Beauharnois structural complex, situated in Quebec (Canada), are analyzed. First, the right wing dam is modeled assuming isothermal conditions. Secondly, the same dam is

analyzed with a provision to account for seasonal temperature variations. The influence of the foundation stiffness is also studied and the results from the above two models are compared. Later, the water intake structure is analyzed using as a three-dimensional model and assuming isothermal condition. Parametric study for each model is carried out.

Finally, some conclusions from this study and recommendations for further research are presented in Chapter 6.

Chapter 2

Alkali-Aggregate Reaction in Concrete Structures

2.1 Introduction

Concrete may deteriorate due to expansive reactions between alkali substances and certain types of aggregates. The alkalis are mainly present in the cement, but it has also been found that some aggregates contain minerals which contribute alkalis by internal reactions and so cause an increase in alkali content. The reactive aggregates contain silica, which reacts directly with alkali solution in concrete. This reaction is referred to as alkali-aggregate reaction (AAR).

In the 1930's some unexplained cracking and expansion of concrete was observed in a number of structures in California region, causing considerable concern. Structures affected included several school buildings, bridges, pavements and a sea wall. In the late 1930's, Stanton noticed by chance that a mortar cylinder, retained in a tin container for one year, was covered with blotches fringed with a white efflorescence, which were subsequently found to be sodium carbonate. In a short time the entire specimen became covered with cracks. Stanton then showed that mortar samples of local Oro Fino sand and the cement used in the affected structures always showed excessive expansion within 28 days when placed in air-tight cans, whereas those made using another source of sand or another source of cement did not. It was established that expansion was related to the alkali content of the cement and that the deterioration occurring in some concrete structures was caused by an alkali-silica reaction (ASR),the reacting siliceous constituent

being opaline silica. From tests on mortar bars with a cement content of over 600 kg/m^3, Stanton concluded that cracking and expansion due to ASR did not occur when the acid soluble alkali content of the cement, expressed as equivalent sodium oxide content, was less than 0.60% by mass.

Stanton's paper, which was the first one on AAR published in 1940, incited considerable interest. Since then, an increasing number of concrete structures, all over the world, have shown the evidence of durability problems due to AAR. The inherent factors of AAR are the available alkali content in the cement matrix and silica content in the aggregate. The sufficient environmental condition for AAR is a high moisture content. The hydration reaction of alkali in cement and silica in aggregate generates expansive gels, which cause concrete deleterious expansion. Consequently, most AAR damaged structures are dams, bridges, pavements, foundations and other structures subjected to high moisture conditions.

The remediation of AAR damaged structures is usually very costly. For example, the Maentwrog dam in Snowdonia National Park, UK, has experienced vertical cracking in the arch close to the abutments due to AAR in the concrete. This damage resulted in building a new dam immediately downstream for replacement (Anon, 1989). The Hiwassee Dam in North Carolina, US was built in 1930 by Tennessee Valley Authority (TVA). Cracks had been found in this dam in 1939. Due to AAR, concrete growth has squeezed the spillway opening and caused significant structural cracking in the abutments. By the 1980's, the spillway section had permanently closed 3-4 in. Seasonal opening and closing movement had reached 2-3 in. Static and seismic analyses showed that the upper

portion of the dam could slide and fail in a low-magnitude earthquake. This prompted TVA to cut four slots completely through the concrete in an attempt to keep the floodgates operational. The total cost of the remediation was estimated at US$ 4 million (Newell *et al.*, 1994).

2.2 Mechanism of AAR in Concrete Structures

The essential conditions for AAR are a sufficient alkali content in the cement matrix and high humidity environment. The reaction mechanism can be summarized as follow (Hobbs, 1984; Shayan *et al.*, 1992):

1. In high relative humidity condition, alkali in cement is dissolved in pore moisture. A high concentration of alkali hydroxides is developed in pore solution. The alkali in the solution reacts with the silica in aggregate.

2. The reaction of alkali and silica produces the expansive alkali-silica gels. The gels absorb water and expand, causing internal stresses in the concrete. The alkali-silica gel is not as stiff as the normal cement paste. Thus, the gels destroy the concrete matrix bonds, and cause fracturing of aggregates and the adjacent cement paste. At the same time, the differential expansion of the interior and the exterior of the concrete structure can result in formation of surface microcracks.

3. Cyclic loads, for example daily and seasonal temperature changes, cause fatigue microcracking in the weakened matrix of the concrete and enhance the surface microcracking. The progress of fatigue cracking allows penetration of moisture into the concrete structure.

4. The AAR process is enhanced due to the penetration of moisture into the concrete and leads to further expansion and cracking. Moreover, a favorable environment is produced for the redistribution of alkali ions.

Evidence from numerous studies has shown that there is a certain proportion of silica in reactive aggregate causing a maximum expansion in concrete. This proportion of reactive material is referred to as the pessimum proportion. Similarly, there is a pessimum proportion of alkali content in concrete which produces maximum expansion.

The concrete contains a fixed concentration of alkali but a range of concentrations of reactive aggregate constituent. The alkali-aggregate reaction will proceed and produce expansion until either the reactive aggregate constituent or alkali is depleted. For the concrete containing aggregate with a lower percentage of reactive material, the silica is used up with consequent changes in the ratio of alkali to reactive constituent. Similarly, with higher concentrations of reactive aggregate, it is the alkali that is used up with the ratio changing in the opposite direction to the first case. Figure 2.1 illustrates the simplest case when the reaction rate and expansion are being controlled by the ratio of alkali to silica or silica to alkali, both concentrations being equally important for the reaction.

If the silica in the reactive aggregate has a higher rate of removal of alkali, each unit increase in silica will remove a large proportion of alkali during the reaction. This will effectively move the pessimum to the left as illustrated in Figure 2.2.

2.3 Expansion Rate of AAR

In order to obtain AAR expansion data, numerous tests have been carried out. The test specimens are either mortar bars or concrete cores taken from the damaged structures. The behavior of small concrete specimens tested under laboratory conditions is different from that of comparable site concrete. Laboratory test results indicate that the expansion tends to approach a steady low gradient as the concrete age increases. However, outdoor exposure tests show that the expansion continuously increases in contrast to the laboratory test results. Figure 2.3 (Kennerley *et al.*, 1981) compares the results for specimens with indicated alkali contents (kg/m^3), subject to continuous moist curing (M) in laboratories and outdoor exposure (E). The reason for the difference is that under outdoor exposure conditions, numerous factors influence the process of the reaction. For example, seasonal temperature change, different humidity conditions, freeze and thaw cycles, etc., can significantly affect the rate of expansion.

2.4 Degradation of Mechanical Properties

The degradation of mechanical properties of concrete, particularly the elastic modulus as well as the compressive and tensile strengths, comes mainly from the mechanical damage to concrete. During the continuing AAR, the expansive alkali-silica gels destroy the concrete matrix bonds and cause fracturing between aggregates and the adjacent cement paste. The degradation is commonly expressed as a function of time. To assess the long term effect of AAR on a structure, it is necessary to establish the relationships of each mechanical property with time. These relations are derived based on results of laboratory tests. It should be noted that small unconfined specimens generally exhibit much larger

degradation in mechanical properties than those of the actual concrete in structure, where triaxial confinement exists (Jones *et al.*, 1994; Imai *et al.*, 1986).

2.4.1 Degradation of Compressive Strength

The reaction between alkali solution and silica in the aggregate results in a progressive decrease of the concrete compressive strength. The degradation of compressive strength continues during the AAR process.

A number of tests have been performed to establish the relationship between compressive strength and time, as well as other influential factors. Swamy *et al.* (1986) recorded the time history of compressive strength in several concrete specimens subjected to AAR as shown in Figure 2.4. Based on laboratory tests, Pleau *et al.* (1989) pointed out that the maximum loss in strength at 38°C is about 45% after 1 year, Figure 2.5. The results obtained by Nixon *et al.* (1985) indicated that the temperature can significantly affect the rate of compressive strength degradation. It can be seen in Figure 2.6 that at 38°C the compressive strength starts to decrease after 6 month period, while at 20°C a marginal increase is recorded. The relation between the degradation of compressive strength and the expansion was also investigated by Swamy *et al.* (1985), Figure 2.7.

In general, the rate of compressive strength degradation depends on the type of aggregate containing silica. The temperature will influence the rate of AAR. Thus, the rate of alkali-silica gel production and microcracks development are also influenced by temperature. As a result, the rate of compressive strength degradation is influenced by the temperature.

2.4.2 Degradation of Tensile Strength

The gel produced by AAR absorbs sufficient water and expands resulting in the destruction of the bonds between aggregate and cement matrix and fracturing of the aggregate and the bordering cement paste. This causes continuous microcracks development. The result is that the concrete tensile strength is decreased dramatically. Furthermore, the tensile strength degradation will enhance microcracking.

In order to establish the relation between the strength degradation and time, numerous tests have been performed. The tests carried out by Nixon *et al.* (1985) indicate that the effect of AAR on tensile strength is more pronounced than on the compressive strength, as shown in Figure 2.6. It is noteworthy that when the expansion rate becomes higher, the degradation of tensile strength slows down. Figure 2.8 shows the relationship between tensile strength and time (Swamy *et al.,*1985, 1986). Similar test, at 38°C, were performed by Pleau *et al.* (1989) and the results are given in Figure 2.9. The relationship between degradation of tensile strength and expansion was also investigated by Swamy *et al.* (1985), as shown in Figure 2.10.

Generally, the rate of tensile strength degradation is influenced by temperature, which affects the rate of AAR. It can also be seen from the figures mentioned above that tensile strength degradation is usually complete during the early stage of AAR. Further, tensile strength is much more affected than the compressive strength (Blight *et al.,*1981).

2.4.3 Degradation of Elastic Modulus

Elastic modulus degradation is a very influential factor in structural deformation. Since the rate of AAR varies with temperature, the rate of elastic modules degradation is also influenced by temperature.

The results given in Figure 2.11 (Pleau *et al.* , 1989) show the evolution of elastic modulus with time for concrete stored in air at 100% R.H. and 38°C. The results indicate that the elastic modulus exhibits approximately 50% reduction between 4 and 12 weeks. A further decrease follows up until 1 year, when 65% reduction has been achieved. At this point, a relative equilibrium is reached. Charlwood (1994) used an effective modulus E_{eff} to represent the elastic modulus degradation in a finite element analysis of an AAR-affected structure. $E_{eff} = E_{ci} / (1+\phi)$, where E_{ci} is the initial elastic modulus, and ϕ equals 2.5 for long-term prediction and 0.2 for short-term, respectively.

Degradation of elastic modulus is usually complete within the early stage of AAR. The rate of degradation and the percentage of drop may vary for different materials.

2.5 Factors Influencing the Reaction

2.5.1 Influence of Temperature

In the last two decades, a number of tests have been performed to establish the relation between expansion rate and temperature. Most of the tests were carried out in laboratories, where the test conditions, such as temperature and humidity, can be controlled. The others were conducted under outdoor exposure, where the conditions

were very complicated but more close to reality. It should be noted that all outdoor tests were carried out on different materials, which came from different locations, contained different alkali substances with different concentrations. To shorten the test periods, different pretreatment techniques were used in each test. Therefore, it is not possible to compare these results in quantitative terms. Furthermore, most tests were conducted at one constant temperature. Only a few tests were performed under varying temperature conditions, from which a relationship between expansion and temperature may be established.

The rate of alkali-silica reaction, which directly affects expansion, is proportional to soluble alkali content. The lower the temperature, the lower the solubility of alkali. Therefore, at lower temperature, the reaction rate is slow. As the temperature increases, the alkali solubility and concentration increases correspondingly , thus the reaction rate speeds up. As the temperature exceeds a certain value, the solubility is decreased due to the over saturation of alkali contents. As a result, the reaction rate slows down again. This critical value of temperature, referred to as pessimum temperature, is identified to be approximately 40°C as shown in Figure 2.12 (Nishibayash *et al.*, 1992).

The results of numerous studies indicate that two main types of mechanical response can be identified.

Type I: The expansion is directly proportional to the temperature which is below the pessimum temperature. This type of response is typical of materials found all over the world. As an example, Figure 2.13 shows the expansive behavior of concrete specimens

containing limestone, which is widely used as concrete aggregate in Quebec, Canada. It can be seen that the expansion at 38°C is higher than that at 23°C (Pleau *et al.*,1989).

Type II: At high temperature, the expansion is initiated early and develops rapidly, but as the reaction continues, the rate of expansion slows down as shown in Figure 2.14 (Diamond *et al.*,1981). By contrast, expansion at lower temperature is initially slow, but eventually reaches the same level and then exceeds the expansion attained at the higher temperature. These types of materials were reportedly found in the UK and Japan (Diamond *et al.*,1981; Nakano *et al.*,1984; Wood *et al.*,1986; Nishbayashi *et al.*,1989; ISE, 1992).

2.5.2 Influence of Relative Humidity

Alkali aggregate reaction requires water to proceed. High relative humidity is a necessary condition to maintain the reaction and the expansion process. The moisture can be delivered by environmental humidity or by external water flow. During the reaction, water performs two roles: i) solutes alkali, then carries alkali cations and hydroxyl ions; ii) the hydrostatic gel absorbs large amounts of water to swell and develop pressures.

Concrete, even in dry condition, will retain pore fluids so that the relative humidity within the concrete will remain at 80-90% except at the outer layer of the structure, which may be a few centimeters thick (Stark, 1985).

Experimental investigations indicate that the effects of alkali-silica reaction vary with the percentage of the relative humidity. The amount of absorbed water in the gel depends directly on the relative humidity. This is shown in Figure 2.15, which indicates that the

water content in gel increases rapidly when relative humidity is higher than 70%. A typical relation between expansion and relative humidity is shown in Figure 2.16. It can be seen that below 70% R.H. the expansion is negligible, but above 80% R.H. the expansion increases dramatically. So far there is no agreement on the minimum humidity level to maintain AAR. In a report by the Institution of Structural Engineers (1992) the minimum moisture content below which no significant expansion occurs is stated to be 75% R.H. of the surrounding environment. Below 80% the expansion and the crack growth occur very slowly, whereas in the range of 90% to 100% R.H. AAR expansion and cracking develop most rapidly. The ASR development starts clearly at moisture levels between 85 and 90% R.H. The critical humidity range for ASR to develop is identified by a Norwegian report (Rotter, 1995) as 85% to 95% R. H. Other investigations (Gudmundsson *et al.* 1983; Nilson 1983) suggest the critical moisture level to be about 95% R.H. Olaffson (1987) suggested a critical moisture level which depends essentially on temperature.

2.5.3 Influence of Confining Pressure

The confining stresses can significantly influence the expansion and cracking. Figures 2.17 to 2.19 show results obtained for mortar bars subjected to confining pressure and stored at 20°C. The data shown in Figure 2.17 correspond to the case when the mortar bars were subjected to AAR at different levels of confining stresses. It is evident here that the expansion decreased dramatically at high confining stresses. If the confining pressure was applied to the mortar bars after a long period of free expansion, say, 112 days as shown in Figure 2.18, further expansion was prevented. In contrast, if the applied confining stresses were removed after 111 days, as shown in Figure 2.19, substantial expansion was

observed. This indicates that expansion tests carried out on cores taken from affected structures may not yield reliable information on potential further expansion of the concrete within the structures. The affected cores, once taken from the structure, can not be assumed to be representative of the concrete in the original structure. For this reason, Hobbs (1988) considered that measurements of strength and elastic modulus made on affected cores may not give values representative of the concrete in the structure.

2.5.4 Influence of Alkali Content

Generally, increasing the alkali concentration will enhance the alkali-aggregate reaction. To make the expansion rates for different alkali-aggregates comparable, the alkali content is commonly expressed as equivalent Na_2O concentration. The alkalis are mainly presented in the cement. Usually an ordinary Portland cement contains 0.4% to 1% equivalent Na_2O, depending upon the chemical composition of the raw materials. Additional external sources of alkali could be supplied by aggregate grains or external water, particularly sea water (Olafsson, 1989). Varying the alkali concentration changes the hydroxyl concentration of the pore solution in concrete.

When alkali-silica ratio is lower than the pessimum reactive aggregate content, the expansion is proportional to the alkali content. A typical relationship between expansion and the age of the concrete is shown in Figure 2.20 (Hobbs, 1984). It is obvious that when the alkali content is lower than a certain critical level, the expansion stops. A number of tests have been carried out to determine this value for materials from different regions.

Hobbs (1984) reported the results of 200 days expansion tests involving a series of specimens. All of the results were obtained on specimens tested approximately at their critical alkali-silica ratio. The results indicated that none of the concrete prisms cracked due to AAR when alkali content was below 4 kg/m³. However, a sharp increase in expansion was observed when the alkali content was above 4 kg/m³, as shown in Figure 2.21. A 5 year expansion test carried out in New Zealand indicated that alkali contents in excess of 5 kg/m³ were necessary for deleterious expansion to occur, Figure 2.22 (Kennerley *et al.*,1981). A similar type of test carried out in Germany (Bonzel *et al.*,1973; Dahms, 1976; Kordina *et al.*,1981) and Australia (Vivian, 1950; Davis, 1957) led to the conclusion that significant damage will occur when the alkali contents levels exceed 5 kg/m³ and 2 kg/m³, respectively.

2.5.5 Influence of Other Factors

Wetting-drying cycles

It has been reported that there is a noticeable difference in the degree of surface damage between the weather and lee sides of the same structure. In general, exposed parts are more severely cracked and damaged by the effects of AAR than the parts protected from the weather. The reason is that cyclic wetting and drying of an exposed surface contributes to the movement of the alkalis (Poole, 1992). Due to moisture evaporation on the surface, the process of alkali ion migration is coupled with the movement of moisture in the pore structure of concrete. The driving force is believed to be the humidity gradient. Wetting-drying cycles cause alkali ions to migrate (Xu *et al.*,1993). As many large concrete

structures are partially buried in the ground with top surfaces exposed to the atmosphere, e.g. dams, foundations, etc., wetting-drying cycles could be a significant factor influencing alkali-aggregate reaction.

Influence of freeze-thaw cycles

It has been noted that AAR damage mainly occurs in cold regions, implying that the influence of freeze-thaw cycles may be an important factor. Alkalis ions move from warm parts to the freeze-thaw surfaces. Laboratory tests by Xu *et al.* (1993) showed that after 270 freeze-thaw cycles in 90 days, alkali concentrations increased by 43% on the freeze-thaw surface and decreased by the same percentage on the warm surface. The driving force of alkali ion migration in freeze-thaw cycles is considered to be the humidity gradient. Because the vapor pressure of ice is less than that of warm water, moisture moves from the high humidity parts to the frozen area. Due to the low water vapor concentration in the frozen area, ice would be sublimated out of the frozen surface. The interaction between freeze-thaw cycles and alkali-aggregate reaction makes the problem more complex as a coupled problem. The expansion and cracking caused by AAR may accelerate deterioration by frost. On the other hand, the cracking caused by frost is accelerated by the diffusion of ions. Furthermore, the migration and concentration of ions are also factors subject to interaction.

There are other factors influencing AAR, e.g. aggregate particle size (Hobbs, 1988), electric current (Xu *et al.*, 1993), air entrainment (Hobbs, 1988; Rotter, 1995) and so on, which will not be detailed here.
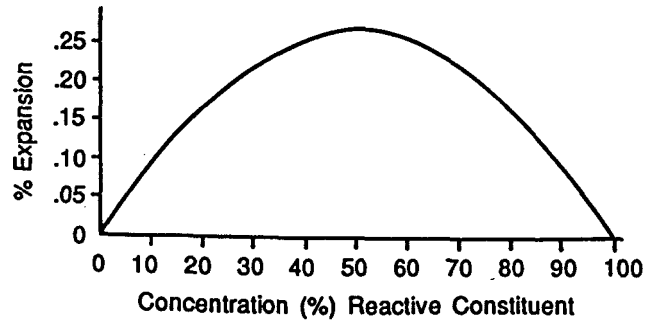
Figure 2.1   Graphical representation of a simple pessimum proportion relationship (Ozol, 1975).
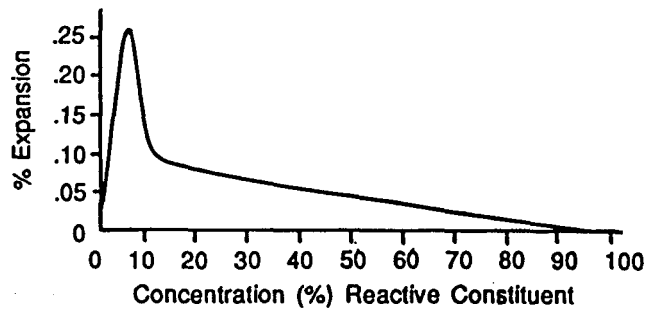
Figure 2.2 The pessimum proportion model showing the effect of a high alkali removal rate (Ozol, 1975).
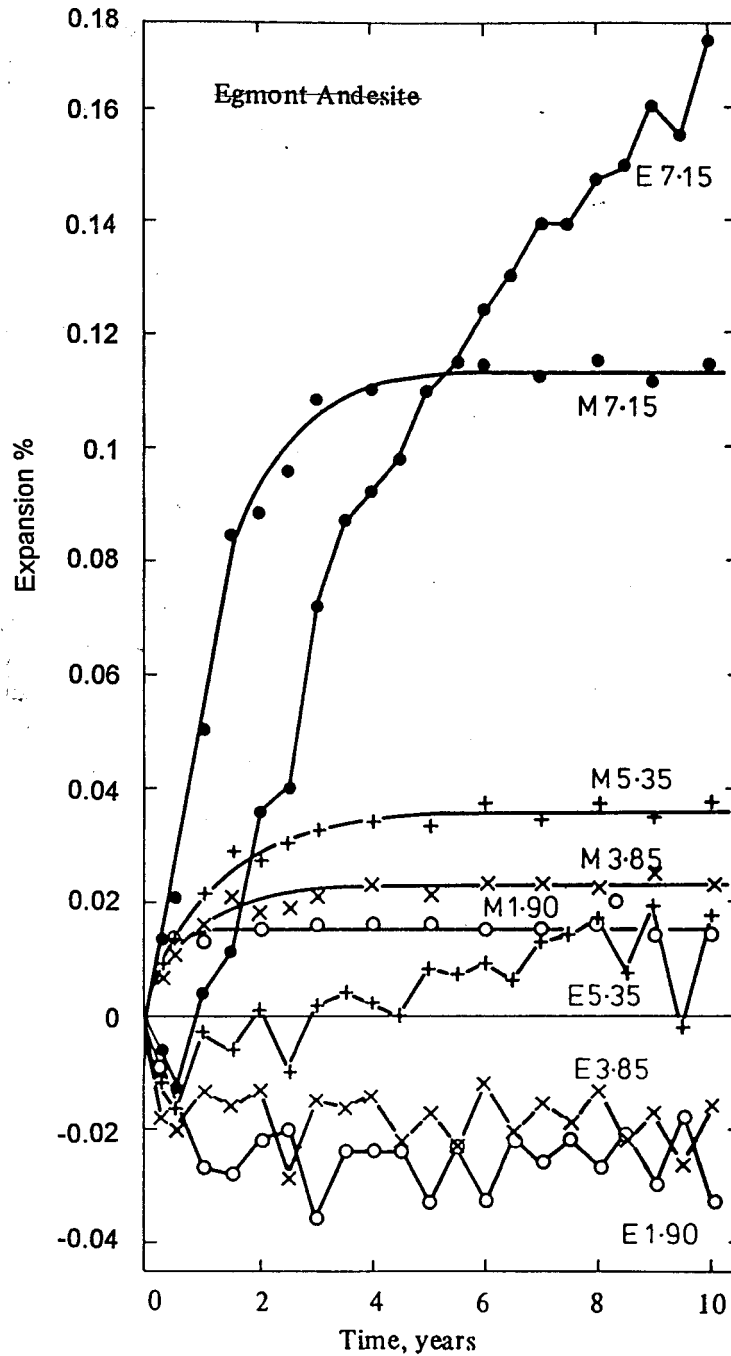
Figure 2.3 Comparison of concrete expansion behavior with indicated alkali contents in kg/m³ subject to continuous moist curing in laboratories (M) and outdoor exposure (E) (Kennerlay *et al*, 1981).
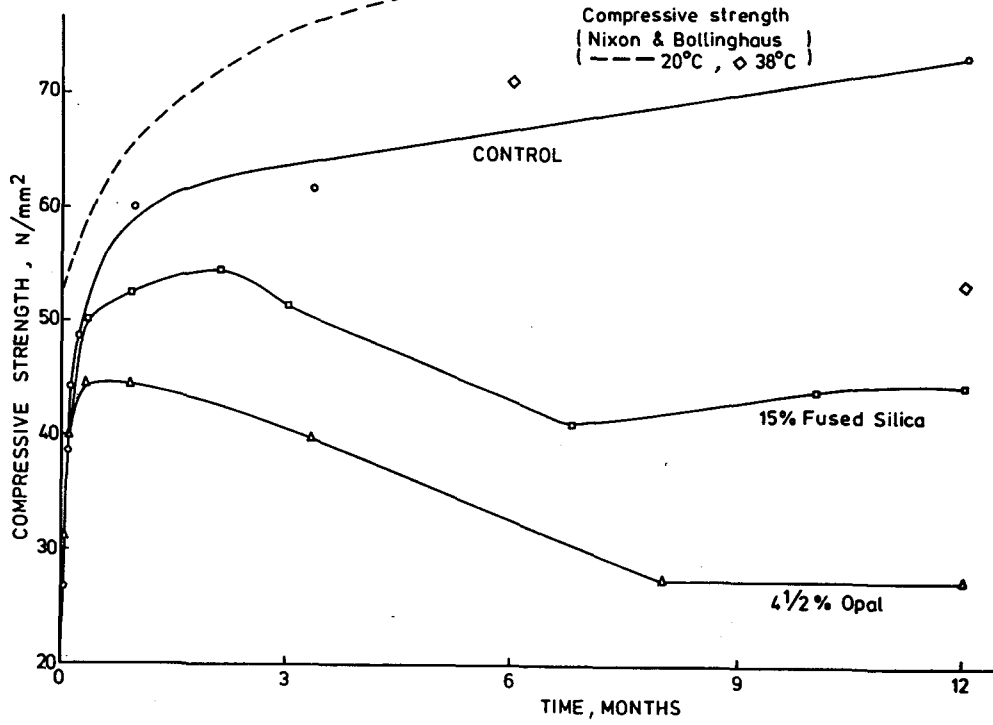
Figure 2.4 Time history of compressive strength degradation (Swamy *et al*, 1985).
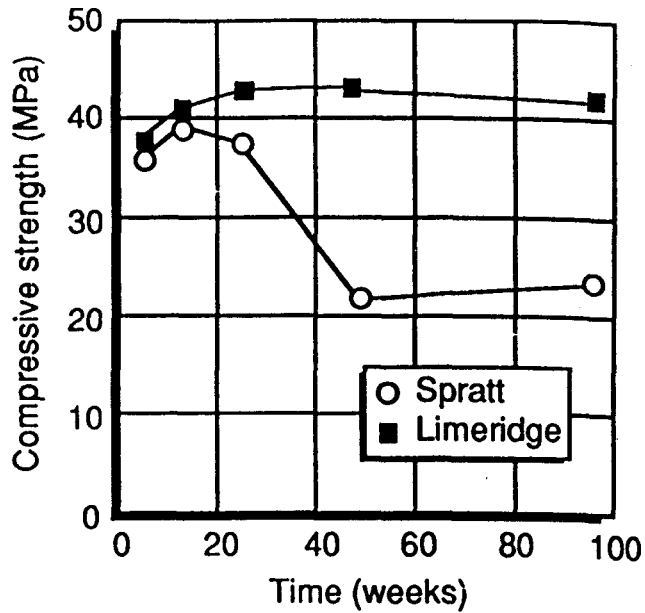
Figure 2.5 Compressive strength vs. time for concrete stored at 38°C (Pleau *et al.*, 1989).
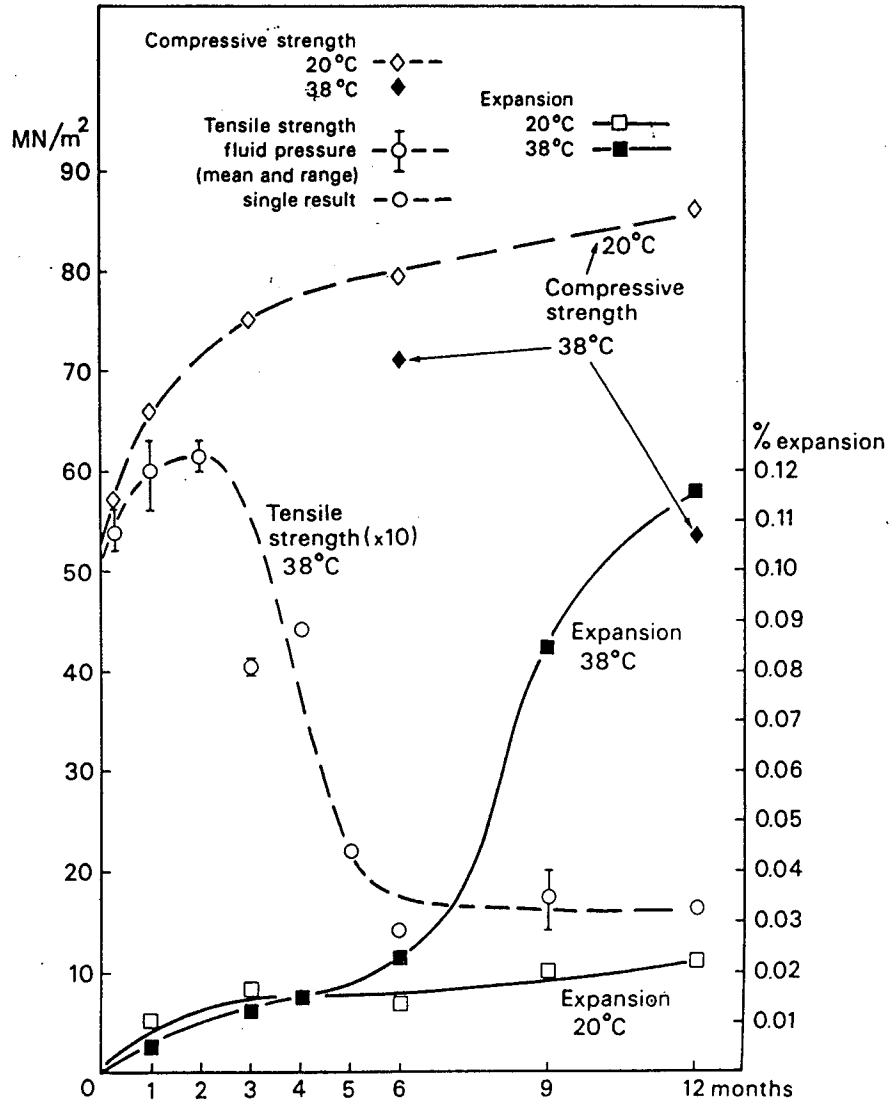
Figure 2.6 Compressive and tensile strength degradation and expansion at 20°C and 38°C (Nixon *et al*, 1985).
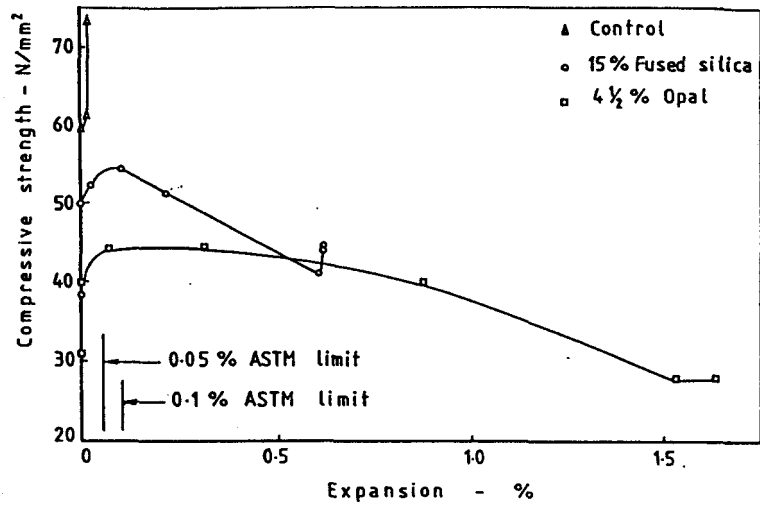
Figure 2.7 Compressive strength vs. expansion (Swamy *et al*, 1985).
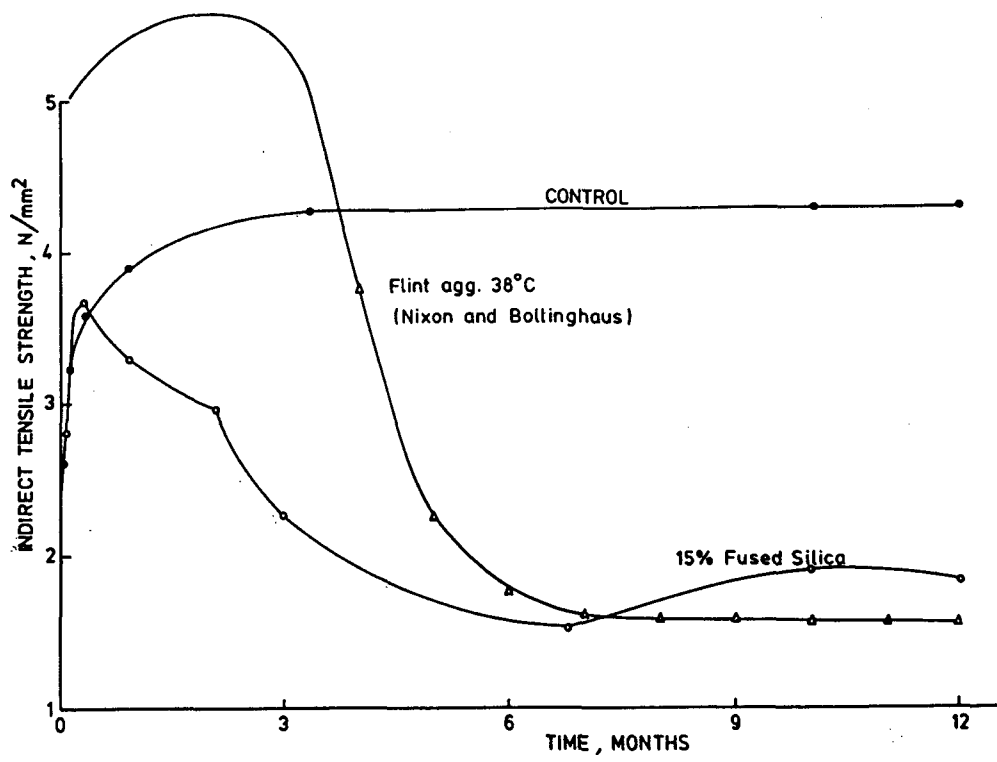
Figure 2.8 Time history of tensile strength degradation (Swamy *et al*, 1985).
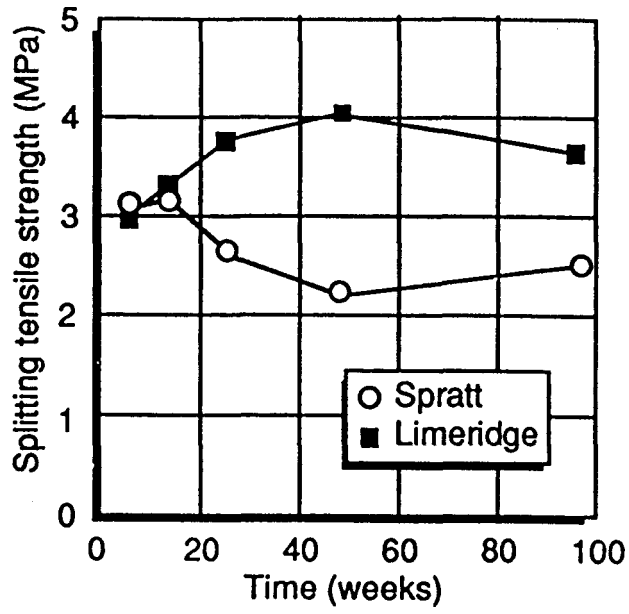
Figure 2.9 Tensile strength vs. time for concrete stored in air at 38°C
(Pleau *et al*, 1989).
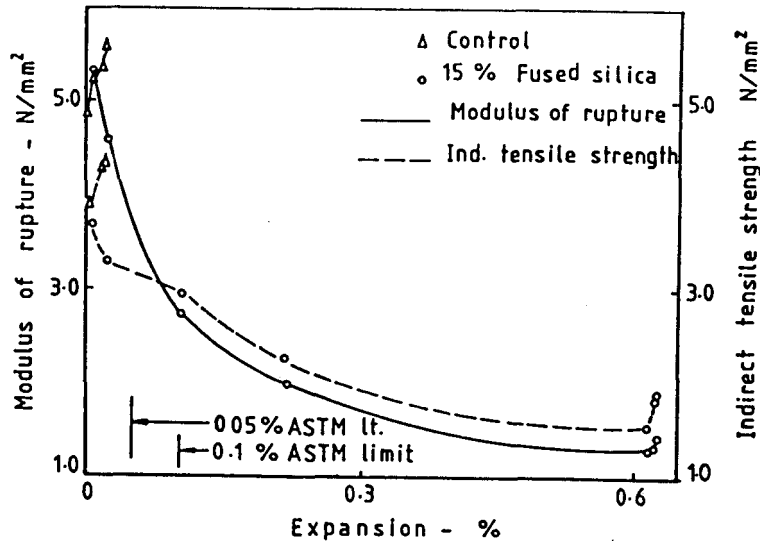
Figure 2.10 Tensile strength vs. expansion (Swamy *et al*, 1985).

Modulus of elasticity (x10³ MPa)

50

40

○ Spratt
■ Limeridge

30

20

10

0

0   20   40   60   80   100

Time (weeks)
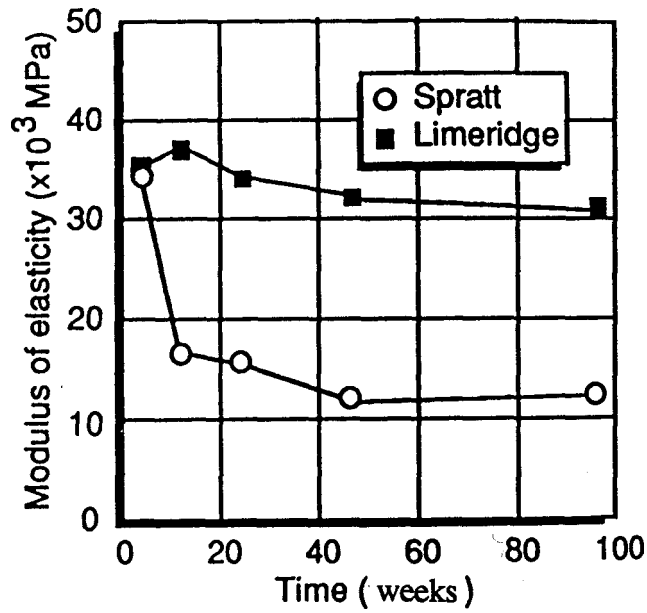
Figure 2.11 Degradation of elastic modules for concrete stored in air at 38°C
(Pleau *et al*, 1989).

Ordinary portland cement with
total alkali content 1.2% Na_2O equiv.

Expansion (%)

0.3

0.2

0.1

0

40°C

60°C

20°C

5°C

2   4   6   8   13   17

Age (weeks)
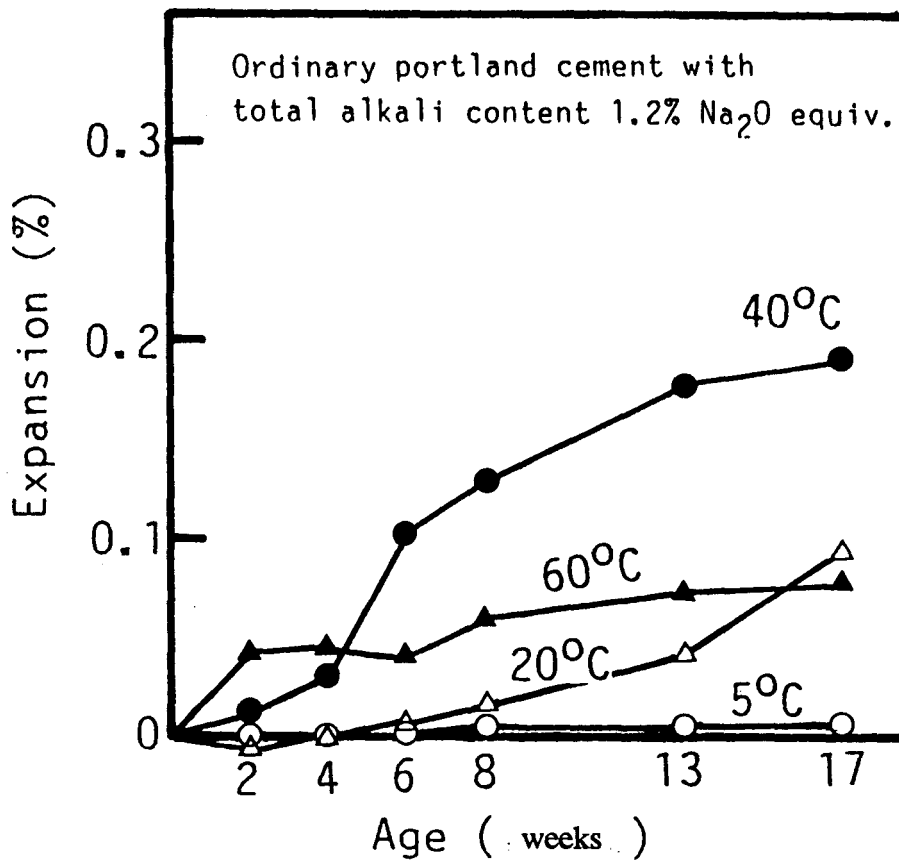
Figure 2.12   Time history of Alkali-aggregate expansion at different temperatures
(Nishibayash *et al.*, 1992).
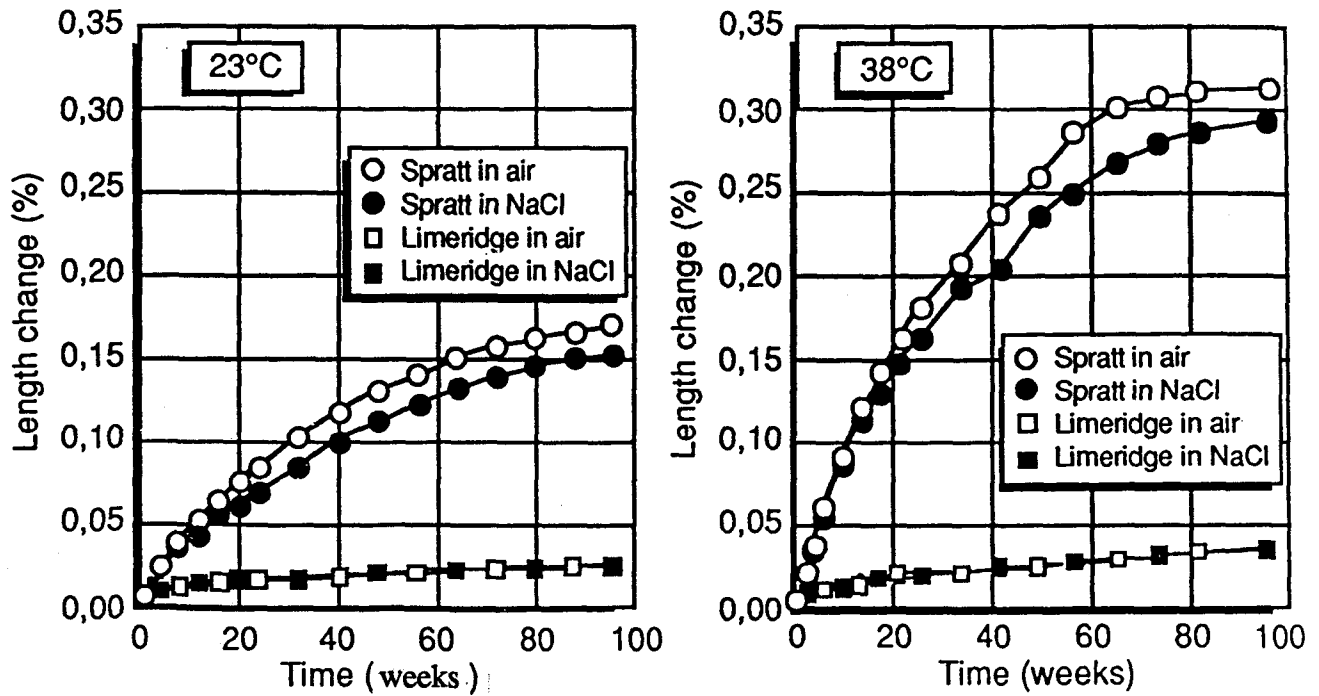
Figure 2.13 Axial expansion of concrete specimens vs. time at 23°C and 38°C (Pleaau *et al*, 1989).
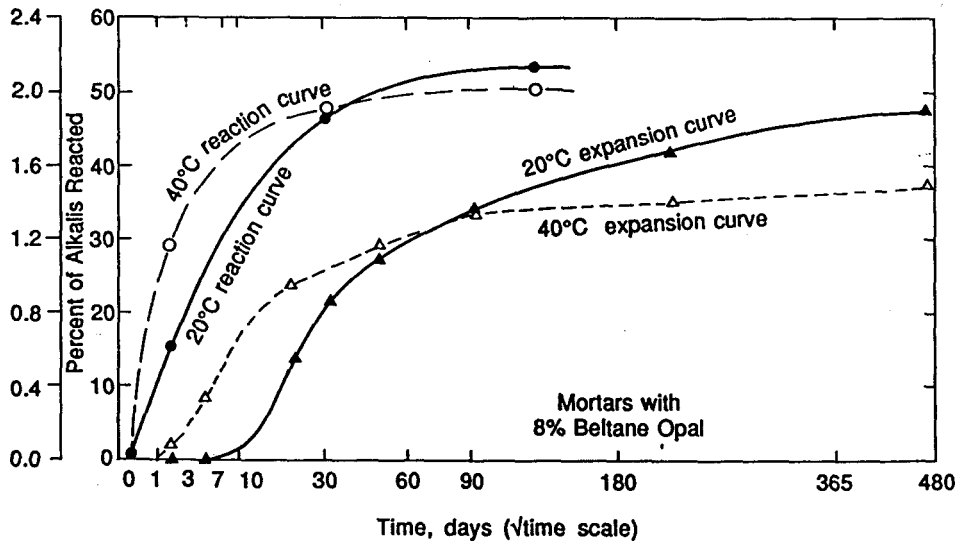
Figure 2.14 Comparison of expansion time at 20 °C and 40 °C (Wood *et al.*, 1984).
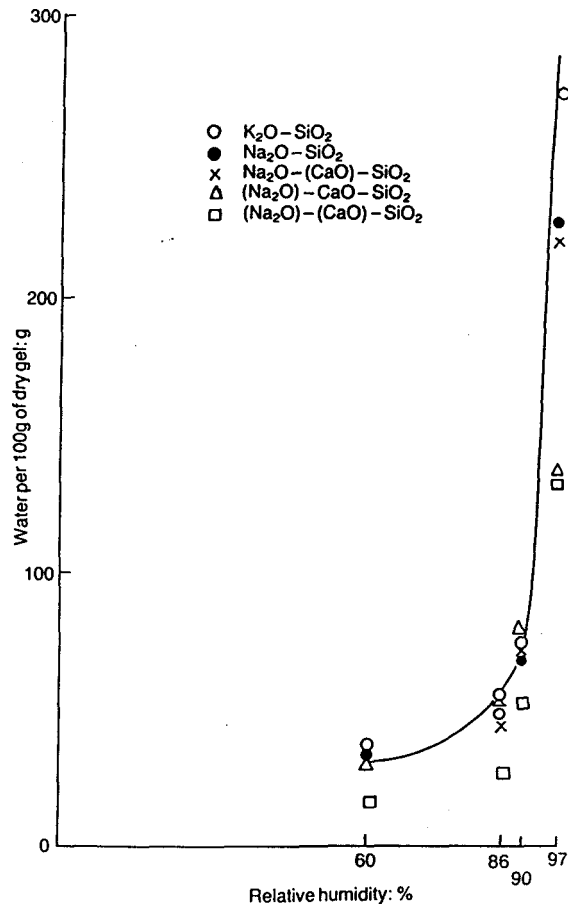
Figure 2.15 Relationship between water content in gels at equilibrium and relative humidity (Krogh, 1975).
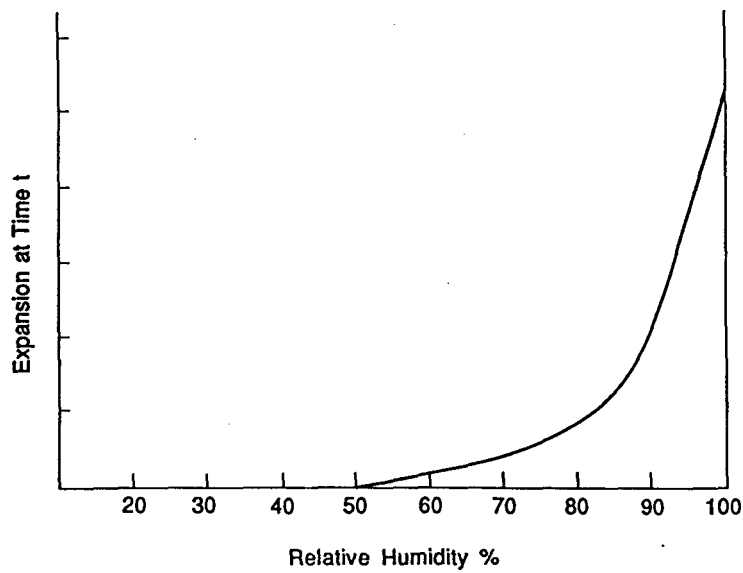
Figure 2.16 The effect of relative humidity on the expansion of concrete (Poole, 1992).
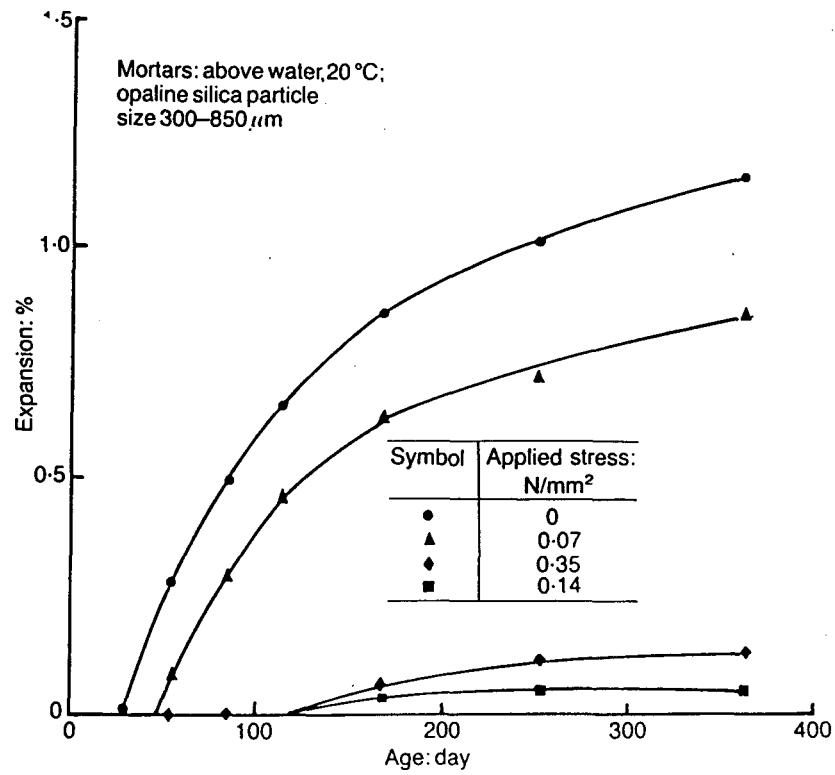
Figure 2.17 Expansion behavior of mortars subject continuously to different applied stresses (Hobbs 1988).
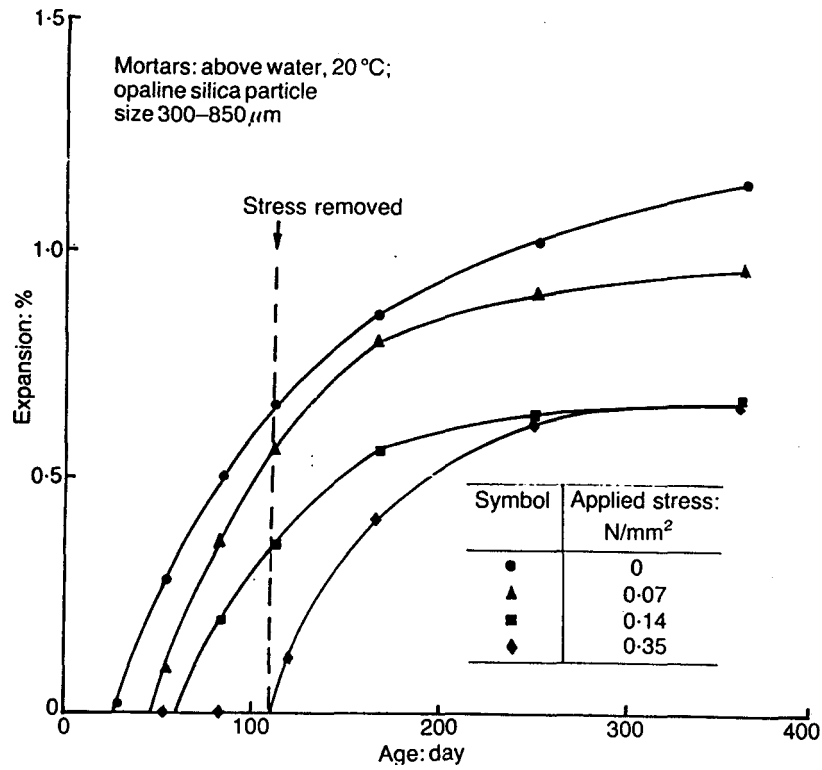
Figure 2.18 Expansion behavior of mortars subject to different applied stress, which has been removed at 111 days (Hobbs 1988).
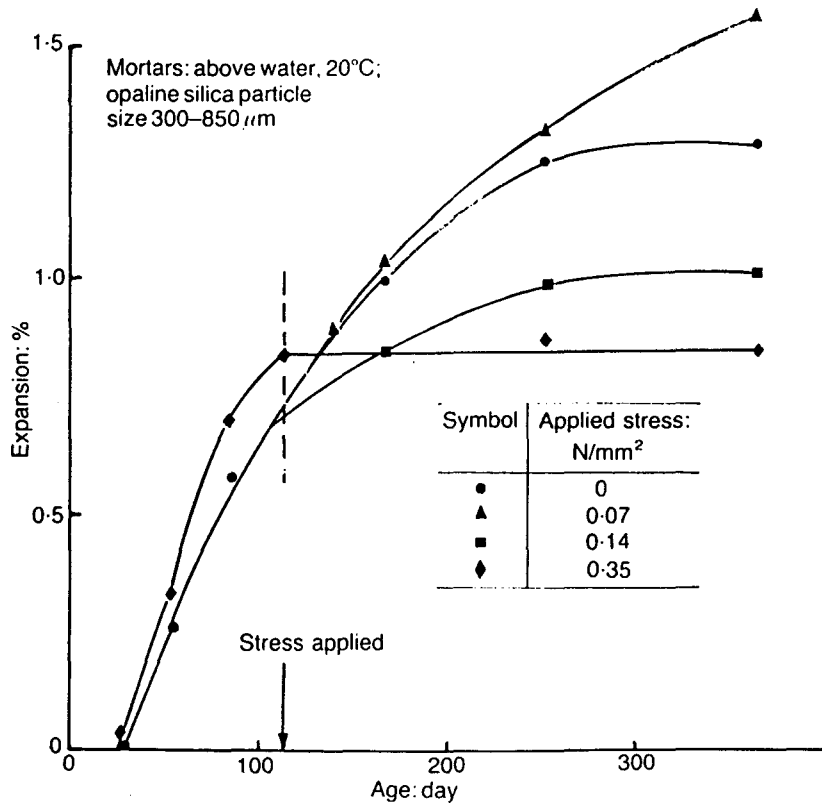
Figure 2.19 Expansion behavior of mortars subject to different stress, applied at 112 days (Hobbs 1988).
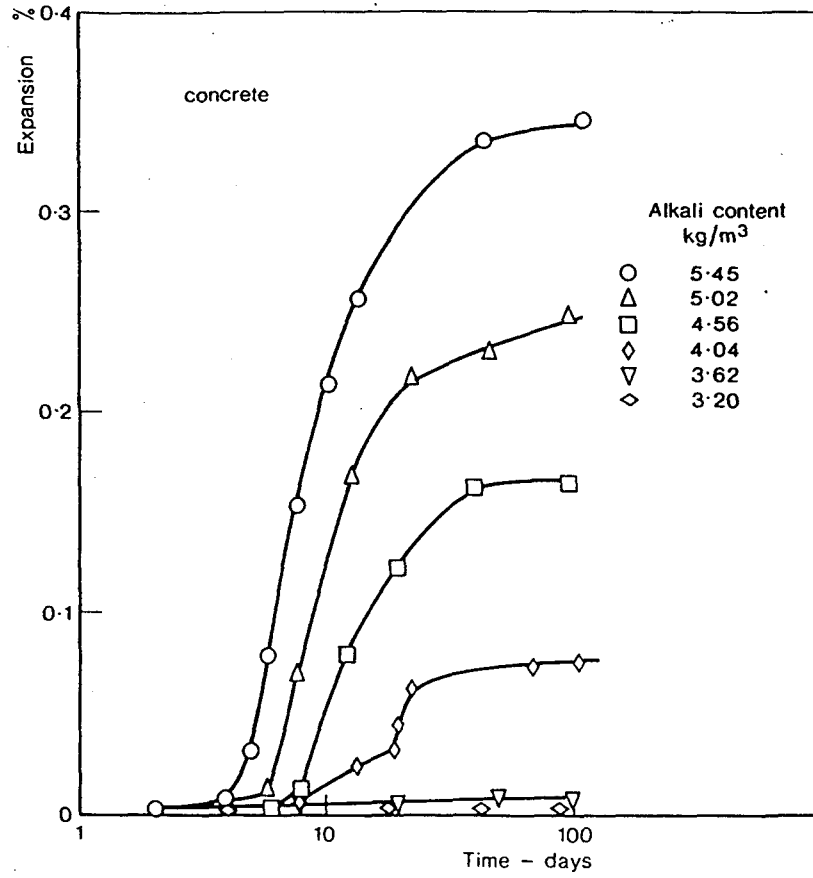
Figure 2.20 Influence of alkali content on expansion behavior (Hobbs, 1984).
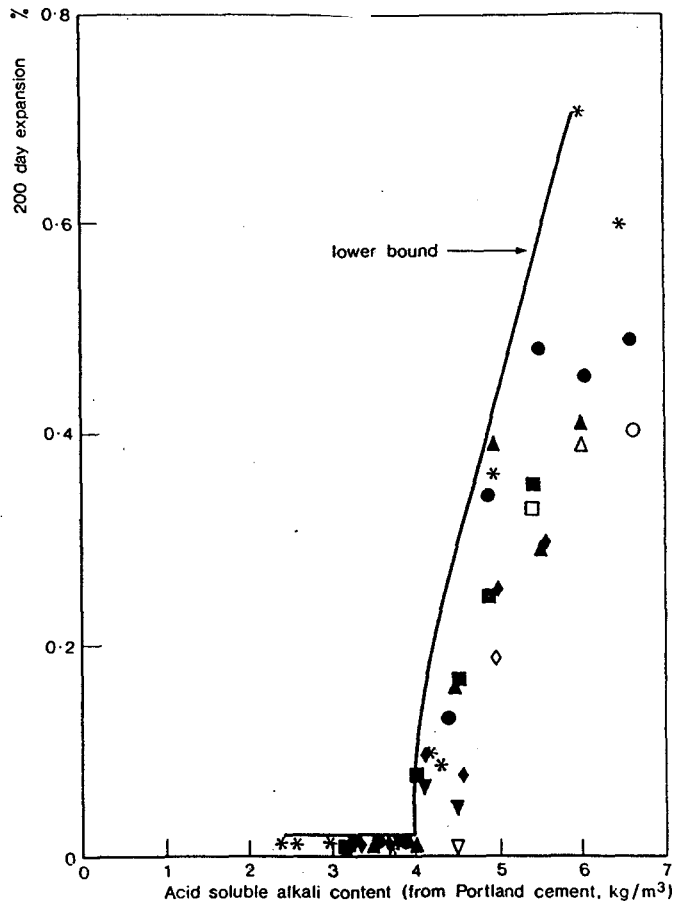
Figure 2.21 Variation of expansion at 200 days with acid soluble alkali content of concrete (Hobbs 1988).
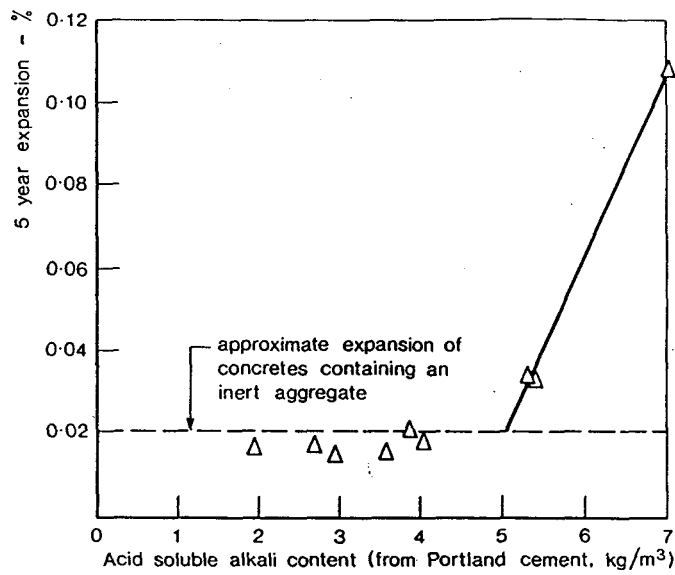
Figure 2.22 Variation of expansion at 5 years with acid soluble alkali content of concrete (Kennerlay *et al*, 1981).

Chapter 3
Constitutive Modeling of Concrete Subjected to AAR

3.1 Introduction

The modeling of AAR is very complex due to the numerous coupled processes affecting the reaction. The effectiveness of a constitutive model depends largely on the understanding of the AAR mechanisms and proper simplifications. Since the 1980's, some AAR models have been proposed to describe either the micro or the macro behavior of concrete affected by AAR. Generally, micro models focus on the physicochemical principles, and can consider only one specific factor which influences AAR. All influence factors can not be simultaneously taken into consideration. This major disadvantage makes these models less attractive in applications. On the other hand, macromodels are based on phenomenological approach. These models involve parameters which can be determined from either in-situ or laboratory experiments. It is obvious that a rigorous connection between micro and macro models may lead to a more satisfactory description of AAR.

In this chapter, an AAR constitutive model will be presented based on the framework proposed by Pietruszczak (1996). The formulation incorporates an assumption that the rate of expansion depends on the confining pressure, the age of concrete, and the temperature. The alkali content in concrete is assumed to remain constant throughout the reaction. The progress in reaction is coupled with the degradation of mechanical properties, particularly the elastic modulus, the compressive and tensile strengths.

Concrete can be considered as a macroscopically homogeneous nonlinear medium. The material nonlinearity occurs predominantly due to elastoplastic behavior triggered by a progressive microcracking. The concrete constitutive model adopted in this study (Pietruszczak *et al.*, 1988) is built within the framework of the rate-independent theory of plasticity. It incorporates a non-associated flow rule and the hardening effects are attributed to accumulated plastic distortions

3.2 Constitutive Modeling of AAR

3.2.1 Formulation of Constitutive Equations

In the elastic range, the strain is contributed by stress, AAR volumetric expansion, and thermo-expansion due to temperature change. Thus, the constitutive relation can be expressed as

$$\varepsilon^e = \left[C^e \right] \sigma + \frac{1}{3} \epsilon_A \, \delta + \frac{1}{3} \beta_T \left(T - T_o \right) \delta \qquad (3.1)$$

where $\left[C^e \right]$ is the elastic compliance; δ is the Kronecker's delta; ϵ_A represents the volumetric expansion due to formation of alkali-silica gel; β_T is the coefficient of thermal expansion, T represents temperature, and T_o is the reference temperature.

Multiplying Equation 3.1 by the elastic stiffness $\left[D^e \right]$, the following expression can be obtained

$$\sigma = \left[D^e \right] \left[\varepsilon^e - \frac{1}{3} \epsilon_A \, \delta - \frac{1}{3} \beta_T \left(T - T_o \right) \delta \right] \qquad (3.2)$$

Differentiating now Equation 3.2 with respect to time,

$$\dot{\sigma} = \left[\mathbf{D}^e\right]\left(\dot{\varepsilon}^e - \frac{1}{3}\dot{e}_A\,\delta - \frac{1}{3}\beta_T\dot{T}\delta\right) + \left[\dot{\mathbf{D}}^e\right]\left[\mathbf{C}^e\right]\sigma \qquad (3.3)$$

Equation. 3.3 indicates that the elastic properties are affected by the continuing expansion due to alkali-aggregate reaction. The volumetric expansion e_A is constrained by the hydrostatic pressure, which is assumed to have little effect on the progress of the reaction itself. The evolution law for e_A is assumed in the following incremental form

$$\dot{e}_A = g_1(\delta^T\sigma)\dot{g}_2(t)g_3(T) \qquad (3.4)$$

where the functions $g_1(\delta^T\sigma)$, $g_2(t)$ and $g_3(T)$ govern the influences of hydrostatic stress, concrete age and temperature, respectively.

It should be noted that Equation 3.1 ensures that the rate of dissipation of energy due to degradation of elastic properties remains positive. According to Equation 3.1, $\sigma^T\dot{\varepsilon} > 0$ requires $det\left|\dot{\mathbf{C}}^e\right| > 0$, which is generally satisfied for a degrading elastic material.

Consider the response in the elastoplastic range. Assuming the additivity of the elastic and plastic strain rates $\dot{\varepsilon} = \dot{\varepsilon}^e + \dot{\varepsilon}^p$, the constitutive relation in Equation 3.2 takes the form

$$\dot{\sigma} = \left[\mathbf{D}^e\right]\left(\dot{\varepsilon} - \dot{\varepsilon}^p - \frac{1}{3}\dot{e}_A\,\delta - \frac{1}{3}\beta_T\dot{T}\delta\right) + \left[\dot{\mathbf{D}}^e\right]\left[\mathbf{C}^e\right]\sigma \qquad (3.5)$$

In order to define the plastic strain rates, the yield surface is assumed to be affected by the progress in AAR. Thus,

$$f(\sigma,\varepsilon^p,t) = 0 \qquad (3.6)$$

$$\dot{\varepsilon}^{P} = \lambda \frac{\partial Q}{\partial \sigma} \tag{3.7}$$

where $Q = Q(\sigma) = $ const. is the plastic potential function. Writing the consistency condition,

$$\dot{f} = \left(\frac{\partial f}{\partial \sigma}\right)^{T} \dot{\sigma} + \left(\frac{\partial f}{\partial \varepsilon^{P}}\right)^{T} \lambda \frac{\partial Q}{\partial \sigma} + \frac{\partial f}{\partial t} = 0 \tag{3.8}$$

and utilizing Equation 3.5, one obtains

$$\lambda = \frac{1}{H} \left[\left(\frac{\partial f}{\partial \sigma}\right)^{T} \left[\mathbf{D}^{e}\right] \left(\dot{\varepsilon} - \frac{1}{3}\dot{\varepsilon}_{A}\,\delta - \frac{1}{3}\beta_{T}\dot{T}\delta\right) + \left(\frac{\partial f}{\partial \sigma}\right)^{T} \left[\dot{\mathbf{D}}^{e}\right]\left[\mathbf{C}^{e}\right]\sigma + \frac{\partial f}{\partial t} \right] \tag{3.9}$$

where

$$H = \left(\frac{\partial f}{\partial \sigma}\right)^{T} \left[\mathbf{D}^{e}\right] \frac{\partial Q}{\partial \sigma} - \left(\frac{\partial f}{\partial \varepsilon^{P}}\right)^{T} \frac{\partial Q}{\partial \sigma} \tag{3.10}$$

Substituting Equation 3.10 into Equation 3.5 and rearranging, the constitutive relation in incremental form is obtained

$$\dot{\sigma} = \left[\mathbf{D}^{ep}\right]\left(\dot{\varepsilon} - \frac{1}{3}\dot{\varepsilon}_{A}\,\delta - \frac{1}{3}\beta_{T}\dot{T}\delta\right) - \left(\frac{1}{H}\left[\mathbf{D}^{e}\right]\frac{\partial Q}{\partial \sigma}\left(\frac{\partial f}{\partial \sigma}\right)^{T} - \left[\mathbf{I}\right]\right)\left[\dot{\mathbf{D}}^{e}\right]\left[\mathbf{C}^{e}\right]\sigma - \frac{1}{H}\frac{\partial f}{\partial t}\left[\mathbf{D}^{e}\right]\frac{\partial Q}{\partial \sigma}$$

$$\tag{3.11}$$

where the elastoplastic constitutive matrix is defined as

$$\left[\mathbf{D}^{ep}\right] = \left[\mathbf{D}^{e}\right] - \frac{1}{H}\left[\mathbf{D}^{e}\right]\frac{\partial Q}{\partial \sigma}\left(\frac{\partial f}{\partial \sigma}\right)^{T}\left[\mathbf{D}^{e}\right] \tag{3.12}$$

The inverse relation, suitable for an arbitrary stress-controlled program, can be derived by invoking the additivity postulate and differentiating Equation 3.1 with respect to time,

$$\dot{\varepsilon} = \dot{\varepsilon}^e + \dot{\varepsilon}^p = \left[C^e\right]\dot{\sigma} + \left[\dot{C}^e\right]\sigma + \frac{1}{3}\dot{e}_A\,\delta + \frac{1}{3}\beta_T\dot{T}\delta + \dot{\varepsilon}^p \qquad (3.13)$$

Utilizing the consistency condition in Equation 3.8,

$$\dot{\lambda} = \frac{1}{H_p}\left[\left(\frac{\partial f}{\partial \sigma}\right)^T \dot{\sigma} + \frac{\partial f}{\partial t}\right] \qquad (3.14)$$

where

$$H_p = -\left(\frac{\partial f}{\partial \varepsilon^p}\right)^T \frac{\partial Q}{\partial \sigma} \qquad (3.15)$$

Finally, by substituting Equation 3.14 into Equation 3.13, the following relation is obtained

$$\dot{\varepsilon} = \left[C^{ep}\right]\dot{\sigma} + \left[\dot{C}^e\right]\sigma + \frac{1}{H_p}\frac{\partial f}{\partial t}\frac{\partial Q}{\partial \sigma} + \frac{1}{3}\dot{e}_A\,\delta + \frac{1}{3}\beta_T\dot{T}\delta \qquad (3.16)$$

where $\left[C^{ep}\right]$ is the elastoplastic compliance

$$\left[C^{ep}\right] = \left[C^e\right] + \frac{1}{H_p}\frac{\partial Q}{\partial \sigma}\left(\frac{\partial f}{\partial \sigma}\right)^T \qquad (3.17)$$

3.2.2 Evolution of Material Properties due to AAR

AAR expansion rate

The volume expansion due to AAR is assumed to be governed by a functional form of Equation 3.4, in which

$$g_1(\delta^T \sigma) = exp\left(A_1 \frac{\delta^T \sigma}{f_{co}}\right) \tag{3.18}$$

$$g_2(t) = \frac{\epsilon t}{A_2 + t} \tag{3.19}$$

$$g_3(T) = 2 \sec h\left(\frac{T - T_p}{A_5}\right) \tag{3.20}$$

where A_1, A_2, and A_5 are material constants; f_{co} designates the initial compressive strength; T_p is the pessimum temperature; t is time. Moreover, $0 \le g_1 < 1$, $g_2 \to \varepsilon$ when $t \to \infty$, and $g_3 \to 1$ when $T \to T_p$.

Degradation of material properties

In the elastic range, the only degrading parameter is the elastic modulus E. The evolution law is postulated in the following form

$$E|_{T=T_p} = E_o\left[1 - (1 - A_3)\frac{g_2}{\epsilon}\right] \tag{3.21}$$

$$\dot{E} = g_3(T)\dot{E}|_{T=T_p} \tag{3.22}$$

where A_3 is a material constant and E_o represents the initial modulus.

In addition, the progress in AAR results in degradation of the uniaxial compressive strength f_c . At $T = T_p$, the degradation function is chosen as

$$f_c\big|_{T=T_p} = f_{co}\left[1-(1-A_4)\frac{g_2}{\varepsilon}\right]$$ (3.23)

$$\dot{f}_c = g_3(T)\dot{f}_c\big|_{T=T_p}$$ (3.24)

where A_4 is a material constant and f_{co} designates the initial compressive strength. It should be noted that degradation of f_c is accompanied by a proportional reduction in the uniaxial tensile strength, as explained in the next section.

3.2.3 Constitutive Model of Concrete

In this study, the elastoplastic properties of concrete are described by the constitutive relation proposed by Pietruszczak et al (1988). The formulation invokes the concept of a failure surface $F(\sigma) = 0$, which is introduced a priori as a path-independent criterion. The progressive damage of the material due to microcracking is represented in terms of the evolution of the family of yield surfaces $f(\sigma,\xi) = 0$, where ξ is a damage parameter. The direction of plastic flow is defined by a non-associated flow rule, which involves the existence of a family of plastic potential surfaces $Q(\sigma) = const$. The material properties are affected by the value of confining pressure. An appropriate strain hardening/softening function is employed to ensure a smooth transition from ductile (stable) to brittle (unstable) response.

Failure surface

The failure surface, which defines the maximum strength of the material under any possible combination of stresses, is defined in the following form:

$$F = \overline{\sigma} - k(\theta)\overline{\sigma}_c = 0 \tag{3.25}$$

In Equation. 3.25,

$$\overline{\sigma}_c = \frac{-a_1 + \sqrt{a_1^2 + 4a_2\left(a_3 + \dfrac{I}{f_c}\right)}}{2a_2} f_c \tag{3.26}$$

where $I = -\sigma_{ii}$, $\overline{\sigma} = \left(\dfrac{1}{2}S_{ij}S_{ij}\right)^{\frac{1}{2}}$, $\theta = \dfrac{1}{3}\sin^{-1}\left(\dfrac{3\sqrt{3}J_3}{2\overline{\sigma}^3}\right)$, and $J_3 = \dfrac{1}{3}S_{ij}S_{jk}S_{ki}$ are the stress invariants. Moreover, the parameters a_1, a_2, and a_3 represent dimensionless material constants, and f_c is the uniaxial compressive strength of concrete.

In the principal stress space, this equation represents an irregular cone with smooth curved meridians (Figure 3.1). The function $k(\theta)$, which defines the shape of the failure surface in the deviatoric plane, is chosen in the following form

$$k(\theta) = \frac{\left(\sqrt{1+a} - \sqrt{1-a}\right)K}{K\sqrt{1+a} - \sqrt{1-a} + (1-K)\sqrt{1-a}\sin 3\theta}, \qquad a \to 1 \tag{3.27}$$

which satisfies $g(\dfrac{\pi}{6}) = 1$ and $g(-\dfrac{\pi}{6}) = K$, and for $a = 0.999$ guarantees convexity for $K \geq 0.5587$. The parameter K is defined as $K = \dfrac{\overline{\sigma}_t}{\overline{\sigma}_c}$, where $\overline{\sigma}_t$ and $\overline{\sigma}_c$ represent the maximum deviatoric stress intensities $\overline{\sigma}$ for I = const. in the extension $(\theta = -\dfrac{\pi}{6})$ and the

compression ($\theta = \dfrac{\pi}{6}$) domains, respectively. In the present study, K is assumed to be a function of I, i.e.

$$K = 1 - K_o e^{-K_1\left(a_3 + \frac{I}{f_c}\right)}$$

(3.28)

where K_o and K_1 are material constants. The above representation ensures that the π-plane section of the failure surface evolves from a curvilinear triangle for low confining pressures to a nearly circular shape at high confining pressures, which is consistent with existing experimental evidence.

Yield surface

The yield surface is chosen in a functional form similar to that of the failure surface

$$f = \bar{\sigma} - \beta(\xi)k(\theta)\bar{\sigma}_c = 0$$

(3.29)

where $\beta(\xi)$ represents the hardening/softening function. In the ductile regime (at relative high confining pressure), in which material characteristics are stable, β is defined in a simple hyperbolic form:

$$\beta(\xi) = \frac{\xi}{A + B\xi}$$

(3.30)

Whereas in the brittle regime, (at relative low confining pressure), in which material characteristics are not stable,

$$\beta(\xi) = \frac{\xi}{A + B\xi}\left\{1 - \bar{\phi}_r\left[1 - \exp\left(-C\langle \xi - \xi_f \rangle^\gamma\right)\right]\right\}$$

(3.31)

Here A and B are material constants; ξ_f represents the value of ξ corresponding to the maximum value of $\beta = \beta_f$; γ is a material constant; $\bar{\phi}_r$ defines the residual strength of the material and C controls the rate of strain softening in post-bifurcation mode. The damage parameter ξ is assumed to be a function of accumulated plastic distortions

$$\xi = \int d\xi \tag{3.32}$$

$$d\xi = \frac{\sqrt{2J_2(\dot{\varepsilon}^p)}}{\bar{\Phi}} \tag{3.33}$$

where $J_2(\dot{\varepsilon}^p)$ is a second deviatoric plastic strain rate invariant; and $\bar{\Phi} = const$ is defined by a parametric equation in the form:

$$\Phi(I,\theta) = \left[k(\theta)\left(a_3 + \frac{I}{f_c}\right)\right]^2 = \bar{\phi} \tag{3.34}$$

In view of the degradation of properties, Equations. 3.28 and 3.29 yield

$$\frac{\partial f}{\partial t} = \frac{\partial f}{\partial \bar{\sigma}_c} \frac{\partial \bar{\sigma}_c}{\partial f_c} \frac{\partial f_c}{\partial g_2} \frac{dg_2}{dt} = -\beta(\xi)k(\theta)\left(\frac{\bar{\sigma}_c}{f_c} - \frac{I}{2a_2\bar{\sigma}_c + a_1 f_c}\right)\dot{f}_c \tag{3.35}$$

Plastic potential surface

The direction of plastic flow is governed by a non-associated flow rule $d\varepsilon_{ij}^p = d\lambda \dfrac{\partial Q}{\partial \sigma_{ij}}$, in which $d\lambda$ is a positive scalar. The plastic potential (Figure 3.2) is selected in the form

$$Q = \bar{\sigma} + \eta_c k(\theta)\bar{I}\ln\left(\frac{\bar{I}}{\bar{I}_o}\right) = 0 \tag{3.36}$$

where $\bar{I} = a_o f_c + I$, a_o defines the location of the apex of the current potential surface in the tensile domain and η_c represents the value of $\eta = \dfrac{\bar{\sigma}}{k(\theta)\bar{I}}$ at which a transition from compaction to dilatation takes place.

3.2.4 Numerical Integration Algorithms

Stress-controlled programs

A stress-controlled program is generally used to identify material parameters, and carry out the numeral simulation for comparison with the test data. The numerical procedure is described in the following steps.

At the beginning of step $n+1$, the following parameters are known: σ_n, $\Delta\sigma$, ε_n, T_n and ΔT.

1) Update the stress

$$\sigma_{n+1} = \sigma_n + \Delta\sigma \tag{3.38}$$

2) Determine the parameter β_{n+1} from $f_{n+1} = 0$.

3) Determine $\Delta\xi$

$$\xi_{n+1} = \frac{A\beta_{n+1}}{1 - B\beta_{n+1}} \tag{3.39}$$

then

$$\Delta\xi = \xi_{n+1} - \xi_n \tag{3.40}$$

4) Compute $\Delta\lambda$

$$\Delta\lambda = \Delta\xi \frac{\overline{\Phi}}{\sqrt{2J_2\left(\dot{\varepsilon}^p\right)}}$$

(3.41)

5) Compute the plastic strain increment

$$\Delta\varepsilon^p = \Delta\lambda\left(\frac{\partial Q}{\partial\sigma}\right)$$

(3.42)

6) Compute the elastic strain increment

$$\Delta\varepsilon^e = \left[C^e\right]\Delta\sigma + \left[\dot{C}^e\right]\sigma + \frac{1}{3}\Delta\epsilon_A\,\delta + \frac{1}{3}\beta_T\Delta T\delta$$

(3.43)

where $\Delta\varepsilon_A = g_1(\delta^T\sigma)\dot{g}_2(t)g_3(T)\Delta t$

7) Compute the total strain increment

$$\Delta\varepsilon = \Delta\varepsilon^e + \Delta\varepsilon^p$$

(3.44)

8) Obtain the total stain

$$\varepsilon_{n+1} = \varepsilon_n + \Delta\varepsilon$$

(3.45)

Go to step 1, and repeat the procedure.

Numerical examples based on the stress-controlled scheme are presented in Section 3.2.5.

Strain-controlled programs

In the finite element analysis, a strain-controlled procedure is required as a model drive to simulate the behaviour of the material. In the following, a simple explicit scheme is derived by using the stress state and state variables at the beginning of each incremental step. In each step, a subincrementation strategy is employed to improve the accuracy and stability

of the explicit algorithm. The accuracy increases with the number of subincrements. However, it is difficult to predict this number *a priori*, so that the degree of accuracy can not easily to be established. Further, the subincrementation strategy can not guarantee the stability of the integration algorithm. The numerical procedure incorporates the steps as outlined below.

At the beginning of step $n+1$, the following parameters are known: ε_n, $\Delta\varepsilon$, σ_n, T_n, and ΔT.

1) Predict the increment of elastic strain

$$\Delta\varepsilon^e = \Delta\varepsilon - \frac{1}{3}(\Delta\epsilon_A)_n \delta - \frac{1}{3}\beta_T \Delta T \delta - \left[\dot{\mathbf{C}}_n^e\right]\sigma_n \qquad (3.46)$$

Divide the increment of elastic strain $\Delta\varepsilon^e$ into m subincrements, and carry out the following steps.

2) Calculate trial stress

$$\Delta\sigma^{tr} = \left[\mathbf{D}^e\right]\Delta\varepsilon \qquad (3.47)$$

$$\sigma^{tr}_{n+1} = \sigma_n + \Delta\sigma^{tr} \qquad (3.48)$$

3) Compute $\Delta\lambda$

$$\Delta\lambda = \frac{1}{H_p}\left[\left(\frac{\partial f}{\partial\sigma}\right)_n^T \Delta\sigma^{tr} + \left(\frac{\partial f}{\partial t}\right)_n \Delta t\right] \qquad (3.49)$$

4)Compute the plastic stress increment

$$\Delta\varepsilon^p = \Delta\lambda\left(\frac{\partial Q}{\partial\sigma}\right)_n \qquad (3.50)$$

5) Compute the total stress

$$\sigma_{n+1} = \sigma^e_{n+1} - [D]\Delta\varepsilon^p \qquad (3.51)$$

6) Correct the stress, in order to satisfy the condition $f(\sigma_{n+1}) = 0$ back to the yield surface.

Repeat the steps 2 to 6 for subsequent subincrements.

The tangential operator $[D]_{n+1}$ is non-symmetric due to non-associated flow rule. A simplified one (Huang *et al.*, 1996) can be adopted in the form

$$[C]_{n+1} = [C^e]_{n+1} + [\dot{C}^e]_{n+1}\Delta t + \frac{1}{3}\left[\frac{\partial g_1}{\partial(\delta^T\sigma)}\right]_{n+1} \dot{g}_2 g_3 \Delta t(\delta\delta^T) \qquad (3.52)$$

$$[D]_{n+1} = [C]^{-1}_{n+1} \qquad (3.53)$$

3.3 Numerical Examples of Stress-Controlled Point Integration

Following are two numerical examples of a point integration using the stress-controlled algorithm. The examples pertain to AAR-induced deformation in concrete samples subjected to a constant axial load of different intensities.

3.3.1 Simulation of the Response of Concrete under Isothermal Condition

The first example is related to simulation of the response under isothermal conditions. The material parameters are chosen as $E_o = 25{,}000$ MPa, $f_{co} = 30$ MPa, $\varepsilon = 0.001$, $v = 0.166$, $A_1 = 0.1$, $A_2 = 200$, $A_3 = 0.3$, $A_4 = 0.8$, $g_3 = 1$. The results of numerical simulations are presented in Figures 3.3 to 3.5.

Figures 3.3 and 3.4 show the time history of axial (ε_l) and volumetric strain (ε_v) for samples under vertical compressive stress of 0, 10, 20 and 25 MPa. The sample in the stress-free state undergoes a progressive expansion consistent with the assumed g_1-characteristic. At the vertical stress of 10 MPa, the degradation of material properties results in axial contraction which counteracts the AAR-induced expansion, so that there is virtually no deformation in the vertical direction. At higher stress intensities (e.g. 20 MPa), the effect of degradation becomes even more prominent resulting in a substantial increase in axial contraction. For the sample under the vertical stress of 25 MPa, the degradation phenomenon leads to the brittle failure.

This aspect is further illustrated in Figure 3.5, which shows the material response in terms of the hardening/softening function β. The definition of this function has been given in Section 3.2.3. In general, $0 \le \beta \le 1$, with $\beta \to 1$ specifying the condition at failure. Thus, the evolution of β is an indicator of the extent of degradation in the plastic properties of the material. The results shown in Figure 3.5 clearly indicate that for sample subjected to axial load of 25 MPa, $\beta \to 1$ as a result of continuing reaction, which signifies the brittle failure.

3.3.2 Simulation of the Response of Concrete Subjected to the Seasonal Temperature Variations

The second example deals with the simulation of the response under a seasonal temperature variation. The material parameters are chosen as $E_o = 15,000$ MPa, $v = 0.2$, $f_{co} = 30$ MPa, $\varepsilon = 0.034$, $A_1 = 0.1$, $A_2 = 1825$, $A_3 = 0.385$, $A_4 = 0.385$. $A_5 = 15.2$. As a

reference, the response of the same sample in isothermal condition of 5.2 °C is also calculated. The seasonal temperature change is approximated by

$$T(t) = A\sin\frac{2\pi(t+\zeta)}{P} + T_m \tag{3.54}$$

where $A = \dfrac{T_{max} + T_{min}}{2}$ is the mean value of maximum and minimum monthly temperatures

in °C; t is the time (in day); ζ is the lag factor; P is the period of the sine function, (365

days) and $T_m = \dfrac{T_{max} - T_{min}}{2}$. In this example, $T_{max} = 21°C$, $T_{min} = -9°C$, $\zeta = 0$.

The time histories of axial strain ε_l and volumetric strain ε_v are presented in Figures 3.6 and 3.7, respectively. AAR has the potential to cause a larger expansion than that due to annual temperature cycles. Under isothermal condition, the concrete expansion undergoes a progressive increase. The seasonal temperature variation causes a higher expansion in summer and a lower one in winter, for each annual period. In the stress-free state, the accumulated axial expansion undergoes a progressive increase. The average volumetric characteristics, in the stress-free state as well as at vertical stress of 10 MPa and 20 MPa, are similar to those corresponding to isothermal conditions. For the sample under the vertical stress of 25 MPa, AAR expansion leads the concrete sample to the brittle failure of the sample (Figure 3.8).
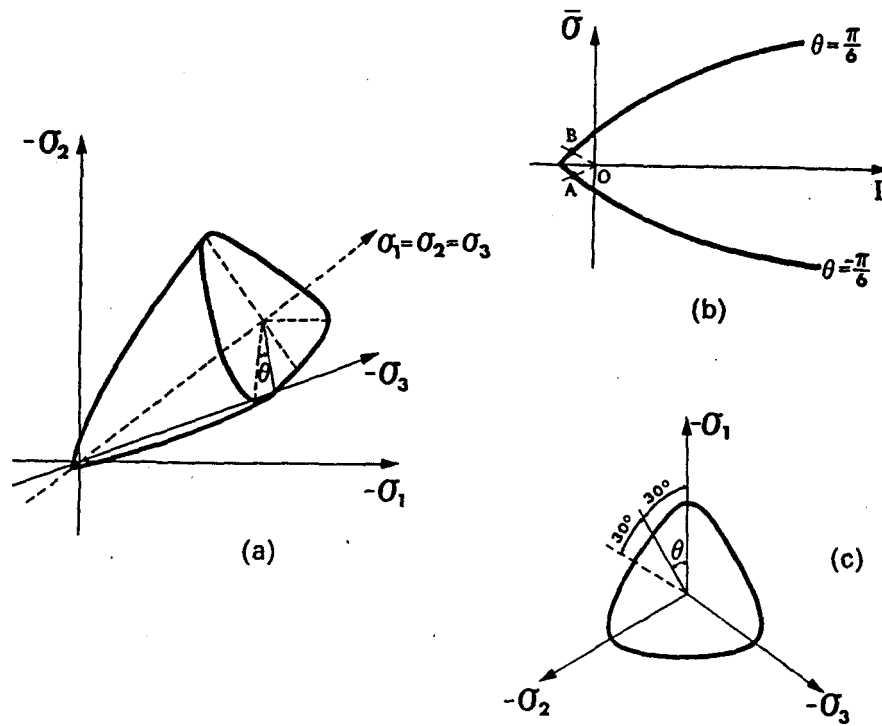
Figure 3.1 Failure surface. (a) Principal stress space; (b) Meridional plane;
(c) Deviatoric plane (π plane). (Pietruszczak *et al*, 1988)
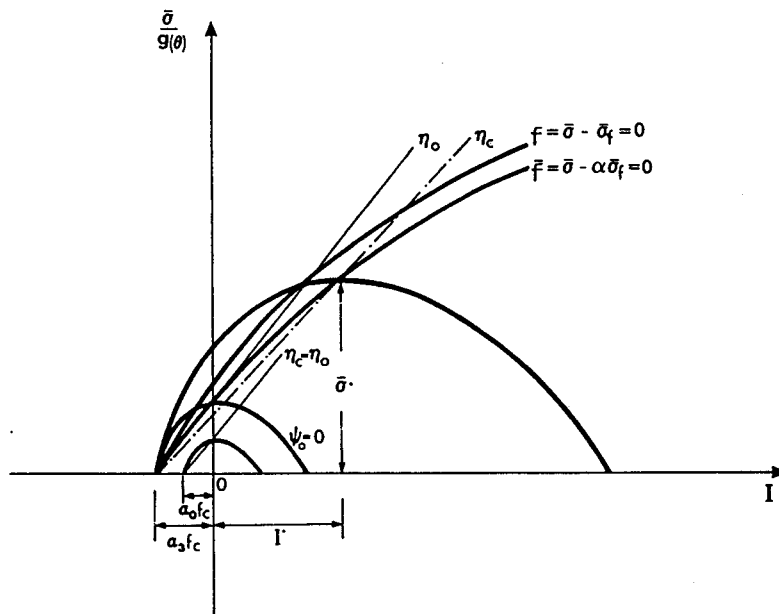
Figure 3.2   Plastic potential surface in meridional section (Pietruszczak *et al*. 1988).
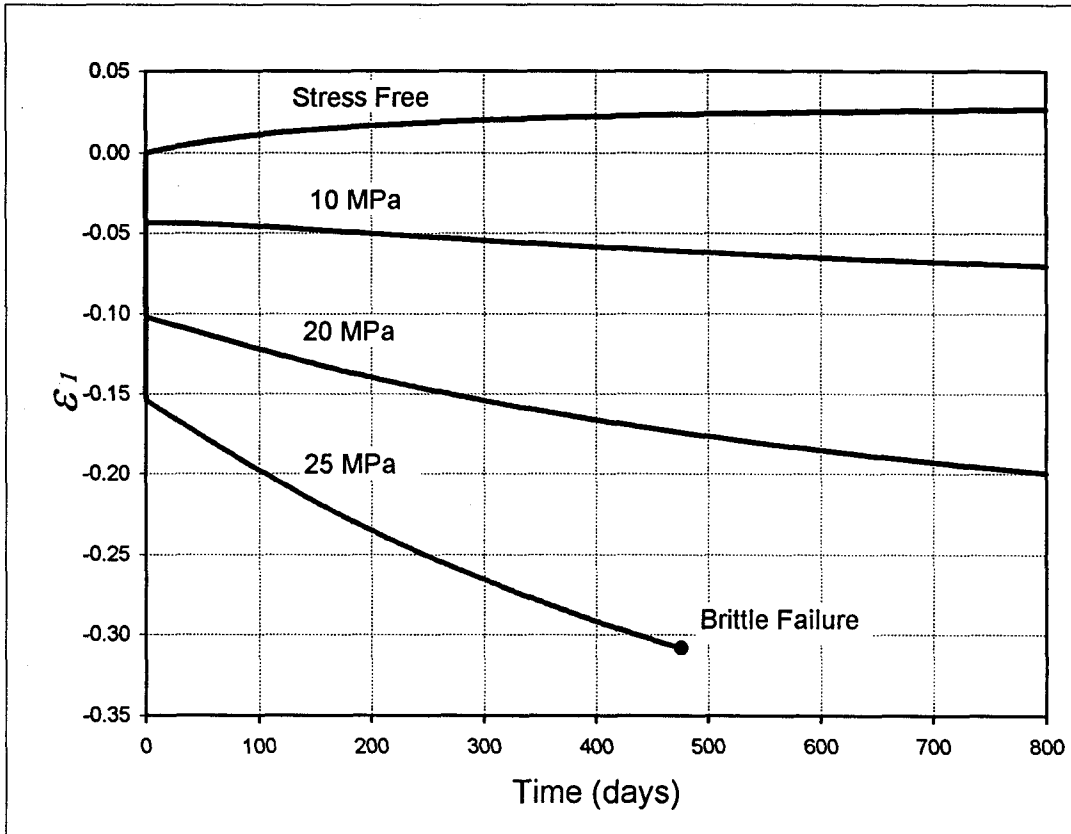
Figure 3.3 Simulation of axial expansion in isothermal condition
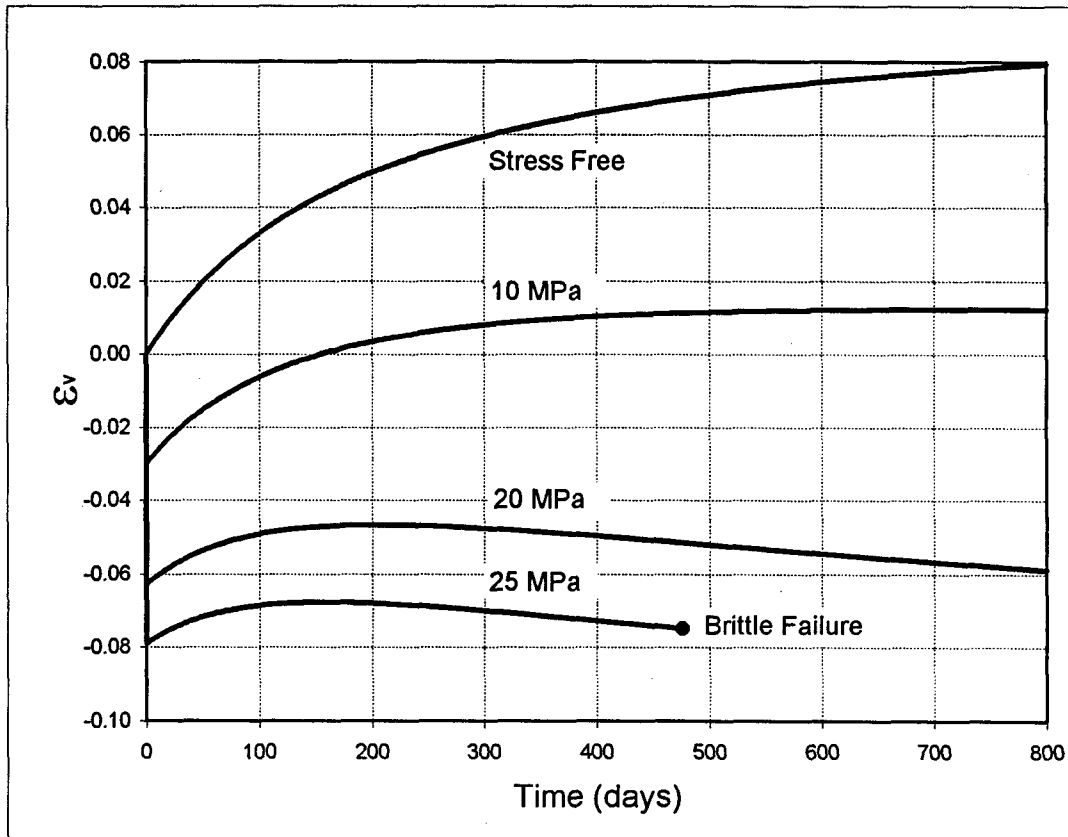
Figure 3.4 Simulation of volumetric expansion in isothermal condition.
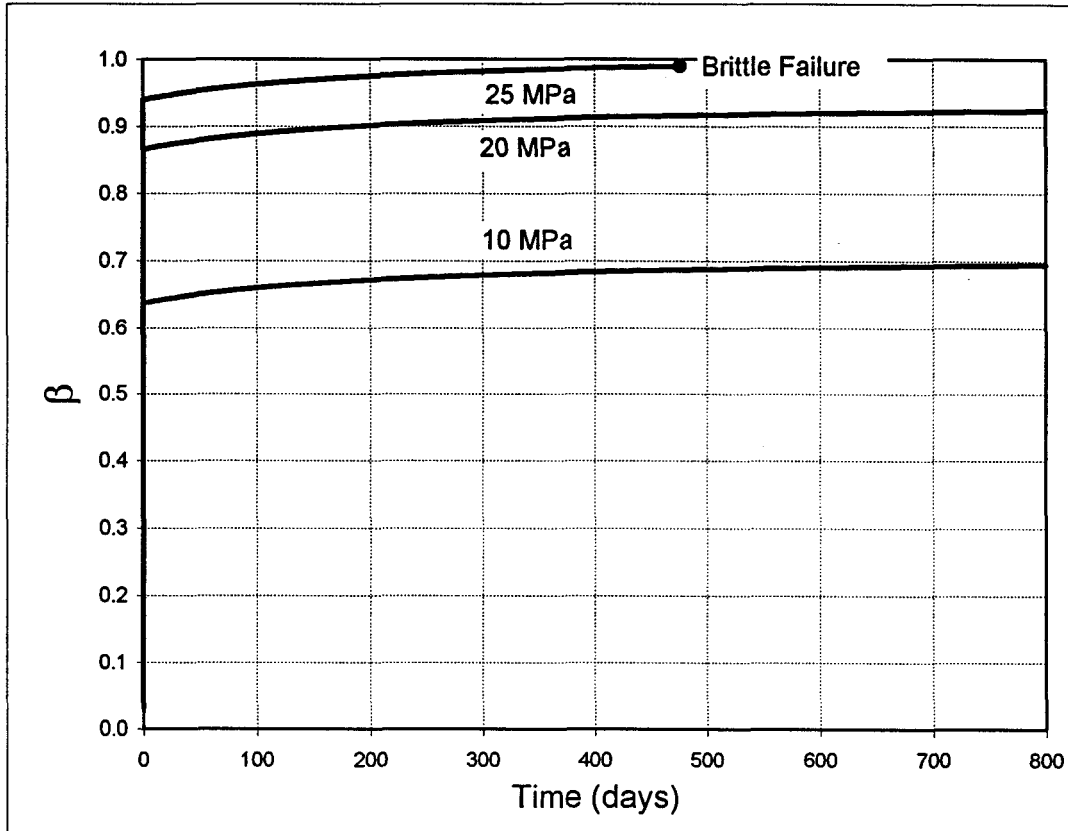
Figure 3.5 Evolution of hardening/softening parameter
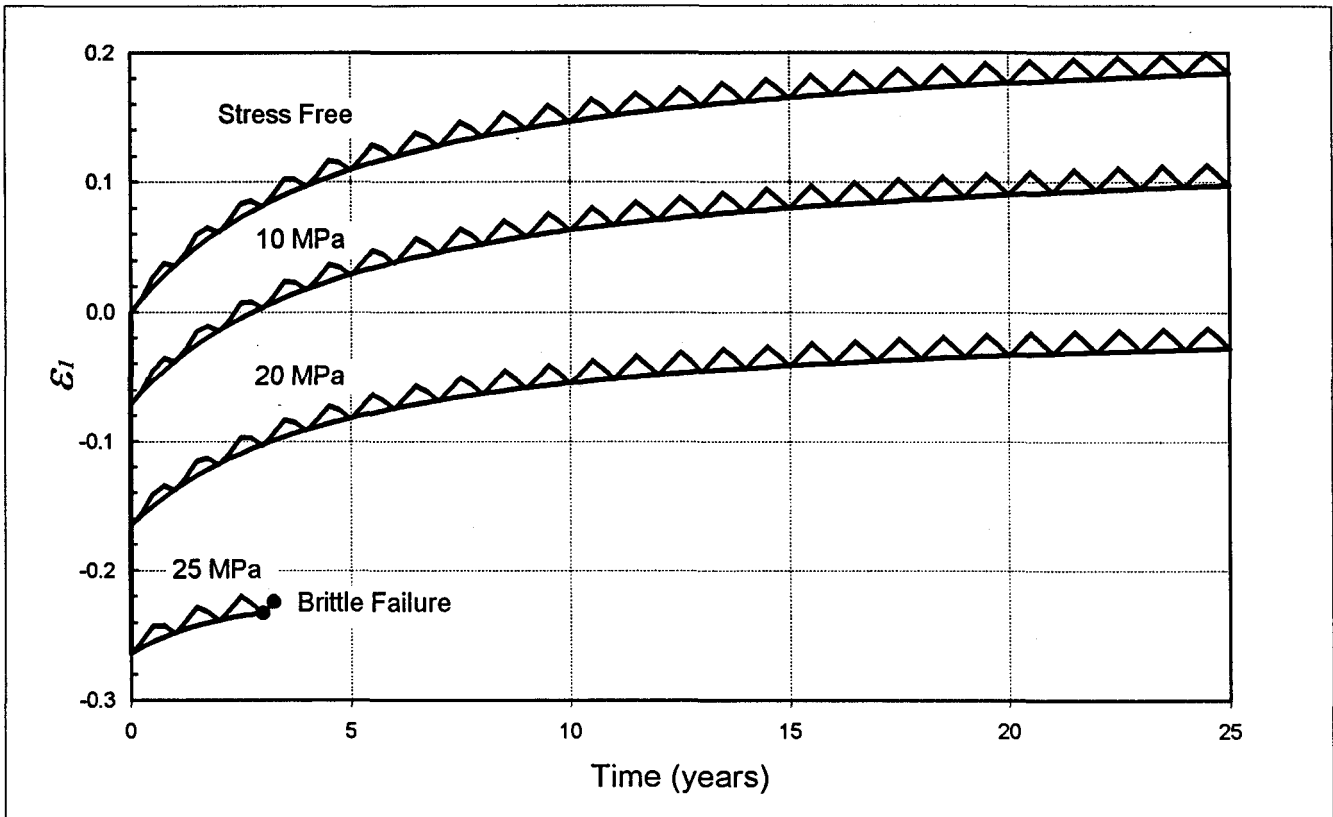
Figure 3.6 The axial expansion of concrete under seasonal temperature variation.
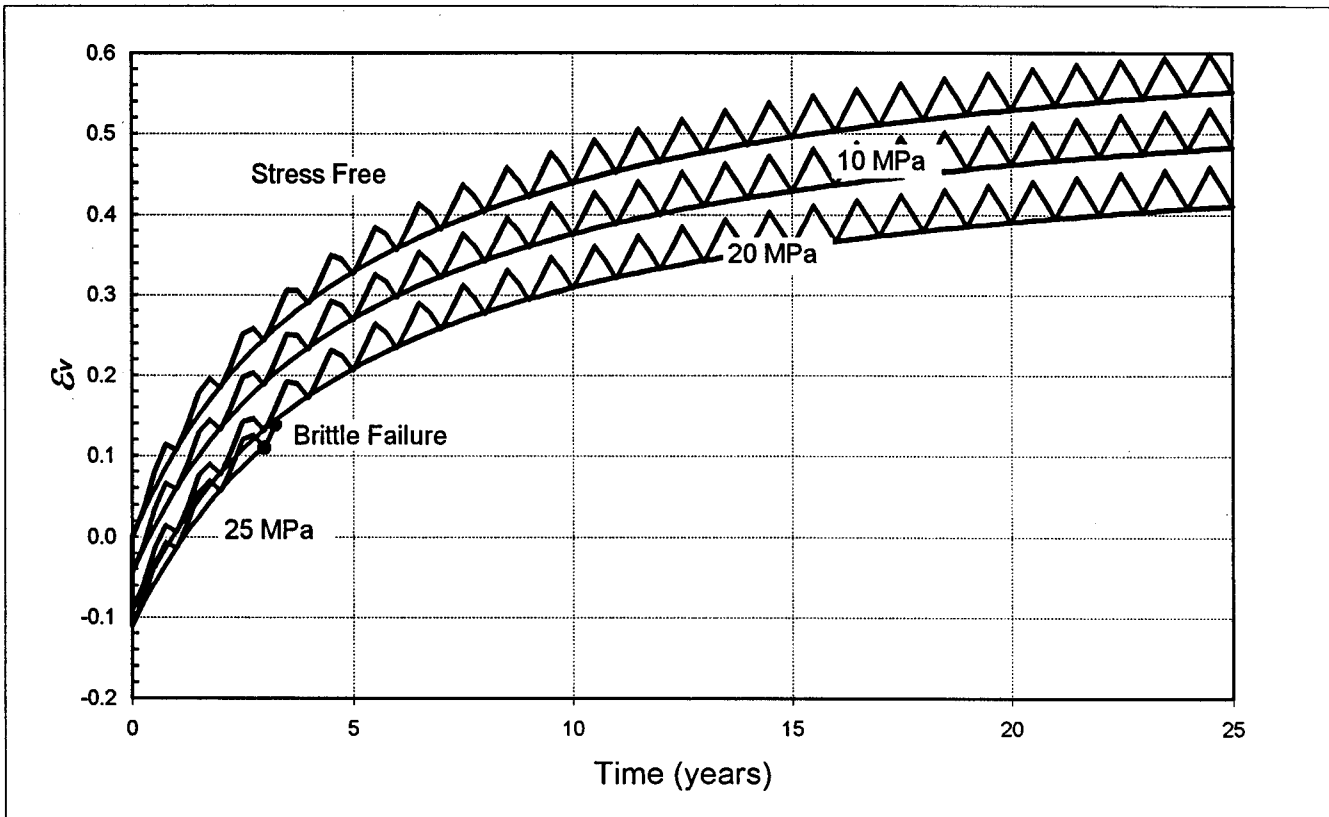
Figure 3.7 The volumetric expansion of concrete under seasonal temperature variation.
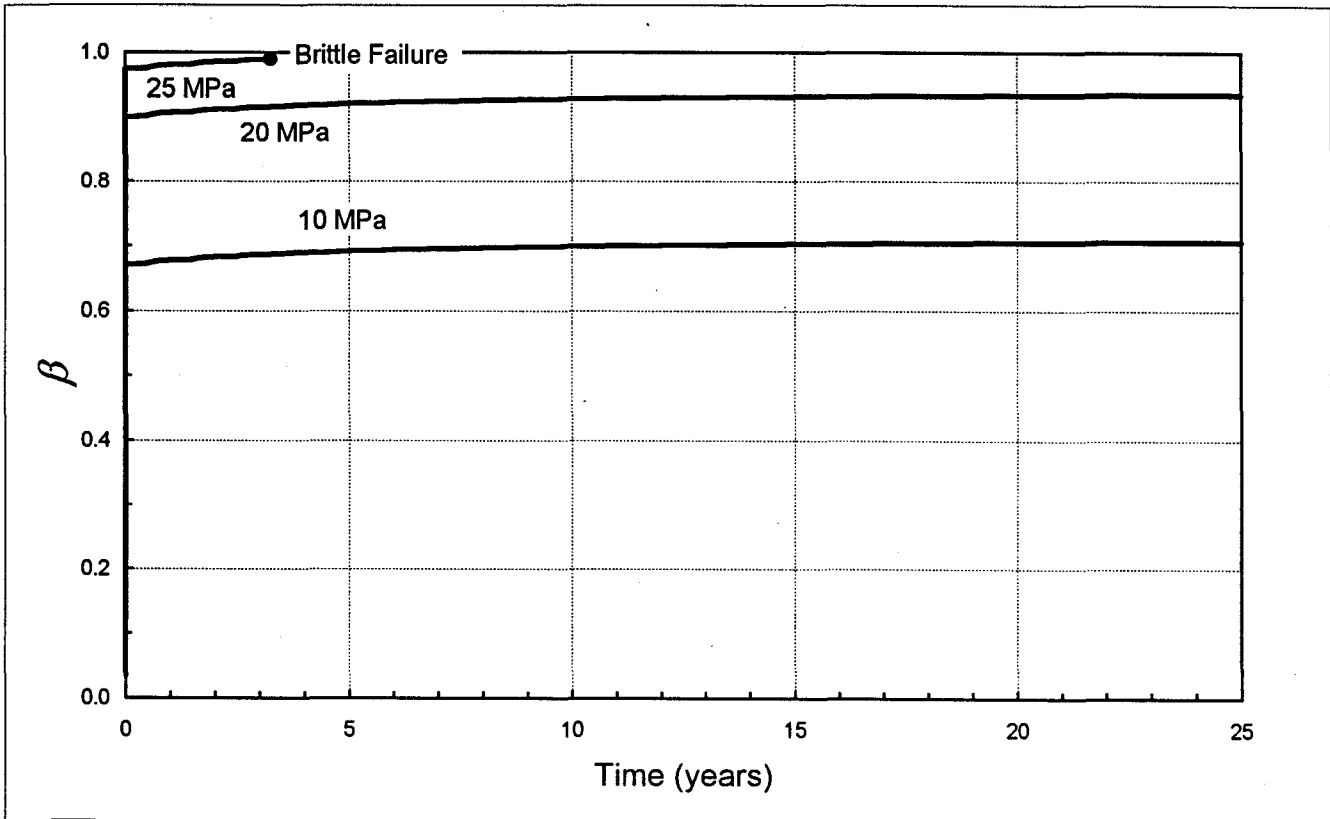
Figure 3.8 The time history of hardening/softening parameter β.

Chapter 4

Generating FE Model and Interface Programs

4.1 Introduction

In its early stages of development, the FEM was used to solve relatively small problems due to the limitations of computer hardware. The input data was manually prepared, and the numerical results were presented in the form of tables designed to be analyzed by the user. For large problems, preparing input data and reading results are laborious work requiring great patience. With the appearance of high performance graphics equipment, FEM preprocessors and postprocessors have developed rapidly. Large problems can now be modeled with computer-aid and the results can be displayed graphically. Today, FEM has merged with CAD to become a more sophisticated system, known as computer-aided engineering (CAE).

In the last three decades, a great number of innovations and improvements of FEM have been made in analyses techniques and in the complexity of solution algorithms. Recently, quite sophisticated graphical user interfaces (GUI) for PC's and workstation's have been developed for modeling large problems. The demand for GUI has made software design much more complex, and prompted a new programming philosophy, which considers the preprocessor, solver, and postprocessor as a whole system instead of three separated modules, and uses the object-oriented programming scheme to make the software design, programming, testing and maintenance more efficient.

Due to historical reasons, most FEM solvers are written in FORTRAN77, which is a blind language with limited data types and operations. To make use of the existing programs, a common strategy is to code interface programs linking the preprocessor, solver, and postprocessor.

In this Chapter, the issues related to the generation of a finite element model are introduced. Subsequently, the commercial code COSMOS/M, which is used in the generation of finite element models in this study, is briefly described. Then, interface schemes linking COSMOS/M and finite element solvers PLASTEX and DARC are developed. It should be noted that this Chapter does not intend to cover all the aspects of pre- and postprocessing, but to present general knowledge in order to evaluate the existing software and setup schemes of generating finite element models analyzed in this thesis.

4.2 Geometric Modeling

The first step in generating a finite element model is to define the problem geometry. In geometric modeling, a model is built by specifying relations between geometric entities, which are maintained by the modeling system. In COSMOS/M, there are eight geometric entities, which can be classified into two catagories: i) points, curves, surfaces and volumes are parametric entities, which can be used for parametric mesh generation; ii) contours, regions, polyhedra and parts are non-parametric entities, which can be used for automatic meshing. These geometric entities compose the geometric model. The commonly used geometric representations are wireframe, surface, and solid modeling

(Hoffmann, 1989). Virtually any manifold geometric object can be modeled for finite element analysis.

4.2.1 Wireframe Modeling

Wireframe models represent an object by defining its edges. A wireframe model consists entirely of points and various kinds of curves, including lines, arcs, circles, etc. When a wireframe view of an object is displayed, only the edges or edge contours of the object can be shown. The user needs to imagine a wire that is bent to follow the edges of the object to generate the model.

In a wireframe model, edges imply surfaces, surfaces in turn can imply solids. Thus, a wireframe model provides a useful description of an object. Certain information can be extracted from a wireframe model directly for generating a finite element mesh.

On the other hand, wireframe models have disadvantages and limitations. Since an edge has no thickness, it can not hide anything behind itself. Therefore, hidden-edge or shading views of the model can not be applied. Thus, a wireframe model may reveal too much visible information at one time. Figure 4.1 shows an example of wireframe representation of a model. Edges on the far side of the object intersect edges on the near side producing a confusing clutter of line segments. In some cases, wireframe models can be ambiguous and misleading. An edge can belong to more than one surface. It is difficult to distinguish which lines belong to the front of the object and which to the back. Thus, a wireframe model can represent more than one object. Consequently, wireframe models are inconvenient for creating and visualizing complex objects.

4.2.2 Surface Modeling

Surface models define surfaces connecting the edges. Therefore a surface model is a more complete and less ambiguous representation than a wireframe model. It is also richer in its associated geometric contents. Since surfaces are defined with edges, a surface model also consists of wireframe entities. The edges can be displayed to make up a representation that looks like a wireframe model. Alternatively, a surface model can be displayed as a true surface model with nearer surfaces hiding surfaces and edges farther from the viewer as shown in Figure 4.2. This is referred to as a hidden-edge view. When the surfaces are filled in, the model can be displayed with shading view as shown in Figure 4.3. These advantages make objects more identifiable and significantly improve the efficiency of the operation when creating, editing and meshing a model.

The disadvantage of surface representation is that the model is only an empty shell. Since surfaces have no thickness, surface models lack information about physical properties. In other words, surface models do not contain mass property or inertial information. Therefore, while a surface model can show the shape of an object, it does not define other characteristics.

4.2.3 Solid Modeling

Solid models define the entire volume which the object occupies including not only the geometric data (the surfaces and their edges) but also the topological information (the relationships between the edges and surfaces of the object). Thus, a solid model of an object is a more complete representation than is a surface model. However, less

information is required to be input to create a solid model. Some data, for example the intersections of surfaces, will be automatically generated by the model system itself. This feature speeds up the processing of model generation. A solid model is relatively easy and fast to modify in many cases, especially for complex three-dimensional objects. There are many approaches to create a solid model. Boundary representation and constructive solid geometry are the most widely used schemes. Furthermore, existing databases in wireframe form can be converted into solid form (Wesley *et al.*, 1984).

A solid model can be displayed either in wireframe mode (edges only) or in surface mode (a hidden-edge view or a shaded rendering). No matter in what mode it is displayed, a solid model contains all the necessary information to calculate surface area, volume, and center of gravity. If a solid model is associated with a particular material, analysis can also include its weight, moment of inertia, thermal conductivity, etc. It is more like the real world counterparts than the other models. These features make solid modeling the most powerful modeling representation for generating a finite element model.

4.2.4 Boundary Representation

Boundary representation (B-rep) is a popular and widely used scheme to create solid models of physical objects. A B-rep model is based on the topological notion that a physical object is bounded by a set of faces. These faces are regions or subsets of closed and orientable surfaces. A closed surface is one that is continuous without breaks. An orientable surface is one in which it is possible to distinguish two sides by using the direction of the surface normal at a point, towards the inside or outside of the solid model.

Each face is bounded by edges, and each edge is bounded by vertices. Thus, a boundary model of an object is comprised of faces, edges, and vertices linked together to ensure the topological consistency of the model.

The database of a boundary model contains both topology and geometry. Since B-rep systems store only the bounding surfaces of the solid, it is still possible to compute volumetric properties such as mass properties. The speed and accuracy of these calculations depend on the types of surfaces used by the models.

4.2.5 Constructive Solid Geometry

The constructive solid geometry (CSG) scheme is another popular scheme to create solid models of physical objects because it is the best understood representation. In many instances, it is more powerful and efficient than the B-rep scheme. CSG offers representations which are succinct, easy to create and store, and easy to check for validity.

CSG defines objects with the aid of Boolean operators. A CSG model is based on the topological notion that a physical object can be divided into a set of basic shapes called primitives. These primitives can be combined in a certain order following Boolean operations to form the object. Primitives themselves are considered valid CSG models. Each primitive is bounded by a set of surfaces, usually closed and orientable. The surfaces of primitives are combined via a boundary evaluation process to form the boundary of the object, that is, to find its faces, edges, and vertices.

4.3 Computer Graphics

The massive amounts of data that computer generates are often beyond comprehension when displayed simply as a stream of numbers. However, if the data can be shown as a graphical image, then their meaning can often be understood immediately. Computer graphics allows the user to visualize the processes and the results of computations. With the aid of computer graphics, certain alterations of the object can be performed. The geometric model and the finite element mesh can be created efficiently.

4.3.1 Surface Normal

The concept of a surface normal is used in geometric modeling, surface shading, etc. The surface normal defines the direction of a surface. The boundaries of a solid can be represented by a set of surfaces with directions. The direction of a surface can be defined by its surface normal. Assume that vectors $V_1 = P_1 - P_2$ and $V_2 = P_2 - P_3$ are contained within surface S as shown in Figure 4.4. The surface normal N_s of the plane is the cross product of V_1 and V_2

$$N_s = V_1 \times V_2 = \begin{vmatrix} i & j & k \\ x_2 - x_1 & y_2 - y_1 & z_2 - z_1 \\ x_3 - x_2 & y_3 - y_2 & z_3 - z_2 \end{vmatrix} \qquad (4.1)$$

This equation can also be written as

$$\begin{bmatrix} x_1 & y_1 & z_1 \\ x_2 & y_2 & z_2 \\ x_3 & y_3 & z_3 \end{bmatrix} \begin{Bmatrix} A \\ B \\ C \end{Bmatrix} = \begin{Bmatrix} -D \\ -D \\ -D \end{Bmatrix} \tag{4.2}$$

where

$$A = \begin{vmatrix} 1 & y_1 & z_1 \\ 1 & y_2 & z_2 \\ 1 & y_3 & z_3 \end{vmatrix}, \quad B = \begin{vmatrix} x_1 & 1 & z_1 \\ x_2 & 1 & z_2 \\ x_3 & 1 & z_3 \end{vmatrix}, \quad C = \begin{vmatrix} x_1 & y_1 & 1 \\ x_2 & y_2 & 1 \\ x_3 & y_3 & 1 \end{vmatrix}, \quad D = -\begin{vmatrix} x_1 & y_1 & z_1 \\ x_2 & y_2 & z_2 \\ x_3 & y_3 & z_3 \end{vmatrix}$$

Thus, any point (x, y, z) can be defined as internal or external of the surface as follows:

$$Ax + By + Cz + D < 0, \text{ internal} \tag{4.3}$$

$$Ax + By + Cz + D > 0, \text{ external} \tag{4.4}$$

4.3.2 Homogeneous Transformations

Homogeneous transformations involve translation, rotation, scaling and any combination of them. These transformations can be used on two different occasions. First, when an object is to be constructed, these transformations are used to properly orient and position the primitives before applying specified operations. Second, if the solid is to be transformed after its construction, the transformation operations must be applied to all faces, edges, and vertices of a B-rep solid or all primitives of a CSG solid.

Transformations can be applied directly to the parametric representations of objects such as points, curves, surfaces, and solids. Transformation of an object represented as a set of lines, surfaces or solids is carried out by transforming the coordinate values for each vertex. The set of transformed coordinate position of the vertices then defines the new

position of the object. Matrix notation provides a very expedient way of developing and implementing geometric transformations.

In a three-dimensional homogeneous coordinate representation, a point being translated from position (x, y, z) to position (X, Y, Z) with distances (a, b, c) can be expressed as

$$
\begin{pmatrix} X \\ Y \\ Z \\ 1 \end{pmatrix} = [T] \begin{pmatrix} x \\ y \\ z \\ 1 \end{pmatrix} = \begin{bmatrix} 1 & 0 & 0 & a \\ 0 & 1 & 0 & b \\ 0 & 0 & 1 & c \\ 0 & 0 & 0 & 1 \end{bmatrix} \begin{pmatrix} x \\ y \\ z \\ 1 \end{pmatrix}
\tag{4.5}
$$

Rotating a point from position (x, y, z) to position (X, Y, Z) with angle θ in the x-y plane around the origin can be expressed as

$$
\begin{pmatrix} X \\ Y \\ Z \\ 1 \end{pmatrix} = \left[\mathbf{R}_{xy}(\theta) \right] \begin{pmatrix} x \\ y \\ z \\ 1 \end{pmatrix} = \begin{bmatrix} \cos\theta & -\sin\theta & 0 & 0 \\ \sin\theta & \cos\theta & 0 & 0 \\ 0 & 0 & 1 & 0 \\ 0 & 0 & 0 & 1 \end{bmatrix} \begin{pmatrix} x \\ y \\ z \\ 1 \end{pmatrix}
\tag{4.6}
$$

while to rotate a point from position (x, y, z) to position (X, Y, Z) with angle ϕ in the x-z plane around the origin, the expression is

$$
\begin{pmatrix} X \\ Y \\ Z \\ 1 \end{pmatrix} = \left[\mathbf{R}_{xz}(\phi) \right] \begin{pmatrix} x \\ y \\ z \\ 1 \end{pmatrix} = \begin{bmatrix} \cos\phi & 0 & -\sin\phi & 0 \\ 0 & 1 & 0 & 0 \\ \sin\phi & 0 & \cos\phi & 0 \\ 0 & 0 & 0 & 1 \end{bmatrix} \begin{pmatrix} x \\ y \\ z \\ 1 \end{pmatrix}
\tag{4.7}
$$

4.3.3 Parallel Projection

Let (e_x, e_y, e_z) denote the coordinates of the viewer's eye, then the rotation angles are

$$\phi_e = \tan^{-1} \frac{e_y}{e_x} \tag{4.8}$$

$$\theta_e = \tan^{-1} \frac{e_z}{\sqrt{e_x^2 + e_y^2}} + \frac{\pi}{2} \tag{4.9}$$

The procedure for parallel projection is i) translate the point to the origin with distance (-e_x, -e_y, -e_z); ii) rotate the point in the x-y plane with angle -θ_e around the origin; iii) rotate the point in the x-z plane with angle -ϕ_e around the origin; iv) rotate the point in the x-y plane with angle -90° around the origin. Thus, the parallel projection matrix is

$$\left[\mathbf{T}_p\right] = \left[\mathbf{T}\!\left(-e_x, -e_y, -e_z\right)\right]\!\left[\mathbf{R}_{xy}\left(-\theta_e\right)\right]\!\left[\mathbf{R}_{xz}\left(-\phi_e\right)\right]\!\left[\mathbf{R}_{xy}\left(-90°\right)\right] \tag{4.10}$$

4.3.4 Surface Shading

An intensity model such as a surface model or a solid model can be applied to surface shading in various ways depending on the type of surface and the requirement of a particular application. Constant shading is used in this study. An object with plane surfaces can be shaded realistically by using constant surface intensities. For a surface illuminated by a point source, the shading model produces a constant surface intensity. A curved surface which is represented as a set of plane surfaces can be shaded with constant surface intensities if the planes subdividing the surfaces are made small enough. This method can generate a reasonably good display when surface curvature changes gradually and light sources and the view position are far from the surface.

More elegant schemes include Gouraud shading which linearly varies the intensity between all the adjacent planes, and Phong shading, which approximates the surface normal at each point then computes the intensity. However, since the geometric models generated in this research do not contain any curved surface, these advanced shading schemes made the shading view no difference than a constant shading view.

4.4 Mesh Generation

Mesh generation, which forms the backbone of the FEM, refers to the generation of nodal coordinates and elements. Although a number of algorithms and software packages for mesh generation have been developed, both geometrical and physical constrains during the generation of a finite element mesh still present difficulties. To mesh a complex object can even require to use more than one algorithm. Mesh generation may generally be classified into parametric and automatic generation schemes. This section reviews the methods of finite element mesh generation used in this study, in particular, quadrilateral and hexahedral element mesh generation.

4.4.1 Parametric Mesh Generation

Parametric methods refer to interactive mesh generation methods or semi-automatic methods, which require user interaction to specify essential parameters. The parametric mesh generation methods provide the most control to the user and require more description about the geometry of the model. These methods can be divided into two categories: the wireframe- and surface-based category and the solid-modeling-based

category. Within each category, methods can be further classified into the node-based approach and the region-based approach.

Wireframe- and Surface-Based Methods

Some methods represent early attempts to automate manual generation (Carey *et al.,* 1984). Other schemes have been developed to utilize the parametric representation of curves and surfaces. Typically, these methods require the user to aid the generation process. Graphical aids are usually required to assist the user in identifying the relatively large amount of information involved.

The node-based approach to mesh generation considers nodes to be the primary control factor of the mesh and therefore generates them first. The nodes are then connected to form elements. Various types of elements can be generated. Element generation may be followed by a mesh refinement step, possibly with element rearrangements, to produce a more reasonable mesh. The mesh refinement step can be avoided if all the nodes in the final mesh are generated in compliance with mesh density specifications. In such a case, the algorithm has only to consider how to connect the nodes to form elements as smooth as possible.

Recursive subdivision is a commonly used method to generate triangular and quadrilateral elements. This method is based on recursively dividing the object to be meshed into subdivisions and generating nodes along their boundaries. This method can be used to mesh objects with planar, multiply-sided, simply-connected regions, that is , without holes. The mesh density along the region boundaries needs to be specified. Multiply-connected

regions, that is, with holes, must be reduced to simply-connected regions by connecting hole boundaries to outer boundaries. The procedure can be described as follows for two-dimensional regions. First, specify the mesh density required for the various curves which form the region boundary. Second, if there are any holes, connect the holes to the outer boundary of the region. A one-dimensional node generator is used to create nodes on the connected boundary, based on the mesh density. Thus, a polygon of nodes is obtained. Split the polygon along the "best splitting line" and generate nodes along this new line according to the mesh density, resulting in two subpolygons. This process is continued until all subpolygons have been reduced to trivially simple polygons, which are the results of the meshing.

For three-dimensional regions, the boundary surfaces are meshed first. This results in a polyhedron. Then the "best splitting plane" is determined, and nodes and faces are generated on this plane. These faces are added to both halves of the region, resulting in two subpolyhedra. This process is continued until all subpolyhedra have been reduced to simple polyhedrals. In this way, by dividing subpolyhedra into tetrahedra, solid finite elements are generated.

The region-based algorithm is another widely used mesh generating method. This algorithm is based on the fact that a region can always be subdivided entirely into quadrilaterals if the polygon which forms the boundary of the region has an even number of sides. This approach requires subdividing the object into regions with specific topologies, mostly four-sided regions. Within each region, the mesh is generated automatically by mapping the region into a regularized domain, normally a quadrilateral.

The total mesh is obtained by merging or piecing the individual meshed regions together. The common sides that neighboring regions share must have the same number of nodes. This requirement can be enforced manually or algorithmically while generating the meshes of the neighboring regions.

Solid-Modeling-Based Methods

Some of the above described meshing methods can be extended to solid models (Shephard *et al.,* 1984). However, due to the original designs, these methods can only work on the faces and edges of the solid. Therefore, these approaches do not fully utilize the information which characterizes a solid. Faces and edges need to be extracted from the solid database before using a meshing method.

4.4.2 Automatic Mesh Generation

These methods are primarily based on solid modeling theory and operate on solid models achieving full automation. A fully automatic mesh generator can be invoked at the user level by identifying mesh attributes and the solid. This implies that mesh automation limits user interaction to defining the solid and specifying mesh density parameters.

Node-based approach

One of the methods based on this approach is the Boolean-based method. This method utilizes the CSG representation of a solid, particularly the CSG tree data and Boolean operations, to generate a mesh. Two steps are required for this method to generate a mesh. First, the method places well-distributed nodal points inside each primitive. The

CSG tree is then traversed to combine these nodal points. The method follows a predefined set of rules to decide how to merge the nodal points in the overlapped zones. The method utilizes a divide-and-conquer algorithm and a point membership classification technique in the merging process. Once the nodal points are merged, they are then connected to create the elements. Where quadrilateral elements are not feasible to be generated due to the difficulty in geometry, triangular elements are generated, thus, a mixed element mesh is created.

Element-based approach

The approach is based on subdividing the domain of an object into a set of valid elements directly instead of subdividing the domain into regions first. Recently developed techniques include octree (Mantyla, 1988), looping (Talbert *et al.*, 1990), paving (Blacker *et al.*, 1991; Cass *et al.*, 1996), plastering (Blacker *et al.*, 1993), grid based (Schnelders, 1995; Weller *et al.*, 1996), whisker weaving (Tautges *et al.*, 1996).

4.5 General Description of COSMOS/M

COSMOS/M is an integrated finite element analysis software package designed for pc's and workstation's. The program consists of a pre- and postprocessor, various analysis modules, interfaces, translators and utilities.

GEOSTAR, the pre- and postprocessor, provides the capability of creating a geometric model, generating finite element mesh and visualizing the analysis results. The geometric modeling abilities of GEOSTAR are based on the boundary representation (B-rep) scheme. A comprehensive list of geometry-related commands makes geometric modeling

quick and accurate. Due to the lack of the ability of constructive solid geometry (CSG), generating complex geometric models is less efficient. GEOSTAR provides a neutral file interface which enables the user to exchange data in neutral file forms of the IGES and DXF types between COSMOS/M and other FEA and CAD software packages. This feature is designed to enable user to take the advantages of other software packages. However, neutral files generated by GEOSTAR do not work properly with other software packages. For instance, GEOSTAR can not translate some non-standard geometric entities defined by GEOSTAR itself into either IGES or DXF format.. On the other hand, GEOSTAR ignores many geometric entities when importing IGES and DXF files generated by other software. Thus, the file importing and exporting may cause loss of information

A finite element mesh can be generated by a parametric (semi-automatic) or an automatic mesh generator built within GEOSTAR. For most element types, the generator can generate a mesh with a constant mesh density within an object. Only for trianglar elements (including shell, plane stress/strain elements), can different mesh densities be defined within an object. Adaptive analysis is supported by triangular and tetrahedral elements (Lai *et al.*, 1992).

A user-defined material model interface allows the specified material model to be linked with COSMOS/M so that analysis can be carried out. However, the linkage can not be carried out on a pc unless two additional software packages are available.

COSMOS/M consists of a large collection of analyses modules for solving problems of linear and nonlinear static and dynamic, heat transfer, fluid mechanics, electromagnetics

and structural optimization. Fast finite element (FFE) technology is employed to speed up the analysis of complex finite element problems. This new technology enables COSMOS/M to analyze complex problems up to 100 times faster than conventional programs while reducing disk storage requirements up to 20 times (Hamilton, 1995).

4.6 Interface Programs

4.6.1 Objectives

Due to the fact that COSMOS/M can not be directly linked with a material model driver on a PC, it has been used as a pre- and postprocessor only in this study. The finite element models were generated by COSMOS/M and FEMAP. The databases were then extracted and analyzed by the finite element solver PLASTEX (for two-dimensional problems) or DARC (for three-dimensional problems). COSMOS/M was then used to provide a visual representation of the results. In the process, several interface programs have been developed to facilitate the operation. The objectives of the interface programs were as follows: i) to extract the finite element database; ii) to convert node numbers from a scattered state into an optimized order; iii) to convert the element local node numbers in order to ensure a positive Jacobian determinant for each element; iv) to generate a new finite element database containing elements for the concrete material only; v) to write a finite element database file in the format of the input file for the finite element solver.

4.6.2 COSMOS/M Finite Element Database Interfaces

COSMOS/M stores most of database in binary format. A library file and a sample database utility program written in FORTRAN77 is supplied to enable the user to communicate with the binary database files. The program provides an easy and straightforward way to extract the finite element database. However, this utility program is potentially risky and troublesome. It may occasionally halt the machine and even destroy the binary database. In addition, this program is not able to convert the node numbers into the optimized order. Thus, a second program is required to do the required conversion. To display the finite element analysis results, yet another program is required to convert the node numbers back.

As an alternative, the finite element database can be stored in ASCII format files in COSMOS/M. The necessary information for interface manipulation can be obtained from the ASCII database file with the GFM extension. Communication with an ASCII file is safer. All of the interface manipulation can be built within a single program, which is more efficient to use than three separate programs.

The GFM file can be generally divided into six sections and contains almost all of the finite element information (Figure 4.5). The first section contains information on geometric entities. When generating a GFM file, COSMOS/M provides an option to include or exclude this information and the interface program should work properly in either case. The second section contains information on the element group set, material group set, etc. The third section contains nodal point information. The next section is element information. If the geometric information is included in this file, each element record is

followed by information indicating the relation of the current element with its corresponding geometric entities. The interface program should again be able to work automatically in either format. The following section, which comes with two different formats, contains displacement constraints information. In one format, each record describes the constraint in a degree of freedom; in the other, each record describes the constraints at a nodal point. The last section contains pressure load information, indicating the element number and face number on which the pressure is applied, and the pressure value.

The nodal point numbers are generated in a scattered state. COSMOS/M provides a function which optimizes the node numbers to minimize the profile of the stiffness matrix. The results of node renumbering are written to an ASCII file with extension RNM. There is no way to change the node numbers either in the binary database or in the ASCII database into optimized order.

The format of an RNM file can generally be divided into two sections, Figure 4.6. The first part includes some description and control data. Among them, only the node and element numbers are used in the interface program. The second part contains three columns of data. The first column contains old nodal point numbers, which are in a scattered state. The second column contains the optimized nodal point numbers. The data in the third column is not relevant here. It should be noted that neither the GFM file nor the RNM file contain the total number of constrained degrees of freedom and the total number of elements with pressure loads.

In COSMOS/M, the element local nodal point direction is generated according to the direction of the corresponding geometric entity. For a model with several geometric entities, there is virtually no way to describe all the entities with the same direction. This results in a disorder of the element local nodal point direction. Some of them are clockwise; while others are counter-clockwise. There is a built-in procedure in the COSMOS/M solver to rearrange the element local node direction. However, COSMOS/M does not provide an interface for user access to the rearranged database. In fact, COSMOS/M discharges the renumbered element information right after the solution processing has finished. To ensure a positive Jacobian determinant for each element, the interface program should provide the ability to rearrange the element local node direction.

A postprocessing visualization interface is provided by COSMOS/M to allow user-defined scalar parameters to be displayed and printed. For vector operators, only one of the components can be read and displayed at a time.

4.6.3 Schemes of Interface Operation

The finite element solvers PLASTEX and DARC used in this research are written in Fortran77, thus unable to be modified reading data directly from the ASCII database files. Two schemes of interface operation are proposed. The first one is for communicating with COSMOS/M ASCII files. The second one is for extracting information from the COSMOS/M binary database.

Figure 4.7 shows the first scheme. The geometric model and finite element model are generated by using COSMOS/M and FEMAP. The interface program COS2PLAS reads

the finite element database from COSMOS/M ASCII files having the GFM and RNM extensions. After converting, COS2PLAS creates three files. The DAT file contains the input data for the finite element solver. The NEW file contains the converted finite element database in the GFM format. This file will be used by COSMOS/M to generate a new finite element database which is used for graphical representation of the results. Since both the NEW file and analysis results are in converted mode, the results can be displayed directly in the database generated with the NEW file. This strategy avoids converting the analysis results back to the unconverted mode. The N12 file is a subset of the NEW file, and contains the filtered finite element database for which a specified parameeter is valid. In particalar, the concrete hardening parameter β is valid only for the concrete dam. Thus elements corresponding to the dam are stored in N12 file, while elements coresponding to rock and soil are screened out. The N12 file is used by COSMOS/M to generate a binary database for plotting β contours. The finite element analysis results are stored in the COS file, which can be displayed by COSMOS/M. Program DEFOMESH generates two deformed mesh files: DEF, which contains the deformed shape of the entire model and D12, which contains the deformed shape of the dam structure only. Both DEF and D12 files can be plotted by COSMOS/M.

The second scheme is outlined in Figure 4.8. Program EXTRA extracts the finite element database from COSMOS/M binary files. The LINK1 program converts the node numbers and generates the input file for the finite element solver. The node numbers in the finite element analysis results are converted back by the LINK2 program.

4.6.4 COS2PLAS -- An Interface Program Converting COSMOS/M ASCII Database Files into PLASTEX Input File

The interface program COS2PLAS is designed to bridge the gap between COSMOS/M and PLASTEX. The program reads GFM and RNM files first. Then, it converts the node numbers, the displacement boundary conditions, the pressure loads and the directions of the element local node numbers. Finally, it writes the results to an ASCII file with extension NEW in the format of the GFM file, writes the filtered information in an ASCII file with extension N12, and writes the results as a PLASTEX input file.

The tasks of converting include: 1) Converting the node numbers (including those for displacement boundary conditions) from the scattered state into optimized order; 2) Converting the pressure loads from being applied on the element faces to being applied at the element local nodes; 3) Unifying the element local node orders. In order to convert the element local node direction, the signs of the Jacobian determinant is computed for each element.

The purpose of the NEW file is to enable finite element analysis results to be displayed directly without any further manipulation. The format of NEW file is the same as the GFM file. Once COSMOS/M reads the NEW file, a new finite element database is established. The finite element analyses results can be displayed directly.

Some parameters in finite element analysis results are valid only for particular material sets, and void for others. For example, β values are valid only for concrete material sets, and void for the rock and soil material sets in this study. However, the postprocessing

program in COSMOS/M treats the β values in rock and soil as zeros. The postprocessor then plots contours not only in concrete regions but also in the rock and soil regions resulting in nonsense contours.

To obtain correct contours, an element filter is designed in the interface program COS2PLAS. The element filter enables the interface program to create a file containing only the necessary elements and corresponding nodes for which β values are valid. The other element information will be screened out. This file can be used for COSMOS/M to generate a special model database which guarantees the β contour to be plotted free of distortion.

The source code of the interface program COS2PLAS is shown in Appendix A. This program is a two-dimensional version, and is easy to be modified into a three-dimensional one.

4.6.5 DEFOMESH -- A Deformed Mesh File Generating Program

COSMOS/M provides a postprocessing interface which allows user-defined scalar parameters to be plotted. For results in vector form, only one of the components can be read and displayed. However, in some cases, a vector field plot is desirable. A simple scheme is presented in this section to enable COSMOS/M to plot vector fields in the form of a deformed mesh.

For node i with its original nodal coordinates x_i and displacements d_i, the deformed nodal coordinates $\mathbf{x}_i^d$ can be expressed as

$$\mathbf{x}_i^d = \mathbf{x}_i + S\mathbf{d}_i \qquad\qquad (4.11)$$

where S is a scaling factor of the deformed shape. To enable the deformed mesh to be overlapped with the original mesh, the node and element numbers in the deformed mesh need to be offset.

Due to the fact that COSMOS/M does not provide a line type choice, the only way to identify the two overlapped meshes is to use different colors. Therefore, the original and deformed mesh models are defined using different element groups, which are allowed to be defined in different colors in COSMOS/M.

The source program of DEFOMESH is shown in Appendix B.

It should be noted that a three-dimensional deformed mesh can be displayed as a wireframe view only using this method. This is due to the fact that COSMOS/M needs the database file containing not only finite element information but also geometric information to display the surface view or shading view.

4.6.6 A Interface Scheme Extracting Information from COSMOS/M Binary Database

Finite element database can also be extracted from the COSMOS/M binary database files. A library file and a sample database utility program is included in COSMOS/M package. The source code EXTRA is obtained by modifying the sample code supplied with COSMOS/M. Program EXTRA extracts the finite element database from COSMOS/M binary files, and then writes the database in an ASCII file. The program LINK1 converts

the node numbers in the database into an optimized order, and then generates the input file for the finite element solver. Finally, the program LINK2 is used to convert the node numbers in the finite element analysis results back, and writes a data file for COSMOS/M to plot contours.

The advantage of this scheme is the economy of memory use since it separates the work into three stages: 1) extracting information from the COSMOS/M binary database; 2) converting the finite element database into an optimized nodal order; and 3) converting the nodal order in the finite element analysis result back to the scarttered state for plotting. The main disadvantage of this scheme is its complexity. Thus, this scheme is suitable for large finite element models when the amount of memory is a critical problem, and the requirements for postprocessing are simple.

EG   CLR
1
2

83
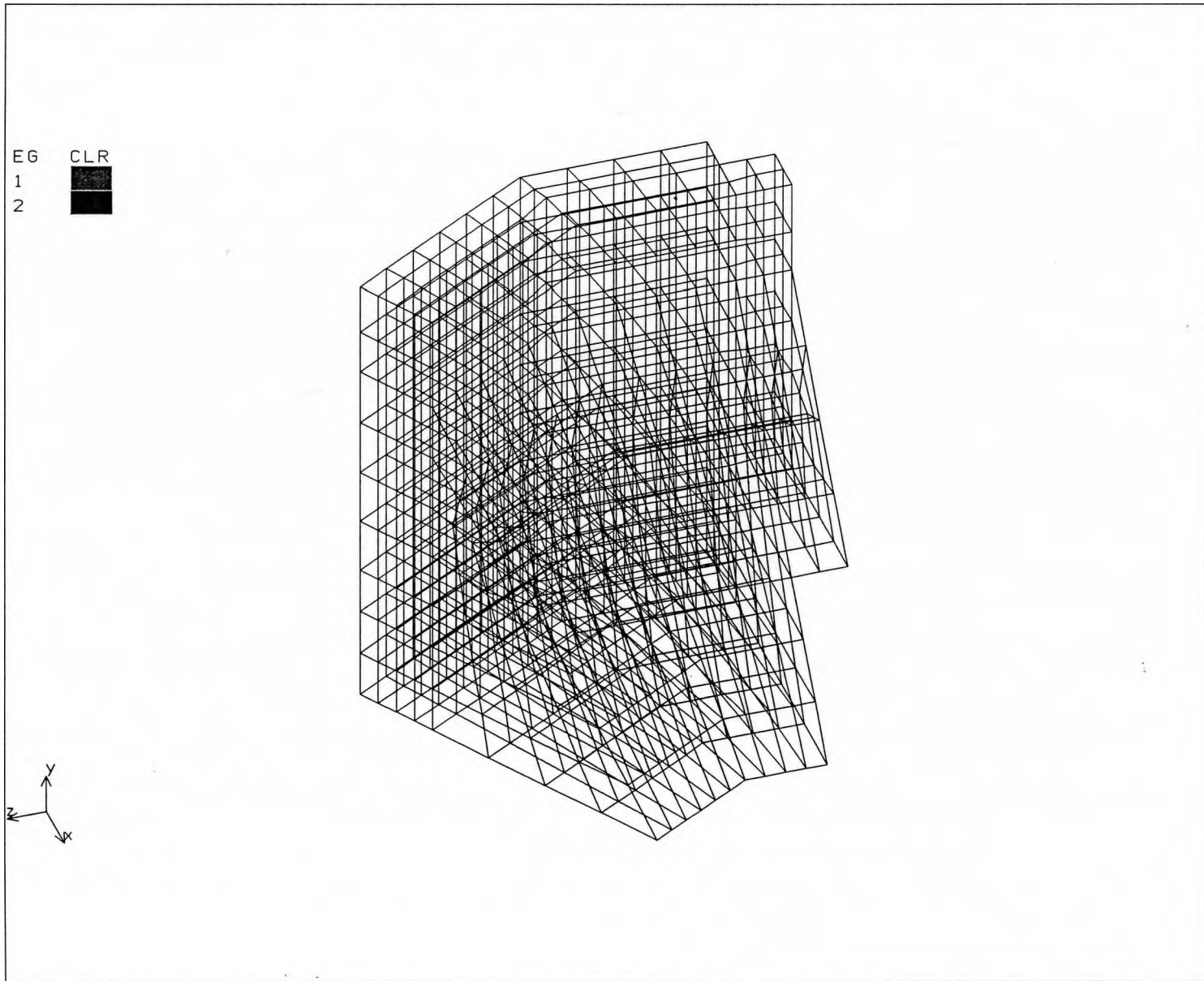
Figure 4.1   Wireframe representation of a junction structure.

EG CLR
1
2

Figure 4.2   A surface model of a junction structure.

84
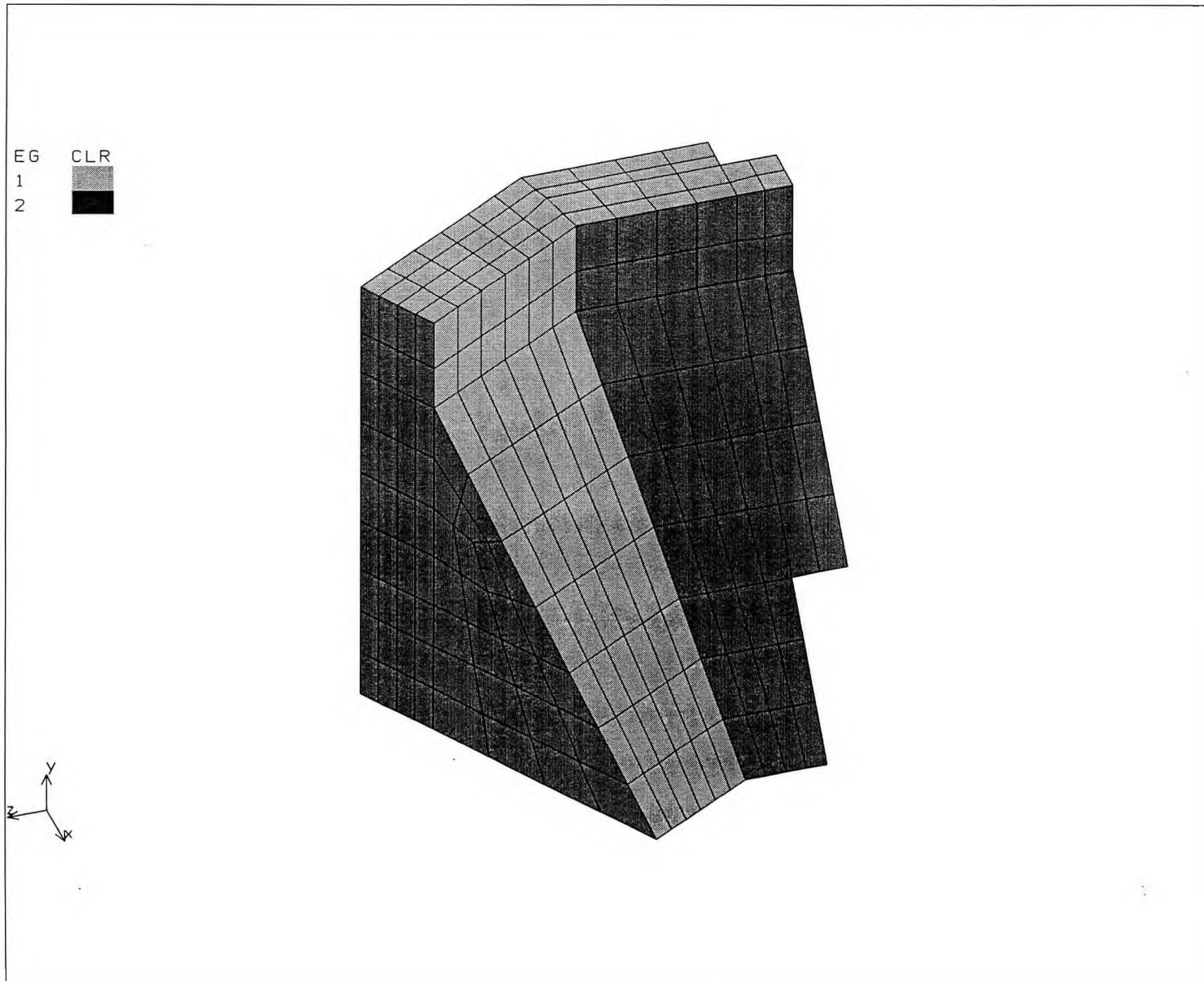
Figure 4.3   A surface model of a junction structure with constant shading.
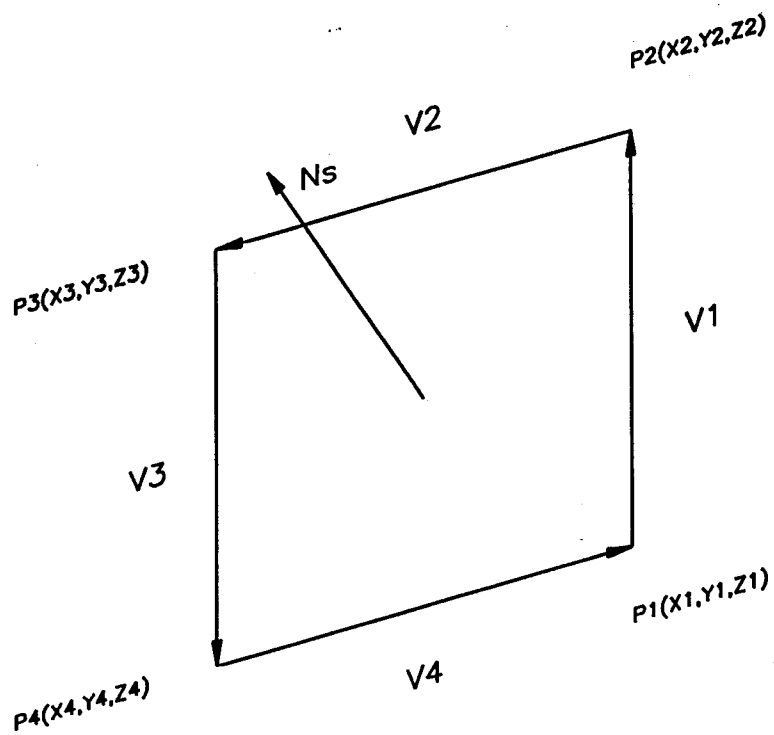
Figure 4.4 Surface Normal.

```
                DATE:  3/**/1996     TIME: **:57:22

Number of nodes      = 1437
Number of elements   =  448



Before resequencing - - -
      Node difference        1330
      Profile            766626
      Average node difference    510.40
      RMS node difference      578.60

After resequencing by  GPS
      Node difference         106
      Profile             79713
      Average node difference     53.07
      RMS node difference      58.01

       1       574        117
       2       383        736
       3       206        739
       4       139        118
       5       190        737
       6       263        740
       7       332        119
       8       414        741
       9       484        120
      10       666        743
      11       828        744
      12       945        121


. . . . . .

    1495       255         97
    1496       232         83
    1497       193         73
    1498       195         67
    1499       261         64
    1500       239         63
    1501       198         62
    1502       199         54

The time required to reduce the Bandwidth is ******** Seconds
```

Figure 4.5 Format of COSMOS/M RNM file

```
PT, 1 0 0 0
PT, 2 17.3 0 0
PT, 3 0 22.1 0

......

EGROUP, 1 PLANE2D , 0, 1, 2, 1, 0, 0, 0, 0,
EGROUP, 2 PLANE2D , 0, 1, 0, 0, 0, 0, 0, 0,
EGROUP, 3 PLANE2D , 0, 1, 2, 1, 0, 0, 0, 0,
EGROUP, 4 PLANE2D , 0, 1, 2, 1, 0, 0, 0, 0,
MPROP, 1, EX,         200000

......

ACTSET CS 0
ND, 1,              11              7          0 12 17 2 C 1 1
ND, 2,       7.1333332       7.5166664         0 0 17 3 0 1 1
ND, 3,       3.8666663       8.5933342         0 0 17 3 0 1 1

.....

ND, 1502,      -41.442566          -45         0 0 0 0 0 0 0
ACTSET EG 1
ACTSET MP 1
ACTSET RC 1
ACTSET ECS -1
EL,    1, RG 1, 8    10    20   21   19  561  562  563  564   0  0  0  0 -1  0
EL,    2, RG 1, 8     2    23   24   22  565  566  567  568   0  0  0 17 -1  0
EL,    3, RG 1, 8    15    26   27   25  569  570  571  572   0  0  0  0 -1  0

......

EL,   69, SF 3, 8    58    94   96   89  717  682  715  711  21  0  0  0  3  0
ACTSET EG 2
ACTSET MP 2
ACTSET RC 2
EL,   70, SF 2, 8    14    98    1   17  718  719  609  604   5  0 18  7  2  0
EL,   71, SF 2, 8    98    99   68    1  720  721  686  719   5  0 18  0  2  0
EL,   72, SF 2, 8    99   100   55   68  722  723  654  721   5  0 18  0  2  0

......
EL,  448, SF 3, 8   374   375  560  423 1501 1498 1500 1502   0  0  0  0  3  0
DND, 129, UX,              4,
DND, 129, UY,              4,
DND, 129, UZ,              4,

......

ACTSET LC 1
PEL, 8,        131.16068 4 8 1 4
PEL, 10,       157.85559 4 10 1 4
PEL, 11,       188.69202 4 11 1 4

......

PEL, 421,           196 1 421 1 4
PEL, 422,           196 1 422 1 4
PEL, 423,           196 2 423 1 4
TOFFSET,       273
TREF,          70
```

Figure 4.6 Format of COSMOS/M GFM file.
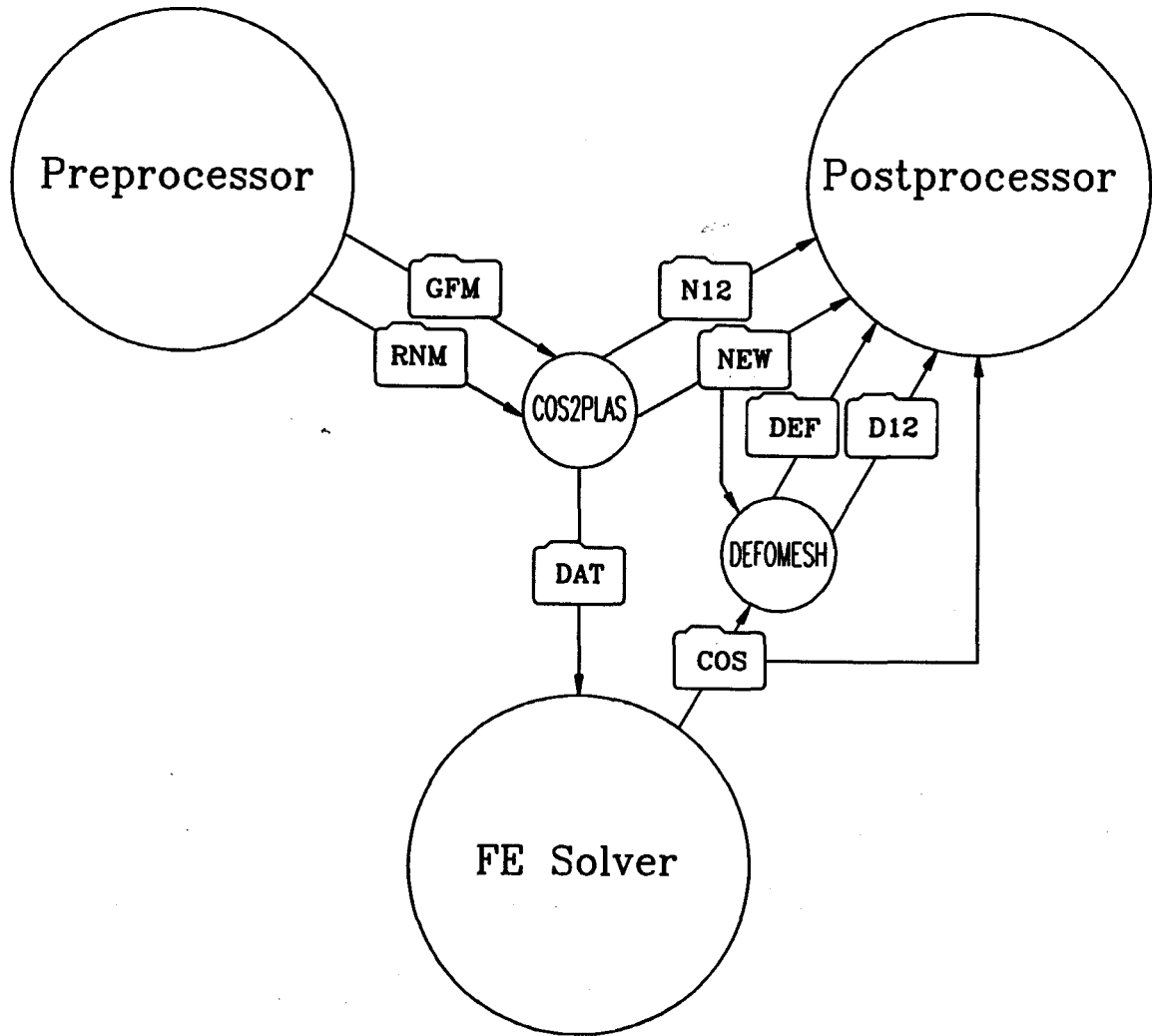
Figure 4.7   Interface scheme based on communicating with COSMOS/M ASCII files.
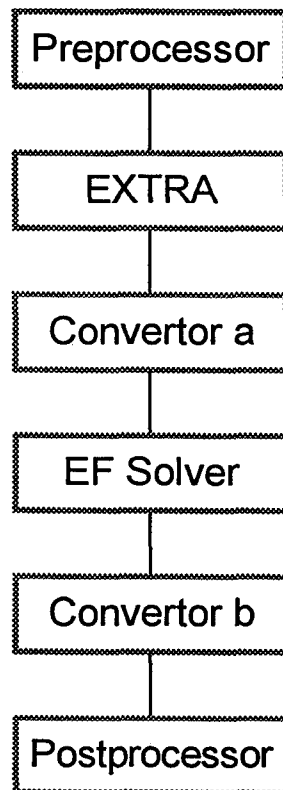
Figure 4.8   Interface scheme based on communicating with COSMOS/M binary files.

Chapter 5

Finite Element Modeling and Analysis of Beauharnois Powerhouse Structures

5.1 Introduction

The Beauharnois Powerhouse is located on the St. Lawrence River about 50 km upstream from Montreal. The complex consists of 37 principal units and 2 auxiliary units encased between two concrete dams located on the south and north abutments (Figure 5.1). The powerhouse units were built in three stages. The construction started in 1928 with the first phase referred to as Beauharnois 1, which was completed in 1935. The second and the third phases, Beauharnois 2 and 3, were completed in 1951 and 1961, respectively. The total length of the concrete structures, including two wing dams, is 1034 m. The height of the intake structures is approximately 29 m. The height of the south wing dam (right wing dam) is approximately 22 m and the height of north wing dam (left wing dam) is approximately 19.5 m. Quartzitic sandstone, which contains chalcedonic silica, has been used as coarse aggregate.

Since the early 1960's, Beauharnois powerplant has been experiencing problems resulting from concrete expansion. A preliminary study which started in 1982 (Albert *et al.*, 1987) investigated the cause of the problem. Concrete core samples, taken from different parts of the complex, have been tested to evaluate the expansion rate. The investigation concluded that the alkali-silica reaction was the principal cause for the abnormal behavior of the concrete. The structural problems experienced at Beauharnois powerhouse include:

i. significant residual deformations in the longitudinal direction of the water intake structures;

ii. the development of structural cracks at the junction structures between the water intakes and the concrete wing dams;

iii. the deterioration of concrete works exposed to weathering or conditions of relatively high humidity;

iv. the vertical and horizontal cracking in wing dams;

v. the throat ring ovalling in the end units of powerhouses 1 and 3.

These structural problems caused severe operational problems, such as reduction of clearances between the turbine runner blades and throat rings. To remedy the damage, slot cutting has been carried out in unit 5 in 1984; then, a partial cutting has been carried out between units 35 and 36 in 1984.

More recent investigation (Gocevsky, 1993), which involved measurement of displacements accumulated over 25 years for each wing dam and water intake unit (Figures 5.2 to 5.5), concluded that the concrete still has a potential for further expansive reaction.

This chapter focuses on the application of the constitutive model described in Chapter 3 to analyse the behaviour of two typical units of the Beauharnois complex. First, the south wing dam is modeled as a two-dimensional structure under isothermal condition. In the second example, the influence of seasonal temperature variations is taken into

consideration. Finally, a three-dimensional analysis of the water intake structure is performed.

5.2 Finite Element Modeling of Concrete Dam Structure

5.2.1 Purpose of the Analysis

The basic purpose of the analysis is to predict the misalignment, macro- and microcracking of the south wing dam due to continuing AAR under isothermal condition. A parametric study of the influence of concrete relative humidity on the AAR-induced deterioration is carried out. In addition, the influence of the stiffness of the foundation is investigated. In particular, two finite element models are compared here: i) the dam founded on a rigid foundation (zero displacement along the bottom of the dam); ii) the dam-foundation system, which enables the dam-foundation interaction to be taken into consideration.

5.2.2 Modeling

All units of the Beauharnois complex are concrete gravity structures and are founded on a firm rock known as the Potsdam sandstone. A typical cross section of the south wing dam, Figure 5.6, is chosen for two-dimensional simulations. The height of the structure is 22.1 m. The height of the reservoir is 19.68 m. On the downstream side of the dam, there is an approximately 5.77 m high backfill.

Concrete expansion rate

The relative humidity of the concrete directly influences the AAR expansion rate. In order to evaluate the relative humidity, samples were taken from different places. A recent investigation of Beauharnois Powerhouse (Albter *et al.*, 1987) concluded that relative humidity increases rapidly with depth. The depth at which the level of 85% relative humidity is attained varied between 75 mm and 350 mm below the exposed concrete surfaces. An investigation of five concrete dams in the U.S. (Stark, 1985) led to a similar conclusion: most of the concrete mass within the dam structure appears to contain sufficient moisture to trigger AAR expansion; only the concrete within several inches of exposed surfaces is sufficiently dry to preclude AAR expansion. Figure 5.7 shows a typical relative humidity distribution for Coolidge Dam (after Stark, 1985). Based on these results, the dam analyzed here is divided into two zones with different AAR expansion rates as shown in Figure 5.8. Most of the concrete within the dam is assumed to have a high relative humidity which enables AAR to be fully developed. The concrete near the exposed surfaces is assumed to have a lower relative humidity which causes a lower rate of expansion. In this analysis, the expansion rates in this zone are assumed to be 0%, 30% and 100% of the full expansion rate, respectively.

Boundary conditions

The stiffness of the foundation may be a major factor influencing the results of the analyses. To investigate this aspect, two models of the dam are considered. Model 1, Figure 5.9, assumes fixed-bottom boundary conditions (infinite stiffness of the foundation). The concrete dam is divided into 122 4-node quadrilateral plane-strain

elements. Model 2 includes a part of the foundation, Figure 5.10. The dam-foundation system is meshed with 448 4-node quadrilateral plane strain elements.

Material properties

The material properties of concrete are E_c = 15,000 MPa, ν = 0.2, f_c = 27 MPa, and f_t = 0.1 f_c. The rock foundation and the backfill soil are assumed to be linear elastic materials. The Young's module of the rock foundation are taken as 0.5, 1.0 and 1.5 E_c, respectively, and ν = 0.2. For the backfill soil, E_s = 0.1 E_c, and ν = 0.2. The only experimental information on the rate of AAR expansion, available at this stage, is that pertaining to the rate of free expansion. Based on this information (Gocevski, 1993), A_2 was identified as 6.329x10^{-7} /day, which corresponds to a principal strain rate of 0.000077 per year. The remaining parameters were chosen as A_1 = 0.1; A_3 = 51.95; A_4 = 17.32. The values of A_3 and A_4 correspond to 30 % reduction in elastic modulus and 10 % reduction in compressive/tensile strength after 25 years of continuing reaction (Kladek *et al.*, 1995).

Solution scheme

The analysis was carried out in two stages. First, the solution due to self-weight of the structure was obtained. The second stage of the analysis was the simulation of the AAR continuing for the period of 25 years. The solution procedure incorporated the modified Newton-Raphson scheme.

5.2.3 Results and Discussion

Results for the dam on the rigid foundation

Figures 5.11 and 5.12 show the horizontal and vertical displacement fields for the dam placed on the rigid foundation, after 25 years of continuing reaction. The horizontal displacements are increasing from the center to both sides, with zero displacement along the bottom boundary. The horizontal displacement at the dam crest is approximately 9 mm towards the reservoir side. The vertical displacement is zero at the bottom of the dam and increases gradually along the height. The maximum vertical displacement at the dam crest is 55 mm. The distribution of the β field, at 25 years of continuing reaction, is shown in Figure 5.13. In this analysis, the rate of free expansion along the exposed surfaces was assumed to be at 30% of that inside the dam. The differential expansion results in high tensile stresses along the exposed surfaces, leading to $\beta > 1$. Thus, macrocracks develop along these surfaces. The fixed-bottom boundary causes high tensile stresses at the bottom of the dam. The high tensile stresses lead to high β values, indicating macrocracks developing near the bottom boundary.

Results for the dam-foundation system

Figure 5.14 shows the deformed shape of the dam-foundation system, after 25 years of continuing reaction. The results correspond to the elastic modulus of the foundation taken as 1.5 E_c. The horizontal displacement field of the dam is shown in Figure 5.15. At the reservoir side of the dam, the horizontal displacements at the crest and the bottom are very close, whereas the maximum horizontal displacement occurs in the midheight region.

Figure 5.16 shows the vertical displacement field. The displacement increases gradually along the height, and reaches the maximum value of 55 mm at the dam crest. The values of the β along the bottom boundary are significantly reduced due to deformeability of the foundation.

Parametric study of the foundation stiffness

Due to the lack of information on mechanical properties of the rock foundation, a parametric study is carried out to investigate the effect of the elastic module of the foundation. The results of the simulations indicate that the β field near the bottom boundary is significantly influenced by the stiffness of the foundation. Figure 5.18 shows the distribution of β for the elastic modulus of the foundation equal to 1.0 E_c. The values of β along the bottom boundary are below 1.0, indicating that only microcracking occurs. Furthermore, if the elastic modulus of the rock foundation is set to 0.5 E_c, the values of β are further reduced, as shown in Figure 5.19. It can be concluded that the degree of cracking near the dam bottom decreases with the decrease in the stiffness of the foundation.

The evolution of the β field due to AAR

The development of macro- and microcracks in the concrete dam can be identified by examining the evolution of the β field. The microcracks form initially at the exposed surface due to the differential expansion rate and a variety of environmental factors. Figure 5.20 shows the distribution of β after 5 years of continuing reaction. The values of β exceed 1 on the lower part of the exposed surfaces, indicating that not only microcracks

but also macrocracks have occurred in the concrete. After 10 years, the values of β along most of the exposed surfaces have exceeded 1 (Figure 5.21), indicating formation of macrocracks along these surfaces. After 25 years of continuing reaction, the macrocracks have developed further and the microcracks have penetrated into the inside of the dam, as shown in Figure 5.22. Most of the concrete mass within the dam experience $\beta > 0.9$, indicating a high probability of formation of microcracks.

Parametric study of the expansion rate

Expansion rate near the exposed surfaces of the dam is lower than that inside the dam, due to the lower relative humidity. There is no direct evidence, however, on the degree of the reduction. Therefore, a parametric study has been carried out to investigate the influence of different expansion rates of the concrete near exposed surfaces. The expansion rates were assumed to be 0%, 30% and 100% of the maximum expansion rate. Figure 5.23 shows that severe macrocracking occurs on the exposed surfaces when the expansion rate in this region is assumed to be zero. Results shown in Figure 5.24 indicate that when the expansion rate of exposed surfaces is 30% of its maximum value, the degree of macrocracking on the exposed surfaces is reduced. When the entire dam expands at uniform rate, the distribution of β becomes relatively uniform, and no macrocracks occurs on the exposed surfaces (Figure 5.25). Thus, it can be concluded that the degree of cracking on the exposed surfaces of the dam is highly influenced by the expansion rate of the concrete near the exposed boundaries. The lower the expansion rate of the concrete near the exposed surfaces, the higher the degree of damage on these surfaces.

5.3 Finite Element Modeling of Concrete Dam Accounting for the Seasonal Temperature Variation

5.3.1 Introduction

Seasonal temperature variation has been found to influence AAR in concrete dams. Both the AAR expansion rate and the degradation rate of material properties may vary with temperature change. Furthermore, seasonal temperature variation may act as a cycling load and cause thermal stresses in concrete dams. Thus, the stress paths experienced by the material are different from those in isothermal conditions.

The influence of temperature variation is taken into account in the simulations carried out in this section. To avoid the coupled thermo-mechanical analysis, a thermal analysis is performed first to obtain the temperature field for each time step. Then, the mechanical analysis is carried out to examine the mechanical response of the dam. The AAR expansion rates in the analysis are related to the temperature fields. The simulation results are discussed and compared to those of the isothermal condition.

5.3.2 Modeling of the Heat Transfer Phenomenon

The energy balance equation, involving the heat transfer, can be written as

$$\rho[\mathbf{c}]\frac{\partial T}{\partial t} - V^T[\mathbf{k}]VT = Q \tag{5.1}$$

where T is the temperature of the medium, $[\mathbf{c}]$ is the specific heat capacity matrix, ρ is the density, $[\mathbf{k}]$ is the thermal conductivity matrix, and Q is the applied flux. The boundary conditions are specified as

$$T = \tilde{T} \text{ on } \Gamma_T \tag{5.2}$$

$$\left(-[\mathbf{k}]\nabla T)^T \mathbf{n} = \tilde{q}\right) \text{ on } \Gamma_q \tag{5.3}$$

where $\tilde{q}$ is the surface intensity of heat flow including the externally supplied flux, the convective heat transfer at the surface and the radioactive heat transfer at the surface. The convective boundary is generally defined by Newton's law as

$$\tilde{q}_c = h_c\left(T - T_a\right) \tag{5.4}$$

where h_c is the convective coefficient, and T_a is the ambient temperature. The Stefan-Bolzmann law governs the radiation, which can be written as

$$\tilde{q}_r = eC_s\left(T^4 - T_a^4\right) \tag{5.5}$$

with e being the emissivity of the surface and C_s being the Stefan-Bolzmann constant. In this problem, the heat loss by radiation is not expected to be significant within the range of temperature difference between the air and the concrete. Therefore, Equation 5.5 can be simplified into a quasi-linear form

$$\tilde{q}_r = h_r\left(T - T_a\right) \tag{5.6}$$

where h_r is defined as

$$h_r = eC_s\left(T^2 + T_a^2\right)\left(T + T_a\right) \tag{5.7}$$

A constant value of h_r can be adopted for a relatively narrow range of variation in temperature.

By using finite element discretization, the following finite element approximation is obtained

$$[\mathbf{C}]\dot{\mathbf{T}} + \left([\mathbf{K}] + [\mathbf{K}_c]\right)\mathbf{T} = \mathbf{f} \tag{5.8}$$

In this equation, $[\mathbf{C}]$ is the heat capacity matrix

$$[\mathbf{C}] = \int_\Omega \mathbf{N}^T \rho c \mathbf{N} d\Omega \tag{5.9}$$

$[\mathbf{K}]$ is the thermal conductivity matrix

$$[\mathbf{K}] = \int_\Omega (\nabla \mathbf{N})^T k(\nabla \mathbf{N}) d\Omega \tag{5.10}$$

$[\mathbf{K}_c]$ is the thermal convection matrix

$$[\mathbf{K}_c] = \int_{\Gamma_q} \mathbf{N}^T (h_c + h_r)\mathbf{N} d\Gamma \tag{5.11}$$

and

$$\mathbf{f} = \int_\Omega \mathbf{N}^T \overline{Q} d\Omega + \int_{\Gamma_q} \mathbf{N}^T \tilde{q}_e d\Gamma + \int_{\Gamma_q} \mathbf{N}^T (h_c + h_r)T_a d\Gamma \tag{5.12}$$

Dam-air interface

The air temperature is simulated as

$$T(t) = A \sin \frac{2\pi(t+\zeta)}{P} + T_m \tag{5.13}$$

where $A = \dfrac{T_{max} + T_{min}}{2}$ represents the mean value of the average monthly temperatures in

°C; t denotes the time in days; ζ is the lag factor in days; P is the period of the sine

function, (365 days); and $T_m = \dfrac{T_{max} - T_{min}}{2}$.

The distribution of average daily and monthly air temperatures, according to the

temperature record in Manicougan, Quebec, Canada, is shown in Figure 5.26 (Leger *et*

al., 1993). The minimum average daily air temperature is -14.93°C, which occurs in

January, while the maximum average daily air temperature is 18.13°C, occurring in July.

To simplify the formulation, ζ is assumed to be $\dfrac{1}{4}P$, corresponding the lowest

temperature occurring on January 1. Thus, the evolution of the air temperature is

$$T(t) = 16.53 \sin 2\pi \left(\frac{t}{365} - \frac{1}{4} \right) + 1.6 \tag{5.14}$$

Dam-reservoir interface

The reservoir temperature varies with depth and follows a cyclic seasonal variations. The

temperature profile used for the reservoir is shown in Figure 5.27. The maximum surface

temperature is assumed to occur at $\dfrac{1}{2}P$. The ice period is assumed to be approximately

from $\dfrac{3}{4}P$ to next year's $\dfrac{1}{4}P$. During this period, no temperature fluctuation occurs

because the ice insulates the reservoir. Thus, the water temperature is assumed to remain

constant. During the ice-free period, temperature fluctuation takes place on the water

surface. This causes the water temperature to fluctuate in time. In this period, the time

fluctuation is assumed to follow a sine curve defined as

$$
T(t) = \begin{cases} T_{min}, & i \leq t \leq 365\left(\dfrac{1}{4}+i\right), \\ (T_{max} - T_{min})\sin 2\pi\left(\dfrac{t}{365}-\dfrac{1}{4}\right)+T_{min}, & 365\left(\dfrac{1}{4}+i\right) < t < 365\left(\dfrac{3}{4}+i\right), \\ T_{min}, & 365\left(\dfrac{3}{4}+i\right) \leq t \leq 365(1+i), \end{cases}
$$

$$i = 0,1,2,\ldots \qquad (5.15)$$

where i denotes seasonal cycle, in years.

The maximum and minimum average monthly temperatures, T_{max} and T_{min}, vary with the

reservoir depth d. On the water surface, they are 14 °C and 0 °C, respectively. At 15 m

depth, they become 6 °C and 2 °C, respectively. From 60 m depth, both T_{max} and T_{min}

become 4 °C and remain constant. The corresponding expressions are

$$
T_{min} = \begin{cases} 2\dfrac{d}{15}, & 0 \leq d \leq 15\text{m} \\ 2 + 2\dfrac{d-15}{45}, & 15 < d \leq 60\text{m} \end{cases} \qquad (5.16)
$$

$$T_{max} = \begin{cases} 14 - 8\dfrac{d}{15}, & 0 \le d \le 15\text{m} \\ 6 - 2\dfrac{d-15}{45}, & 15 < d \le 60\text{m} \end{cases}$$

(5.17)

Ground surface boundary

The temperature of the ground surface is assumed to follow a sine curve from $\dfrac{1}{4}P$ to

$\dfrac{3}{4}P$ with the maximum temperature being 19.4 °C. During the remaining period, the

temperature remains at -1.2 °C, due to snow insulating the ground and preventing heat

transfer between the air and the ground during cold months. Therefore, the temperature

on the ground surface (Figure 5.28) can be expressed as

$$T(t) = \begin{cases} -1.2, & i \le t \le 365\left(\dfrac{1}{4}+i\right), \\ 20.6\sin\dfrac{2\pi(t - 365/4)}{365} - 1.2, & 365\left(\dfrac{1}{4}+i\right) < t < 365\left(\dfrac{3}{4}+i\right), \quad i = 0,1,2,\dots \\ -1.2, & 365\left(\dfrac{3}{4}+i\right) \le t \le 365(1+i), \end{cases}$$

(5.18)

Foundation bottom and side boundaries

Generally, the penetration depth of annual temperature oscillations beneath the ground

surface is about 10 m. Therefore, the temperature at the base of the foundation does not

vary with time. Based on the interpolation of the available data, the temperature along the

bottom boundary of the foundation is 6.0°C. The bottom boundary of the dam is assumed to be an adiabatic boundary.

5.3.3 Finite Element Modeling

To investigate the mechanical behavior of the dam under seasonal temperature variations, two dam models were analyzed. Model 1 is the dam founded on the ground surface. The dam bottom retains an adiabatic boundary condition for thermal analysis (Figure 5.29) and fixed boundary conditions for mechanical analysis. Model 2 is a dam-foundation system, whose boundary conditions for thermal analysis are shown in Figure 5.30. The boundary conditions for mechanical analysis of the two models are the same as those described in Section 5.2.2. In the finite element analysis, the thermal analysis is carried out first to obtain the temperature fields for each time step. Because the seasonal temperature variation is a periodic function, the length of time history to be computed extends to 1 year. Based on the temperature field, which in turn affects the expansion rate of concrete and degradation rate of material properties, the mechanical response of the structure due to AAR is then simulated.

5.3.4 Results and Discussion

The Temperature Fields

Figures 5.31 and 5.32 show the temperature fields in winter for Models 1 and 2, respectively. The temperature for most part of the dam is below 0 °C, indicating that AAR expansion is very low in winter. The distribution of the temperature, especially in the

lower part of the dam, is affected by different boundary conditions. However, since the temperature is very low in winter, the influence of this difference on the AAR expansion rate is very limited. Figures 5.33 and 5.34 show the temperature fields in spring/fall for models 1 and 2, respectively. The temperature ranges between -1.2 °C and 2.2 °C in the dam, indicating that the AAR expansion rate is low in these seasons as well. Further, the temperature near the bottom boundary of the dam in model 1 is higher than that in model 2 due to the effect of different boundary conditions. This implies that the AAR expansion rate near the dam bottom in model 1 may be slightly higher than that in model 2. In summer, the distributions of temperature for model 1 and 2 are very similar, as shown in Figures 5.35 and 5.36, respectively. The temperature on the exposed surfaces reaches approximately 19 °C, which enables AAR expansion to develop rapidly; whereas the parts of the structure near the reservoir side remain at lower temperature, 5.8 °C. Due to the high average temperature, which favors AAR development, the temperature distribution in summer will dominate the mechanical response of the dam.

The results for the dam with fixed bottom boundary

Figures 5.37 and 5.38 show the horizontal and vertical displacement fields for model 1 after 25 years of continuing reaction. The AAR expansion near the exposed surfaces is higher than that on the reservoir side, which is consistent with the summer temperature distribution. The maximum horizontal displacement at the dam crest reaches 37 mm, which is higher than that corresponding to the isothermal condition. The vertical displacement is zero along the dam bottom boundary and increases gradually with height.

The maximum vertical displacement, which is 57 mm, is the same as that under the isothermal conditions.

The distribution of the stress intensity β corresponding to 25 years of AAR is shown in Figure 5.39. In general, this distribution is substantially different from that corresponding to the isothermal condition. The values of β are relatively high near the exposed surfaces and lower near the dam-reservoir interface. On the exposed surfaces, the macrocracking is more severe than that in the isothermal model.

The results of the dam-foundation system

The horizontal displacement field after 25 years of AAR is shown in Figure 5.40. In the lower part of the dam, the horizontal displacement increases from the center to both sides. In the upper part of the dam, the displacement is towards the reservoir side with maximum value of 38 mm at the crest of the dam. The lateral displacement at the bottom edge of the reservoir side of the dam is approximately 40 % of the horizontal displacement at the crest of the dam. The vertical displacement field is shown in Figure 5.41. The displacement increases gradually along the height, with a maximum value of 58 mm at the dam crest. The deformed mesh shape for Model 2 is shown in Figure 5.42. The bottom of the dam is uplifted due to the expansion of the concrete dam.

The distribution of the stress intensity β is shown in Figure 5.43. Again, the β field is substantially different from that corresponding to the isothermal conditions. In general, the values of β on the exposed surfaces of the dam are higher prompting enhanced cracking in the concrete.

Comparison of the displacement fields

Figure 5.44 compares the displacement fields of models 1 and 2. The displacements in the upper part of the dam are very similar for the two models. In the lower part of dam, the deformation is highly affected by the boundary conditions. In model 1, the fixed-bottom boundary constrains the concrete expansion, and significantly affects the deformation of the dam.

Figure 5.45 compares the displacement fields of the dam-foundation system under isothermal and non-isothermal conditions. In the former case, the concrete expands continuously at a constant rate. When the variation of seasonal temperature is considered, the reservoir side of the dam expands less due to the lower temperature. On the air side, the expansion develops more rapidly due to high temperatures in summer.

Final remarks

The horizontal displacement at the crest of the dam as predicted by the non-isothermal model is close to the field measurements (Figure 5.2). The vertical displacements both under the isothermal and non-isothermal conditions are slightly higher than the measured values. The main reason for this discrepancy is the plane-strain approximation, in which the displacements in the longitudinal direction are constrained. According to the actual measurements (Gocevsky, 1993), the concrete strain in the longitudinal direction is not zero.

5.4 Finite Element Modeling of The Water Intake Structure

5.4.1 Description of the Model

The Beauharnois Powerhouse contains 37 water intakes, which are concrete gravity-type structures founded on Potsdam sandstone. The geometry of the water intake structure analyzed in this study is shown in Figure 5.46. The upstream side of the structure is the reservoir. On the downstream side, the intake structure is connected with the powerhouse. The intake structure is sheltered from weathering by the intake superstructure, i.e., a single-framed steel structure building with roof trusses, composite steel-concrete columns and simple steel columns on the upstream and downstream sides.

Relative humidity

In order to account for the variation of the relative humidity in concrete, the structure is divided into three zones, as shown in Figure 5.47. In zone 1, i.e., the lower part, the relative humidity is assumed to be higher than 85%. In zone 2, it is assumed that the relative humidity is lower than 85% so that the expansion is lower than in zone 1. Two cases are studied, that is, 0% and 30% of the maximum expansion rate. The relative humidity in zone 3 is assumed to be low, so that the AAR expansion can be neglected.

Properties of concrete

The material properties of the concrete are E_c = 15,000 MPa, v = 0.2, f_c = 27 MPa, and f_t = 0.1 f_c. Based on the available information, A_2 was identified as 6.329x10-7 /day, which corresponds to a principal strain rate of 0.000077 /year for free expansion. The remaining parameters were chosen as A_1 = 0.1; A_3 = 51.95; A_4 = 17.32. The value of A_3 and A_4

correspond to 30 % reduction in elastic module and 10 % reduction in compressive/tensile strength after 25 years of continuing reaction (Kladek *et al.*, 1995).

Reinforcement

The reinforcement in the water intake is accounted for by introducing reinforced layers, with equivalent thickness of 0.002 m. The Young's modulus is taken as E = 210,000 MPa. In finite element analysis, the reinforcement layers are meshed with three-dimensional shell elements.

Finite element discritization and boundary conditions

The intake structure was meshed with 1832 3D 8-node hexahedron elements as shown in Figure 5.48. The reinforcement was modeled with 796 3D 4-node shell elements (Figure 5.49). The total number of elements is 2579, and the total number of nodal point is 2731.

To simplify the computational effort, the water intake structure is assumed to be founded on a rigid foundation with a fixed-bottom boundary. Thus, the interaction of the structure and the foundation is ignored. In the longitudinal direction (x-direction) of the water intake, both sides of the structure are connected with adjacent units. Therefore, the structure is assumed to be fixed in the longitudinal direction. This assumption is based on the observation of the throat ring ovalness as shown in Figure 5.50, which indicates that the deformation in the longitudinal direction was constrained by the adjacent structures. The upstream face of the water intake is a free boundary. The downstream face is connected to the powerhouse structure with a construction joint, which has reportedly

closed due to concrete expansion. Therefore, the boundary of the downstream face was assumed to be fixed in the normal direction (z-direction).

Solution Scheme

The analysis was carried out in two stages. The first stage was to obtain the solution due to self-weight of the structure and the hydrostatic pressure exerted by water. The second stage of the analysis was the simulation of the effect of 25 years of continuing AAR. The modified Newton-Raphson scheme was used in the finite element analysis.

5.4.2 Results and Discussion

The displacement field

The vertical displacement field after 25 years of AAR is shown in Figure 5.51. The vertical displacement increases gradually from the bottom to the top of the intake structure. The maximum vertical displacement is 58 mm. Little variation in vertical displacement takes place in the x-direction. Figure 5.52 shows the horizontal displacement field in the upstream-downstream direction (z-direction). Due to the imposed kinematic constraint, the displacement in the z-direction is zero along the downstream face of the water intake, and increases gradually towards the upstream face of the structure. This indicates that the structure expands towards the upstream side in the z-direction. The maximum horizontal displacement in the z-direction is 42 mm, and takes place at the top of the water face of the structure. The horizontal displacement at the top of the structure is very close to the corresponding measured values. However, the vertical displacement at the measurement location is approximately 30% higher than the corresponding measured values. One of the

reasons is that the slot cutting carried out previously may have reduced the deformation of the structure.

The distribution of β

Due to the uncertainty pertaining to the expansion rate in zone 2, a parametric study was carried out. The AAR expansion rate of the concrete in zone 2 was assumed to be 0% and 30%, and the corresponding results are shown in Figures 5.53 and 5.54, respectively. For the AAR expansion rate in zone 2 of 30%, the maximum β value is approximately 0.97, indicating severe microcracking. When this expansion rate is reduced to zero, the maximum β value is increased to 1.07, indicating the occurrence of macrocracks. In general, high β values occur at concave and bulkly sections.
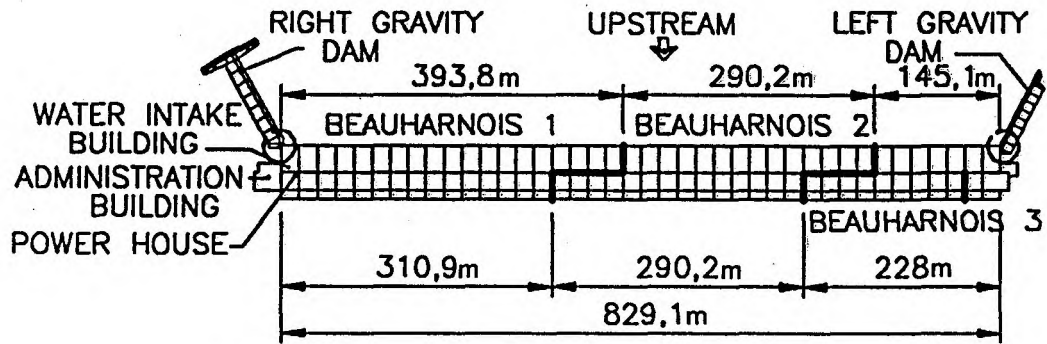
Figure 5.1   Geometry of the Beauharnois powerhouse.

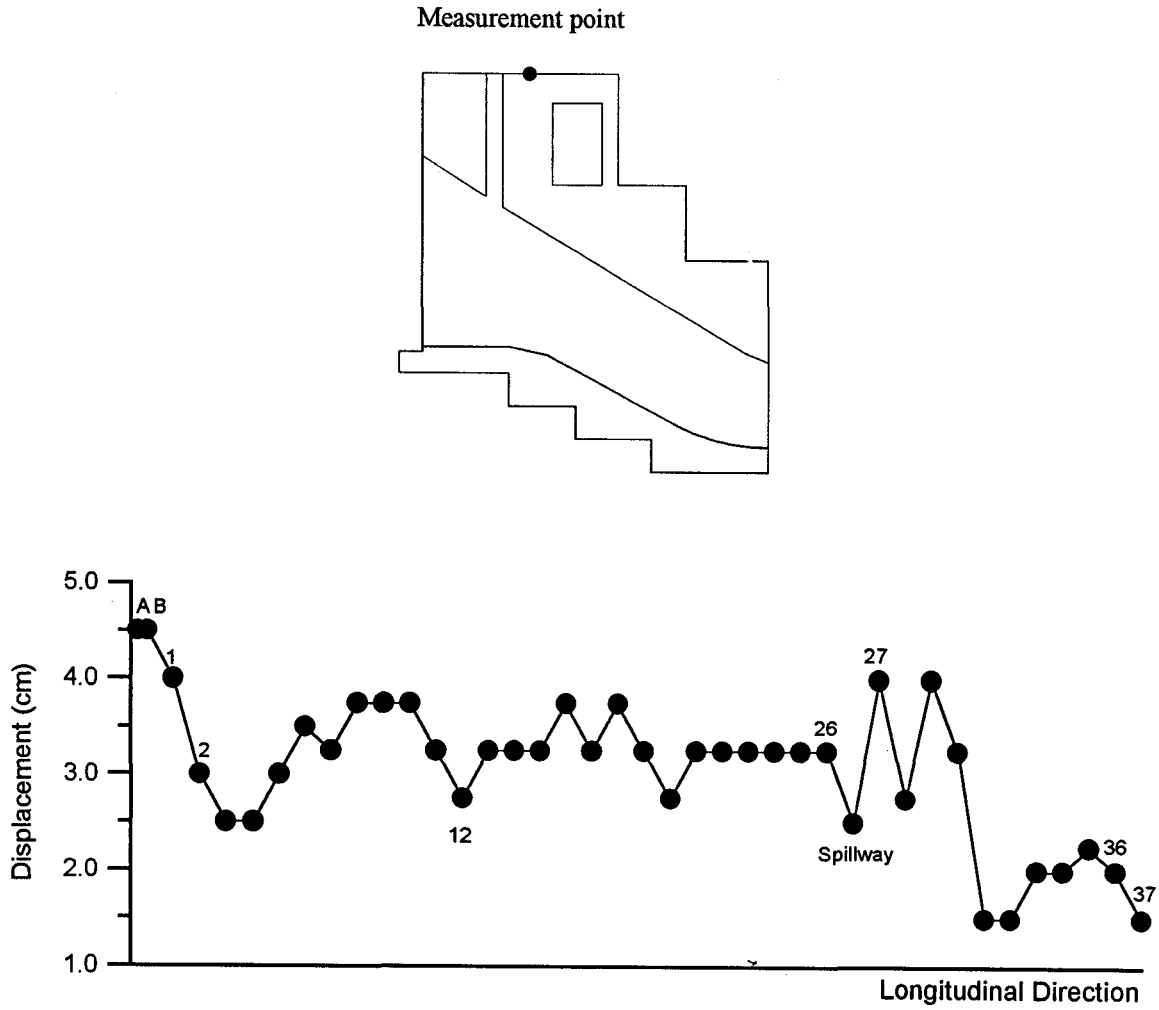Figure 5.2 Measured horizontal displacement (in the upstream-downstream direction) of the south wing dam.

Upstream side
measurement point

Downstream side
measurement point

Figure 5.3 Measured vertical displacements of the south wing dam.
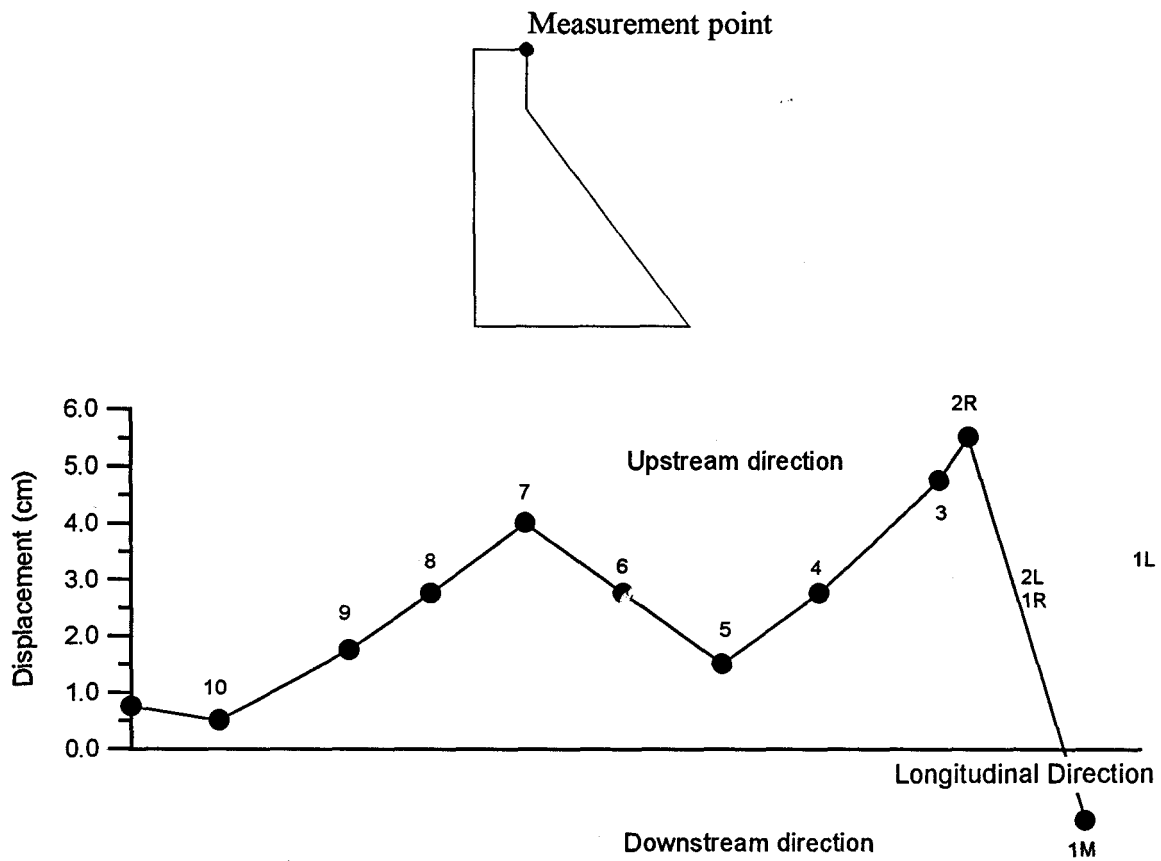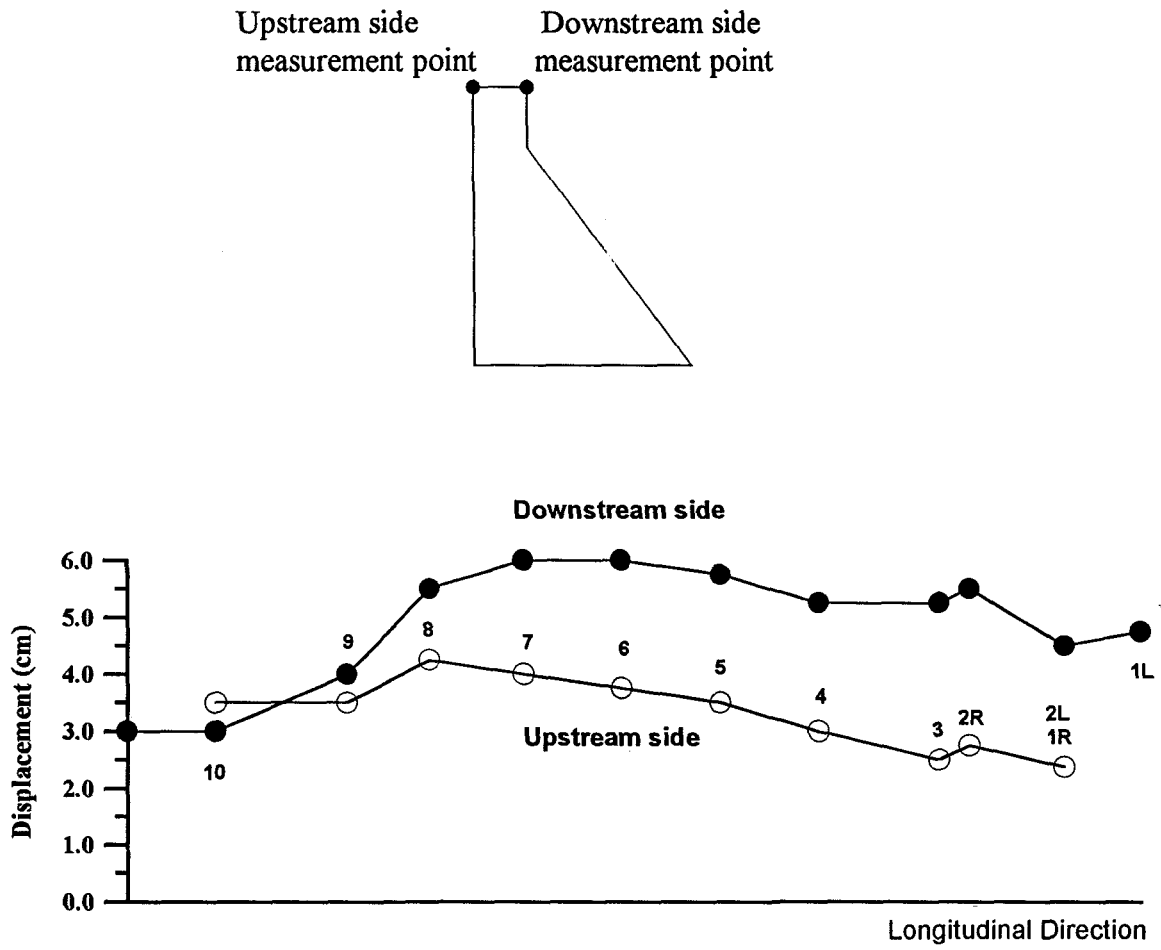
1, 2, ..., 10 are dam block numbers.

Measurement point
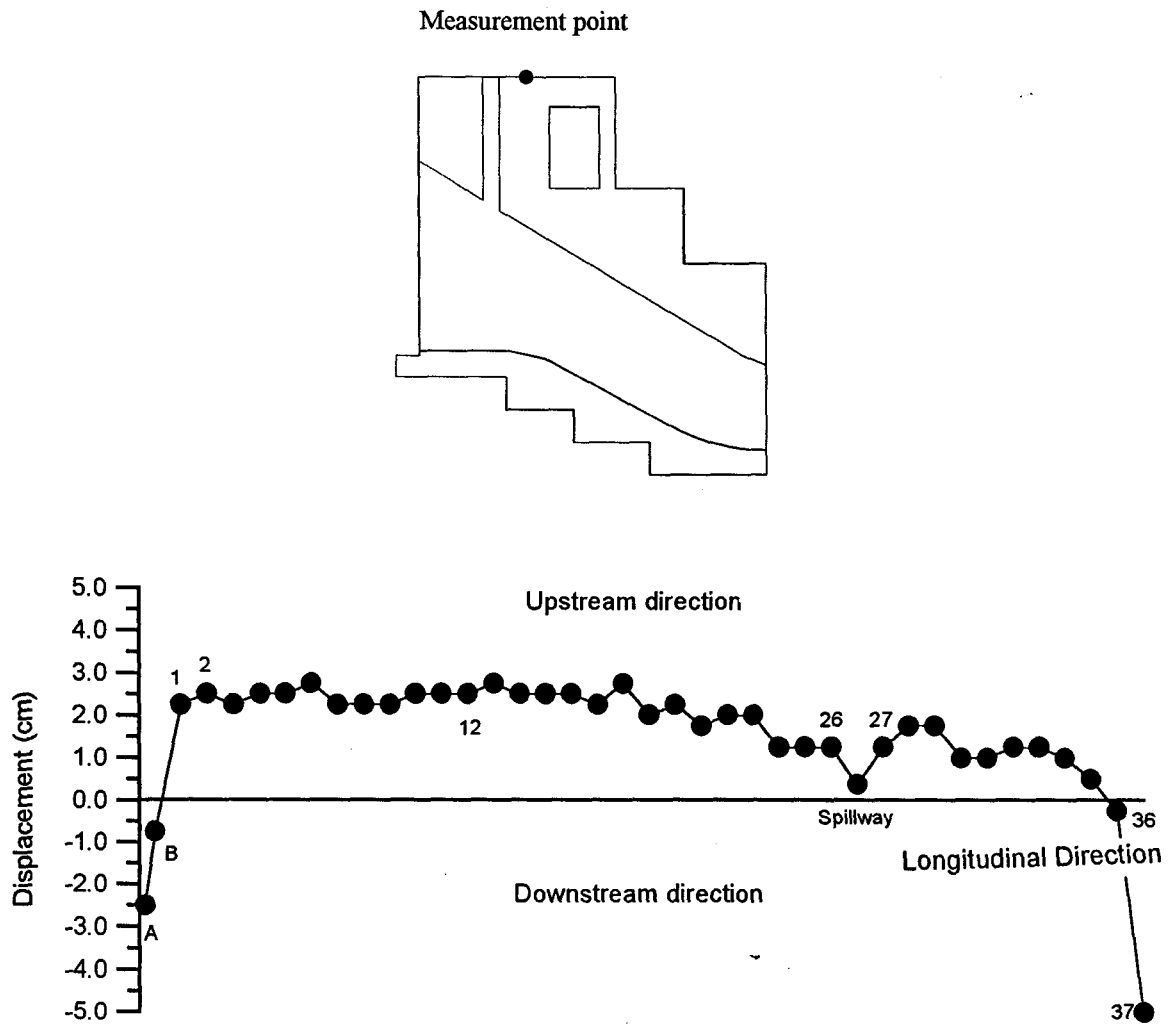
A, B, 1, 2, ..., 37 are intake unit numbers.

Figure 5.4 Measured horizontal displacement of the intake structures in the upstream-downstream direction.

Figure 5.5 Measured vertical displacement of the intake structures.

118
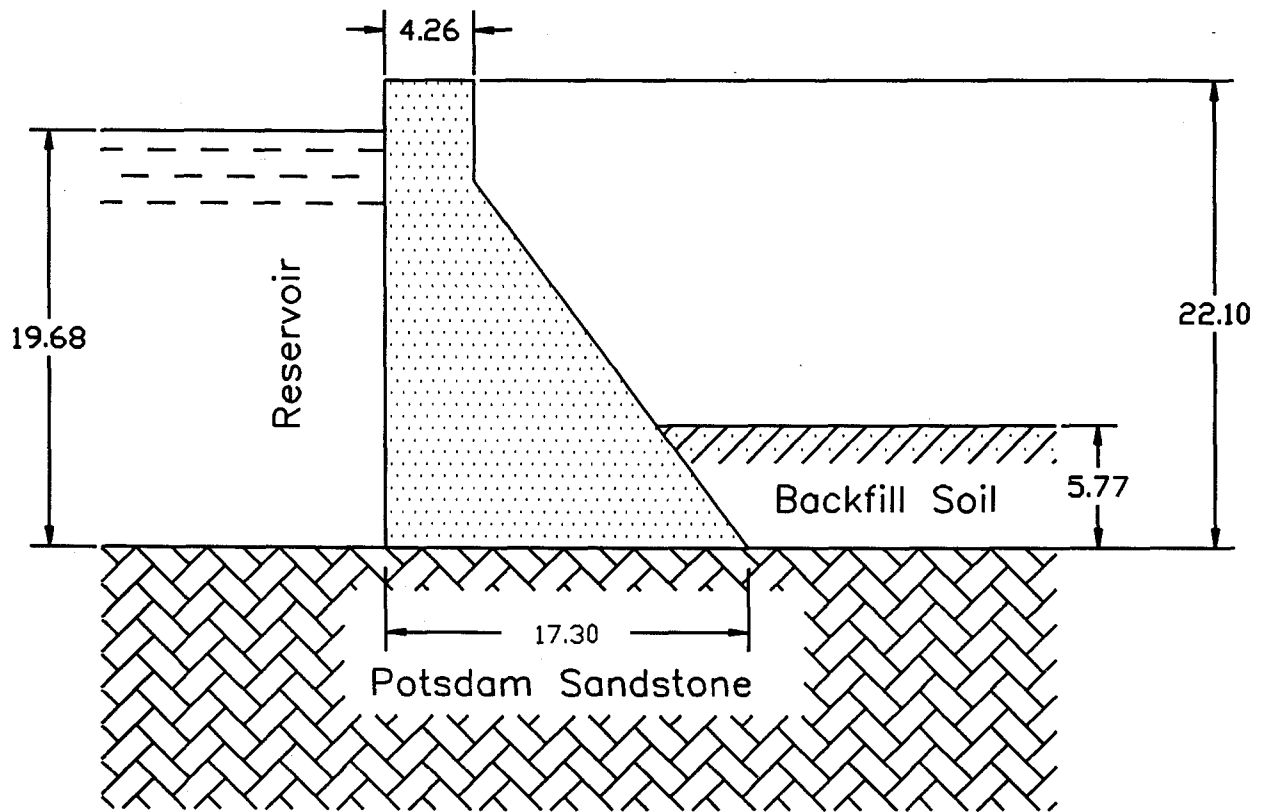
Figure 5.6   Typical cross-section of the south wing dam.
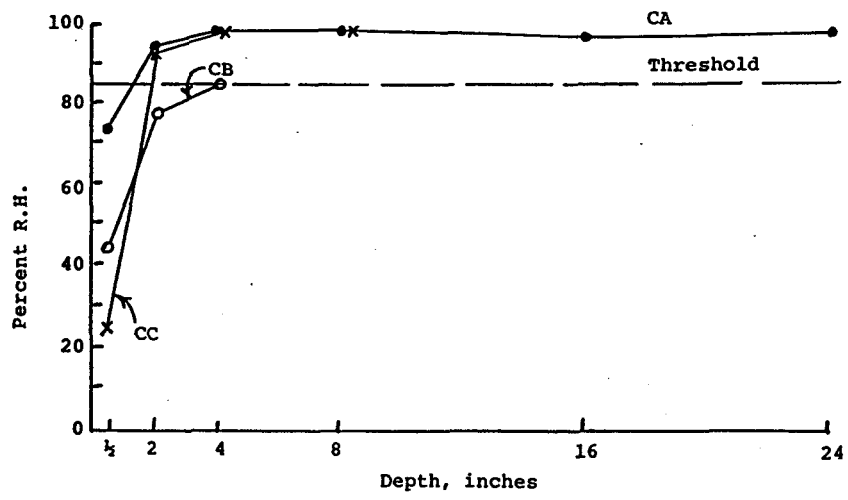
Figure 5.7   The measured relative humidity record for Coolidge Dam (Stark, 1985).
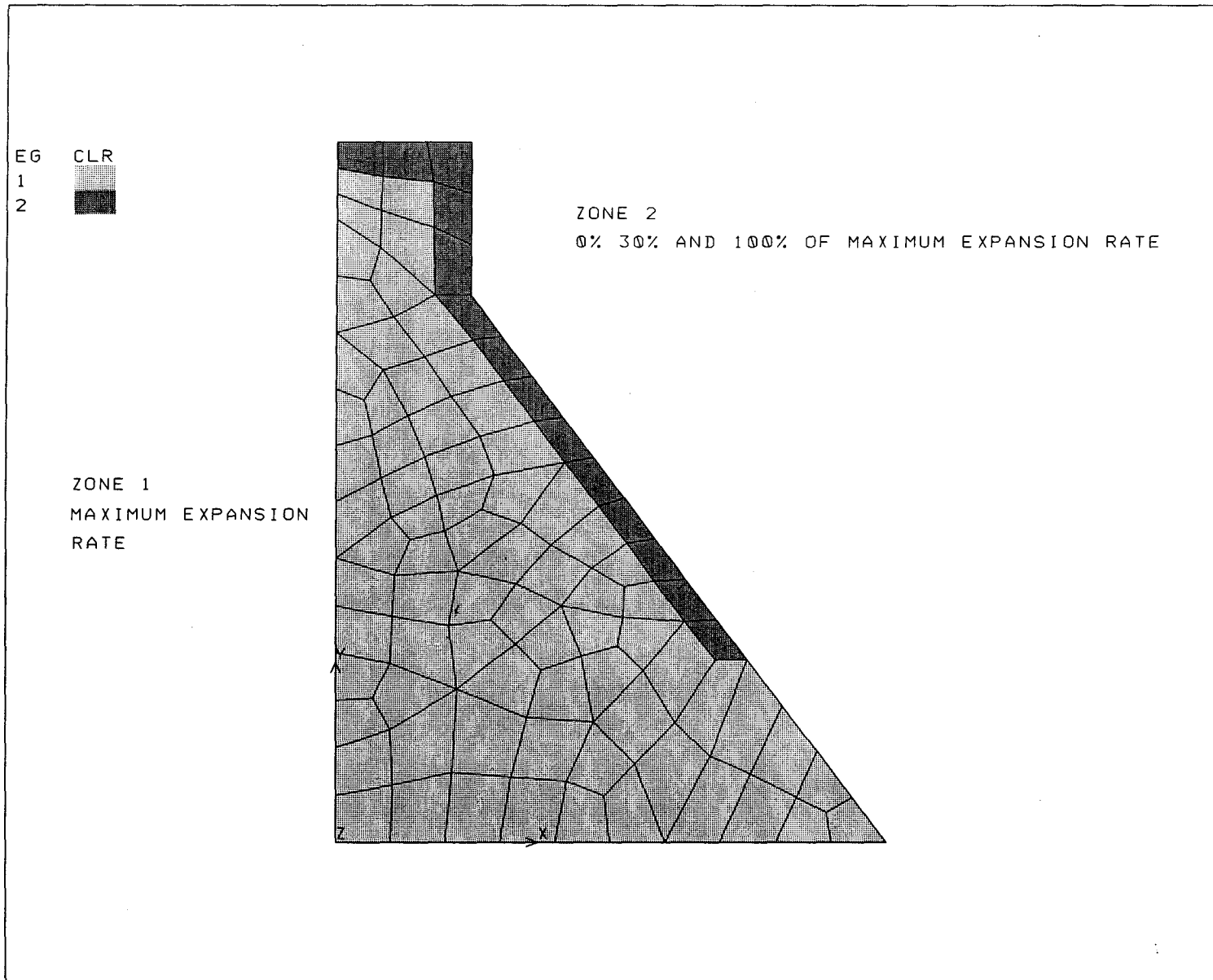
EG   CLR
1
2

ZONE 2
0% 30% AND 100% OF MAXIMUM EXPANSION RATE

ZONE 1
MAXIMUM EXPANSION
RATE

Figure 5.8   Expansion rate distribution according to the relative humidity in the dam.
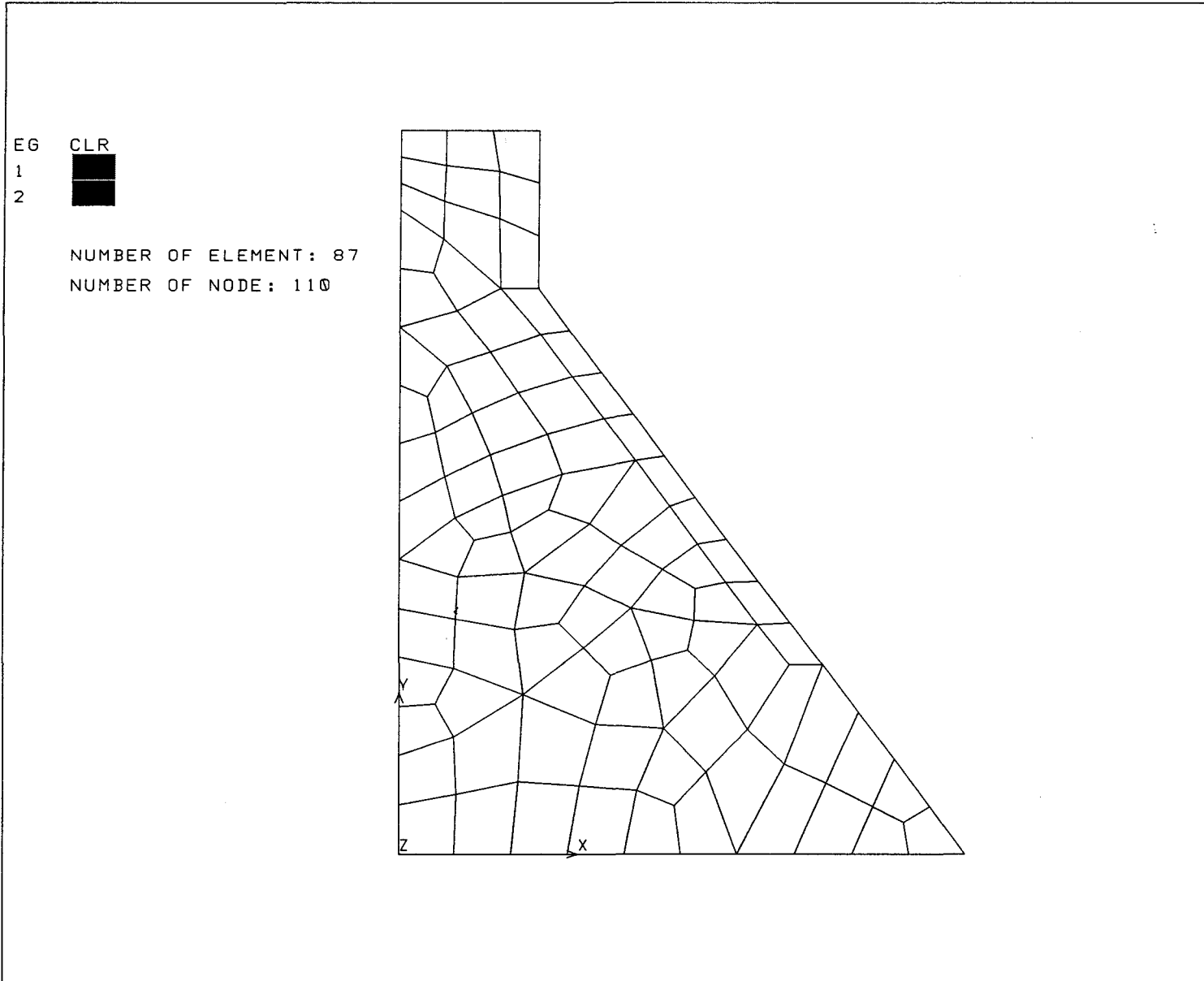
Figure 5.9   Two-dimensional finite element descritization of the south wing dam.
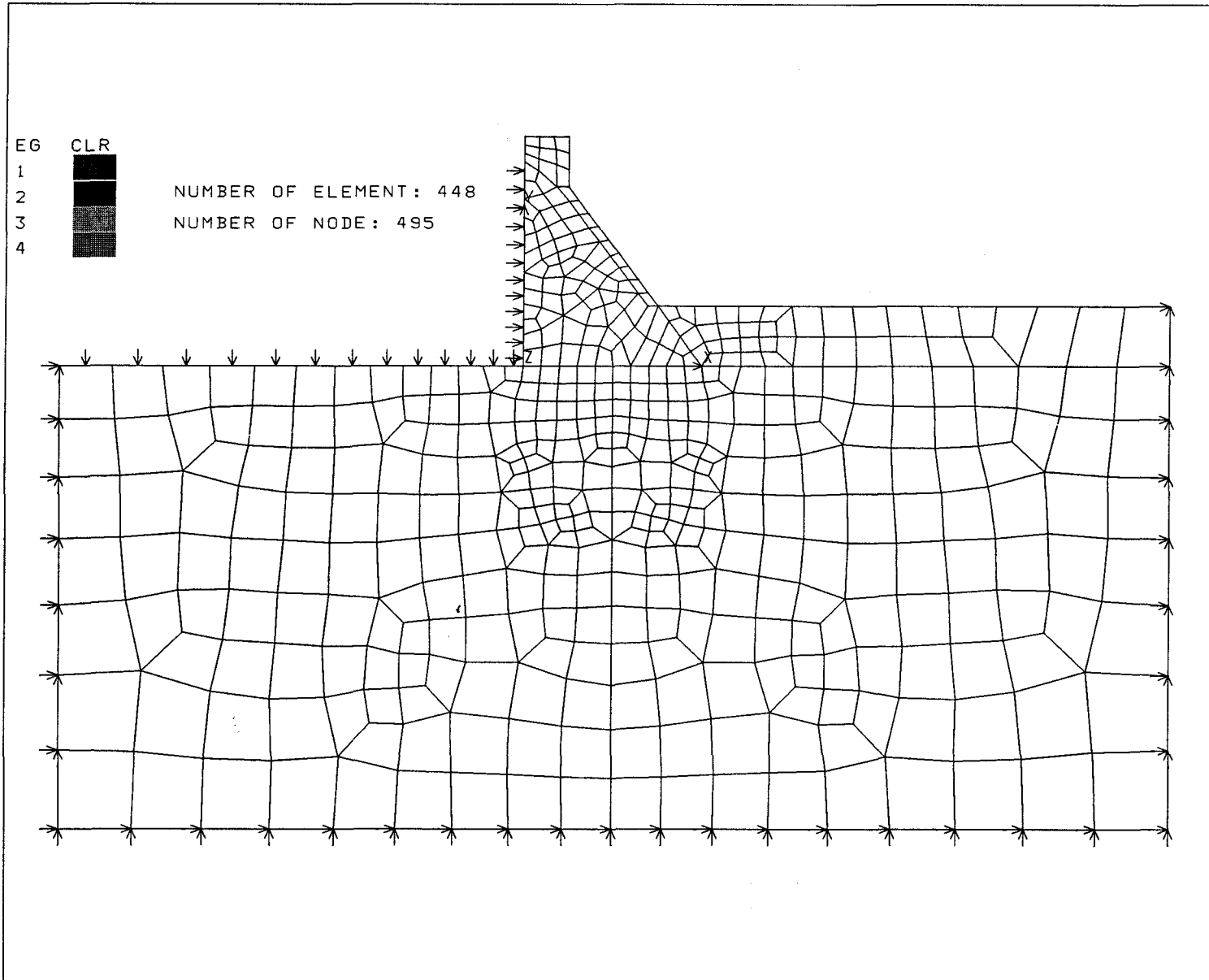
EG   CLR
1
2
3
4

NUMBER OF ELEMENT: 448

NUMBER OF NODE: 495

Figure 5.10   Two-dimensional finite element descritization of the dam-foundation system.

FIXED BOTTOM
EXPANSION=30%
TIME=25YEARS

```
0.009880
0.005940
0.002010
-0.00193
-0.00587
-0.00980
-0.01370
-0.01770
-0.02160
```
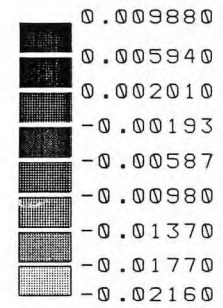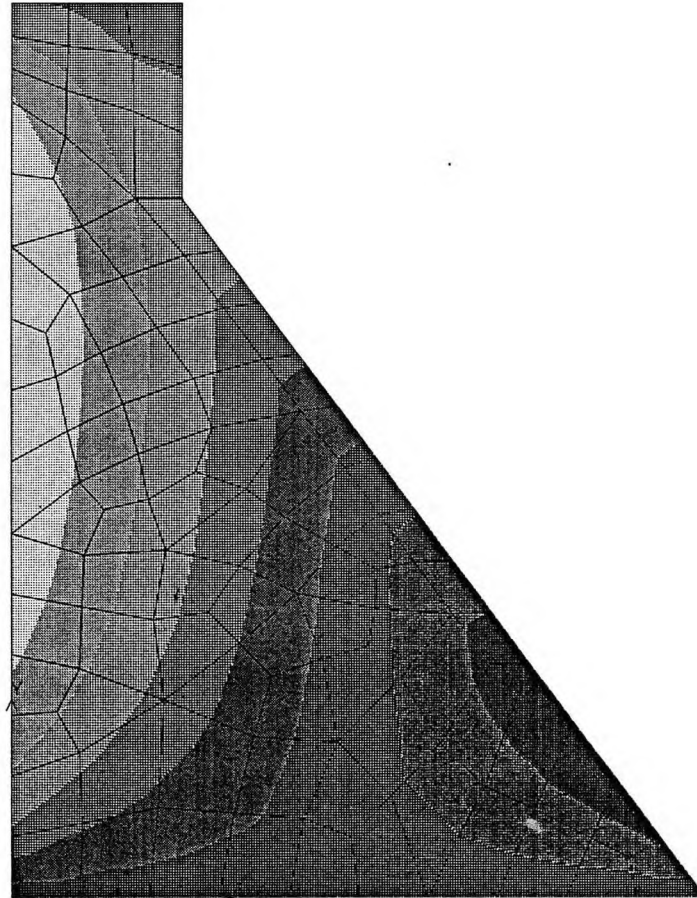
Figure 5.11 The horizontal displacement field in concrete dam with the fixed-bottom boundary.

FIXED BOTTOM
EXPANSION=30%
TIME=25YEARS

0.05470
0.04790
0.04100
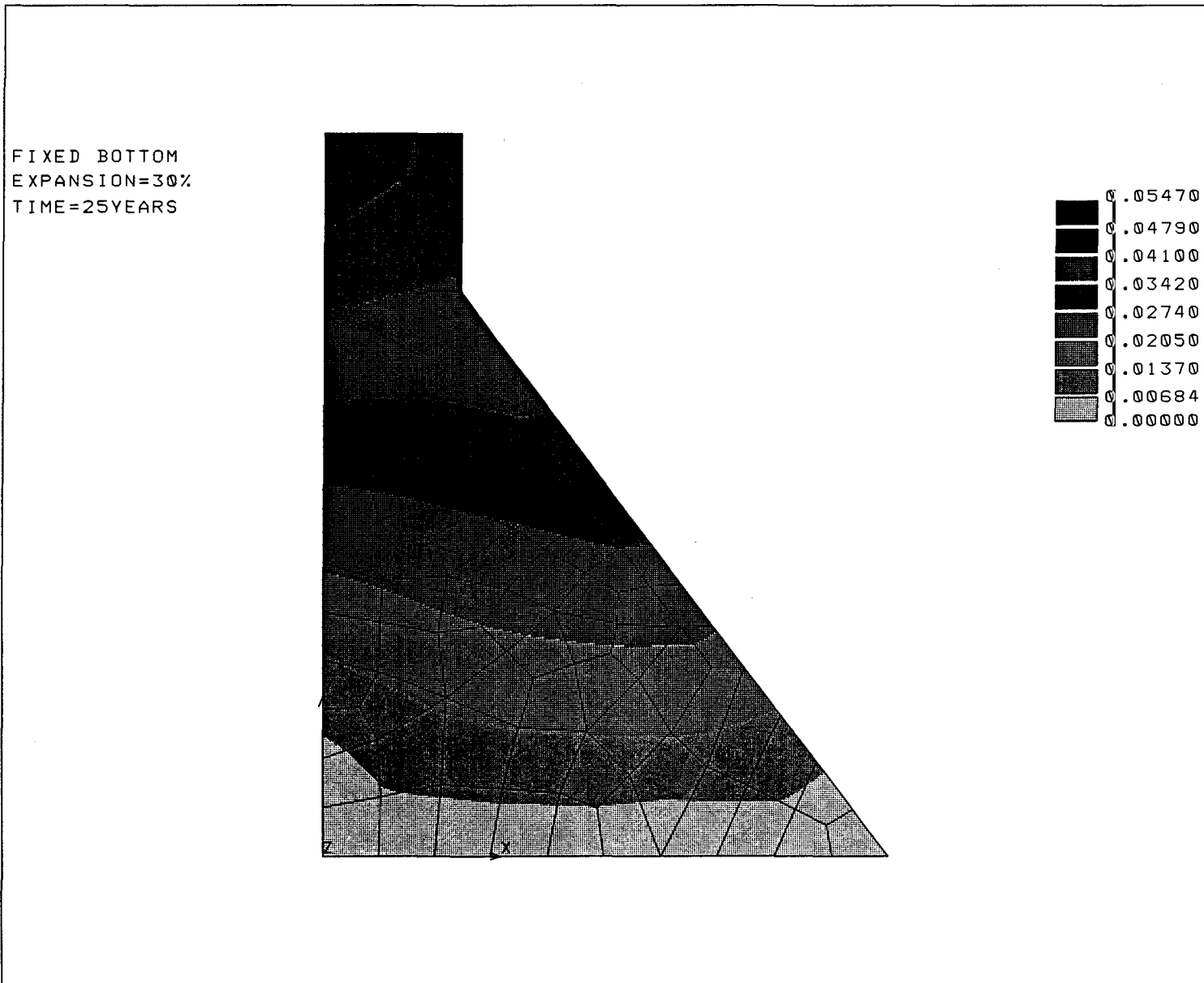0.03420
0.02740
0.02050
0.01370
0.00684
0.00000

Figure 5.12 The vertical displacement field in concrete dam with the fixed-bottom boundary.

FIXED BOTTOM
EXPANSION=30%
TIME=25YEARS

1.300
1.200
1.100
1.000
0.900
0.800
0.700
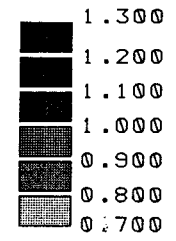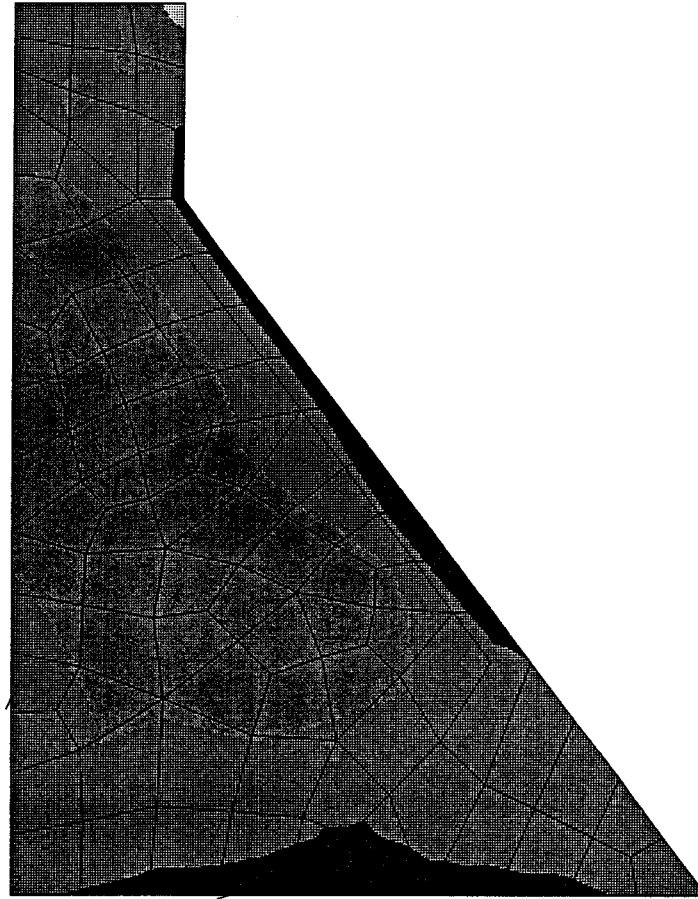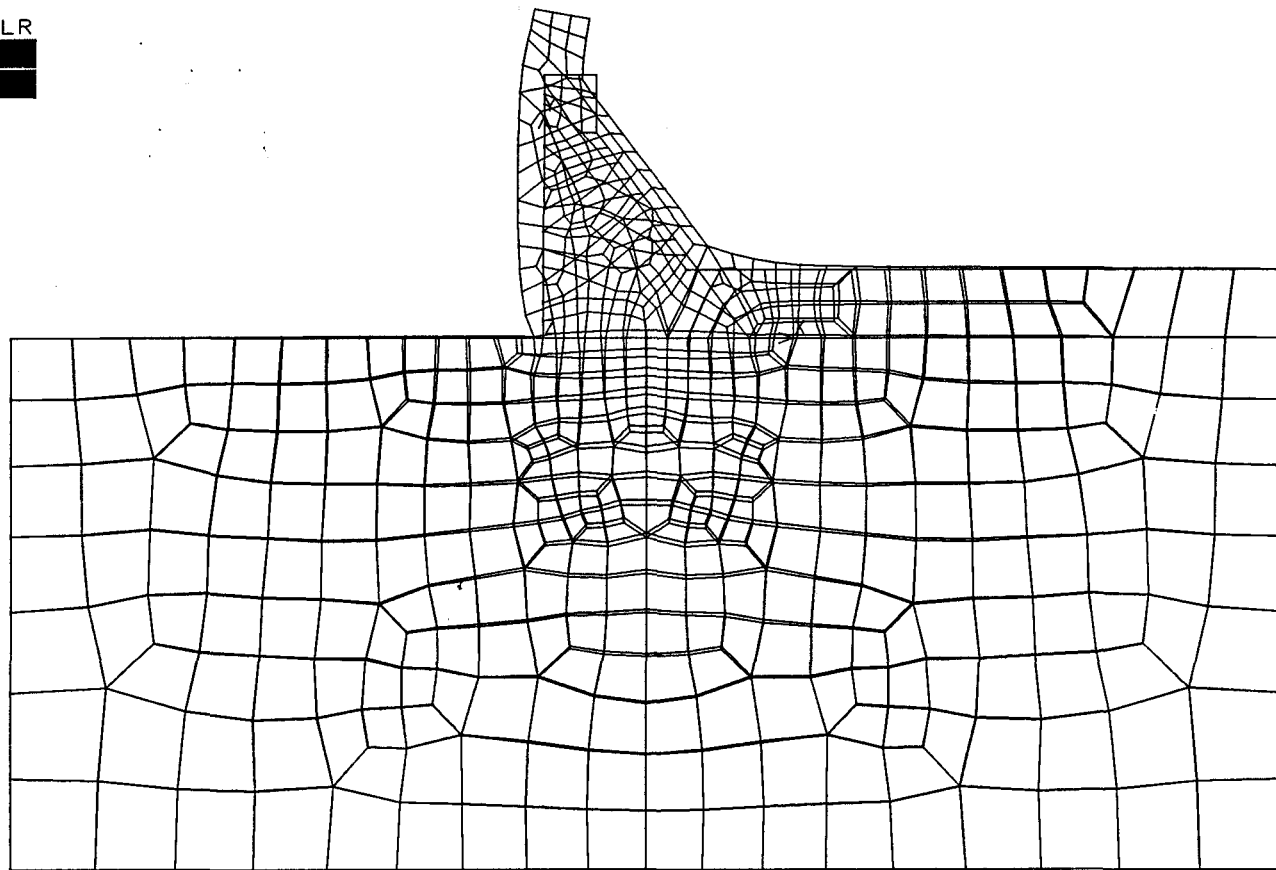
Figure 5.13   The distribution of β in concrete dam with the fixed-bottom boundary.

EG CLR
1
2

(a) The deformed mesh for the dam-foundation system.

Figure 5.14 The deformed mesh for dam-foundation system.

EG   CLR
1   ▮
2   ▮

FOUNDATION FILL
EXPANSION=30%
TIME=25YEARS

DEFORMED MESH (30TIMES)

(b) The deformed mesh for the dam.

127

FOUNDATION=0.5
EXPANSION=30%
TIME=25YEARS

0.009780
0.005700
0.001630
-0.00244
-0.00652
-0.01060
-0.01470
-0.01870
-0.02280
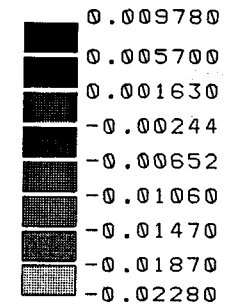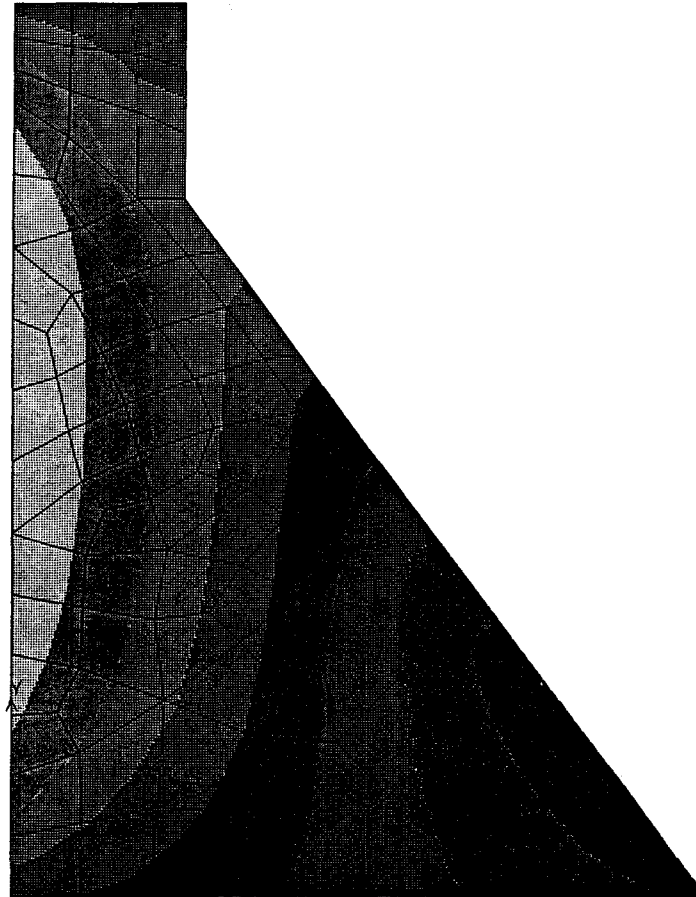
Figure 5.15 The horizontal displacement field for the dam-foundation system.

FOUNDATION=0.5
EXPANSION=30%
TIME=25YEARS

y

0.055200
0.048100
0.041000
0.033900
0.026800
0.019700
0.012600
0.005450
-0.00166

Z   X
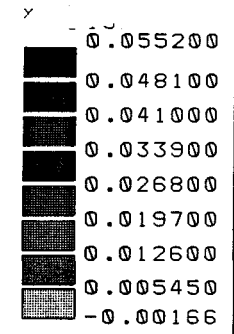
Figure 5.16   The vertical displacement field for the dam-foundation system.

FOUNDATION=1.5
EXPANSION=30%

1.300
1.200
1.100
1.000
0.900
0.800
0.700

Figure 5.17   The distribution of β for dam-foundation system ($E_R = 1.5\ E_C$).

F 1.0 E 30%

```
█  1.300
█  1.200
▓  1.100
▓  1.000
▓  0.900
░  0.800
░  0.700
```
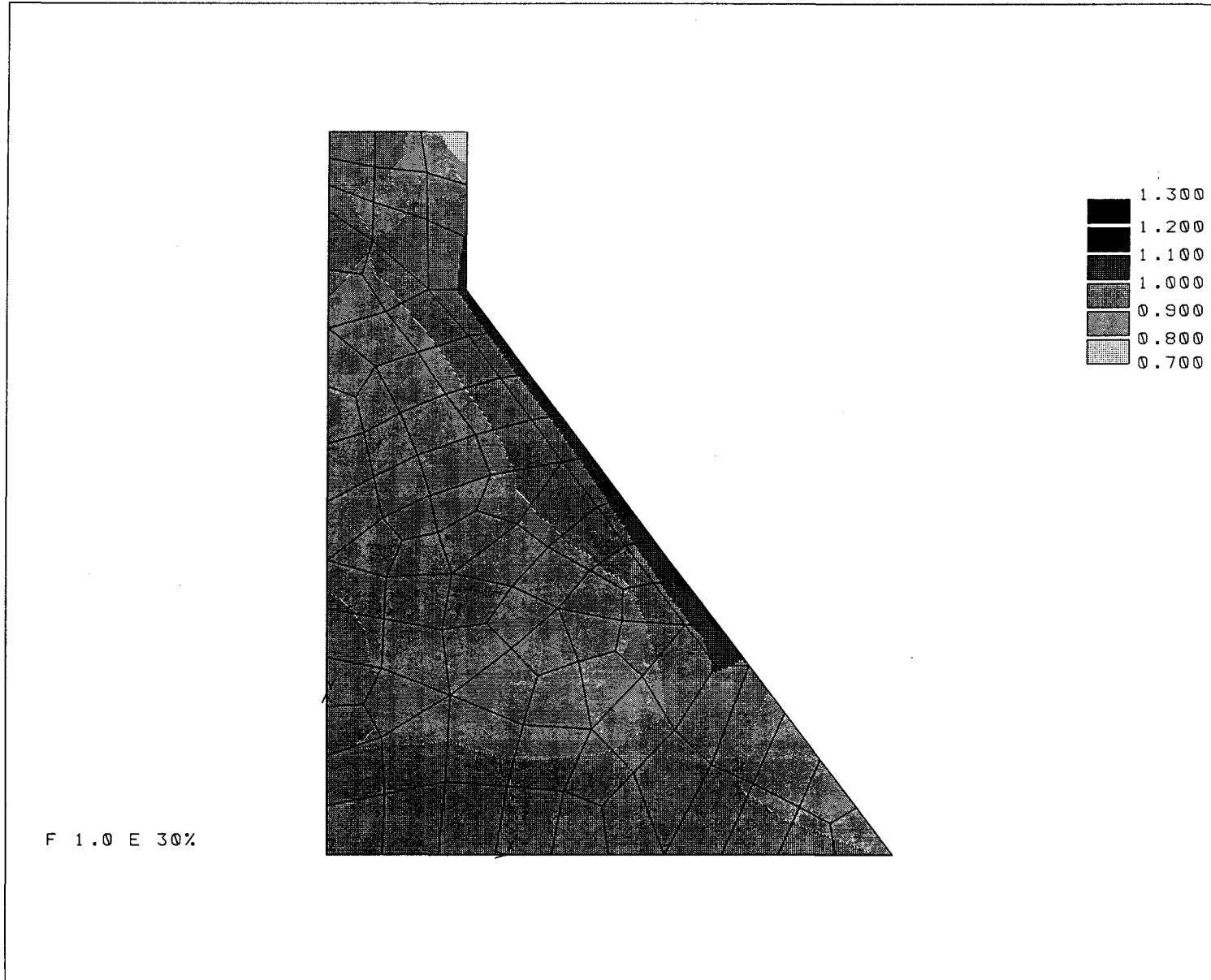
Figure 5.18   The distribution of β for dam-foundation system ($E_R = 1.0\ E_C$).
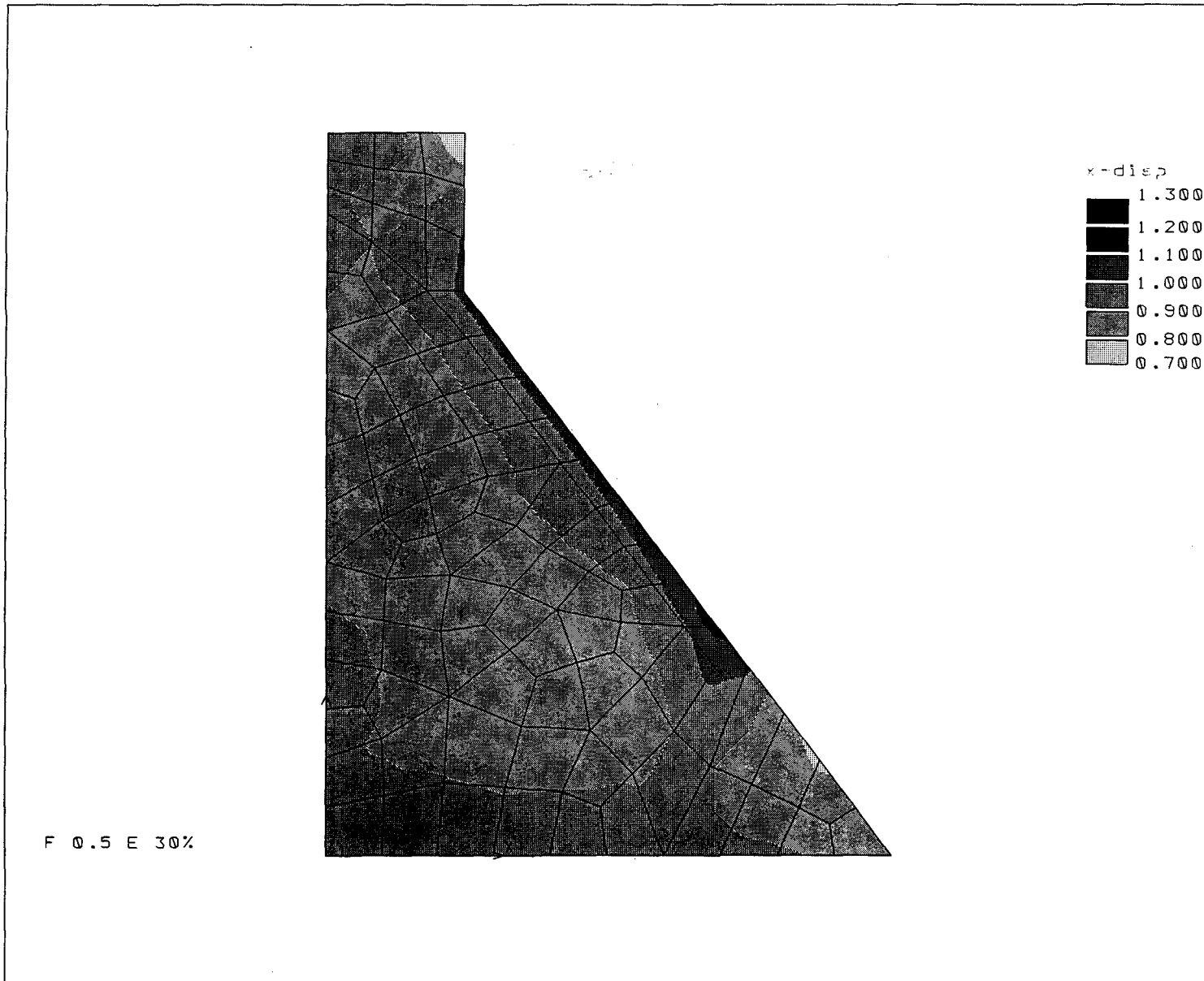
Figure 5.19 The distribution of β for dam-foundation system ($E_R = 0.5\ E_C$).

FOUNDATION=0.5
EXPANSION=1%
TIME=5YEARS

x-disp
1.300
1.200
1.100
1.000
0.900
0.800
0.700
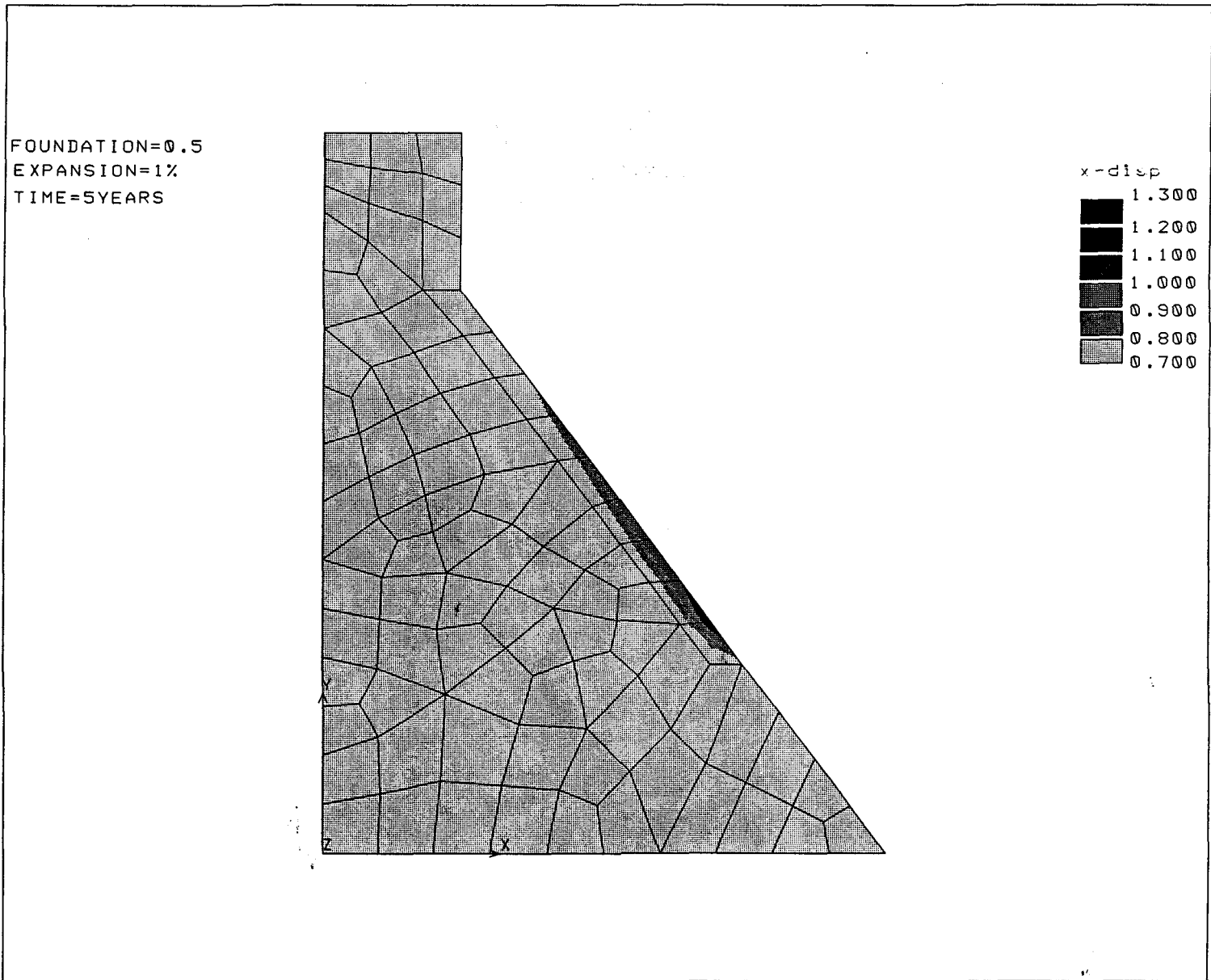
Figure 5.20 The distribution of β for dam-foundation system after 5 years of AAR.

FOUNDATION=0.5
EXPANSION=1%
TIME=10YEARS

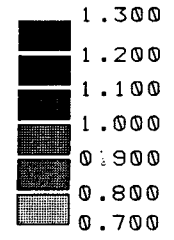x-disp
1.300
1.200
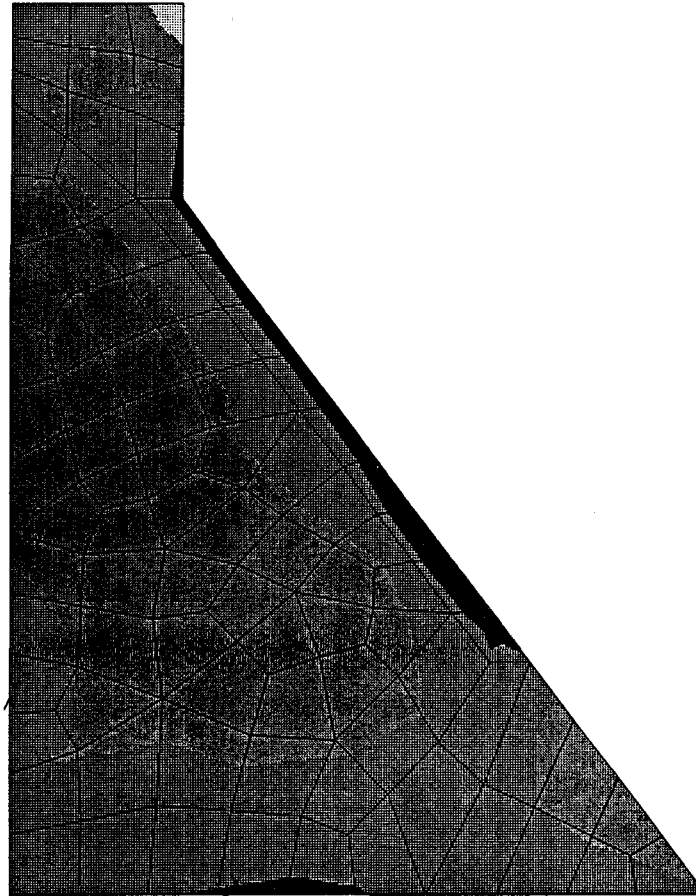1.100
1.000
0.900
0.800
0.700
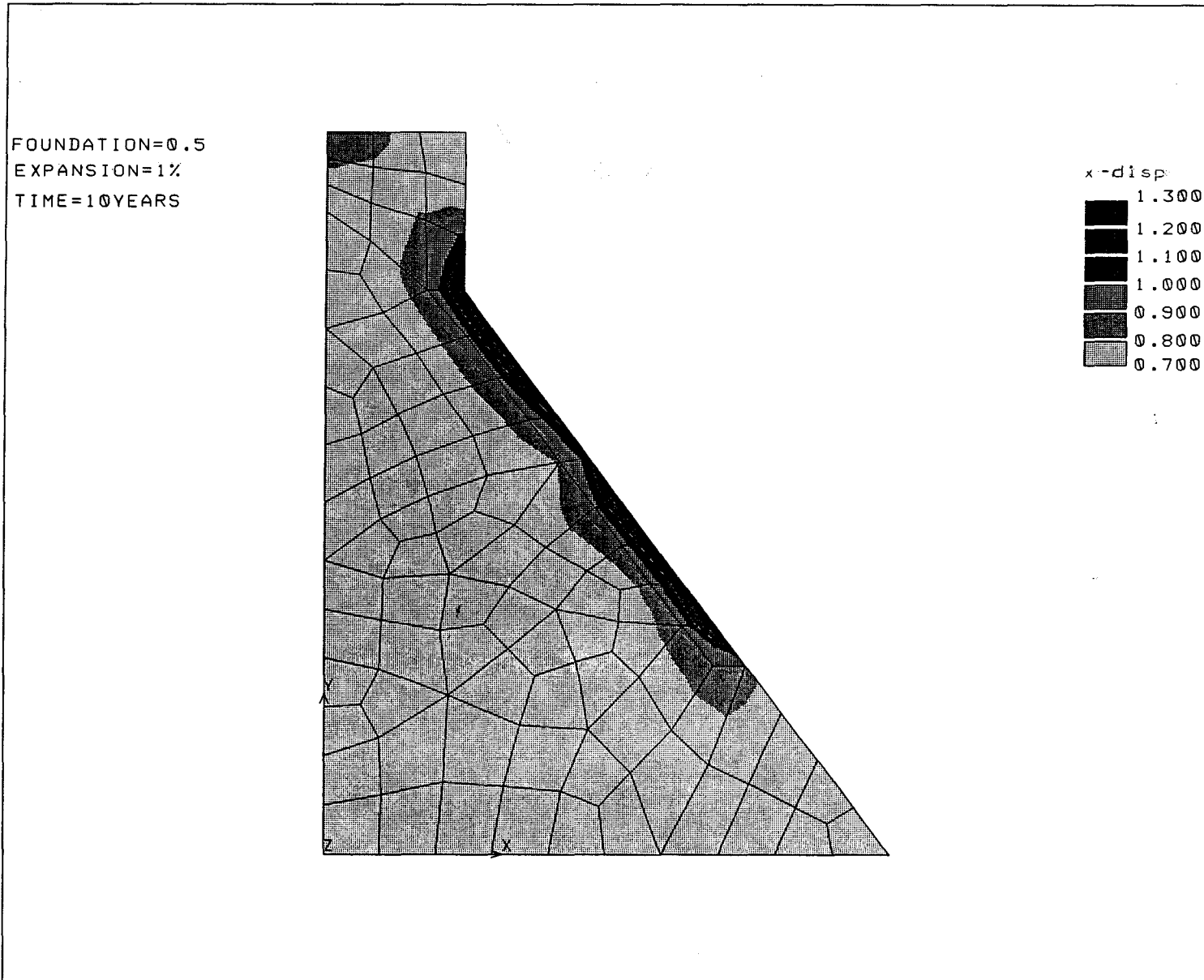
Figure 5.21   The distribution of β for dam-foundation system after 10 years of AAR.
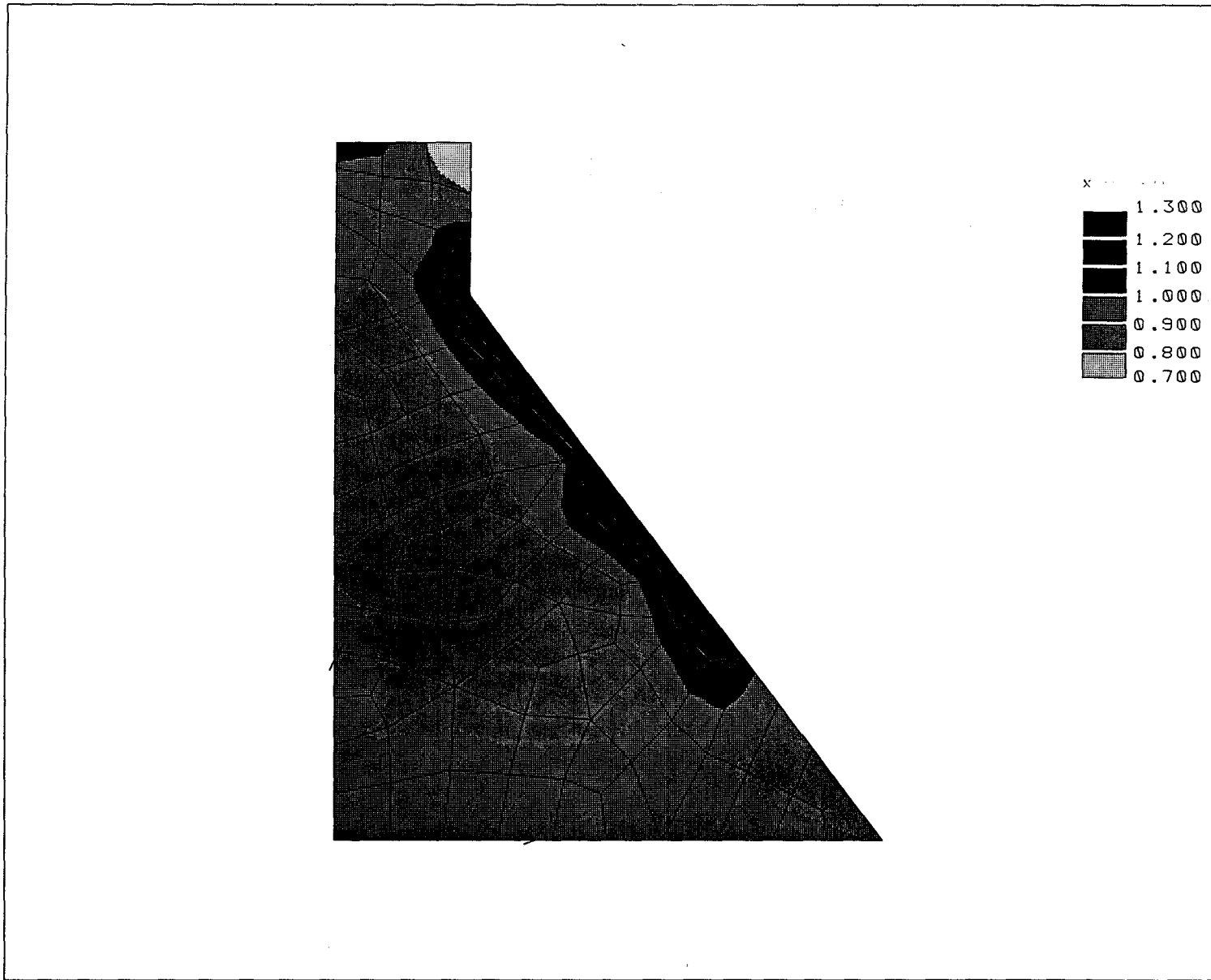
Figure 5.22 The distribution of β for dam-foundation system after 25 years of AAR.
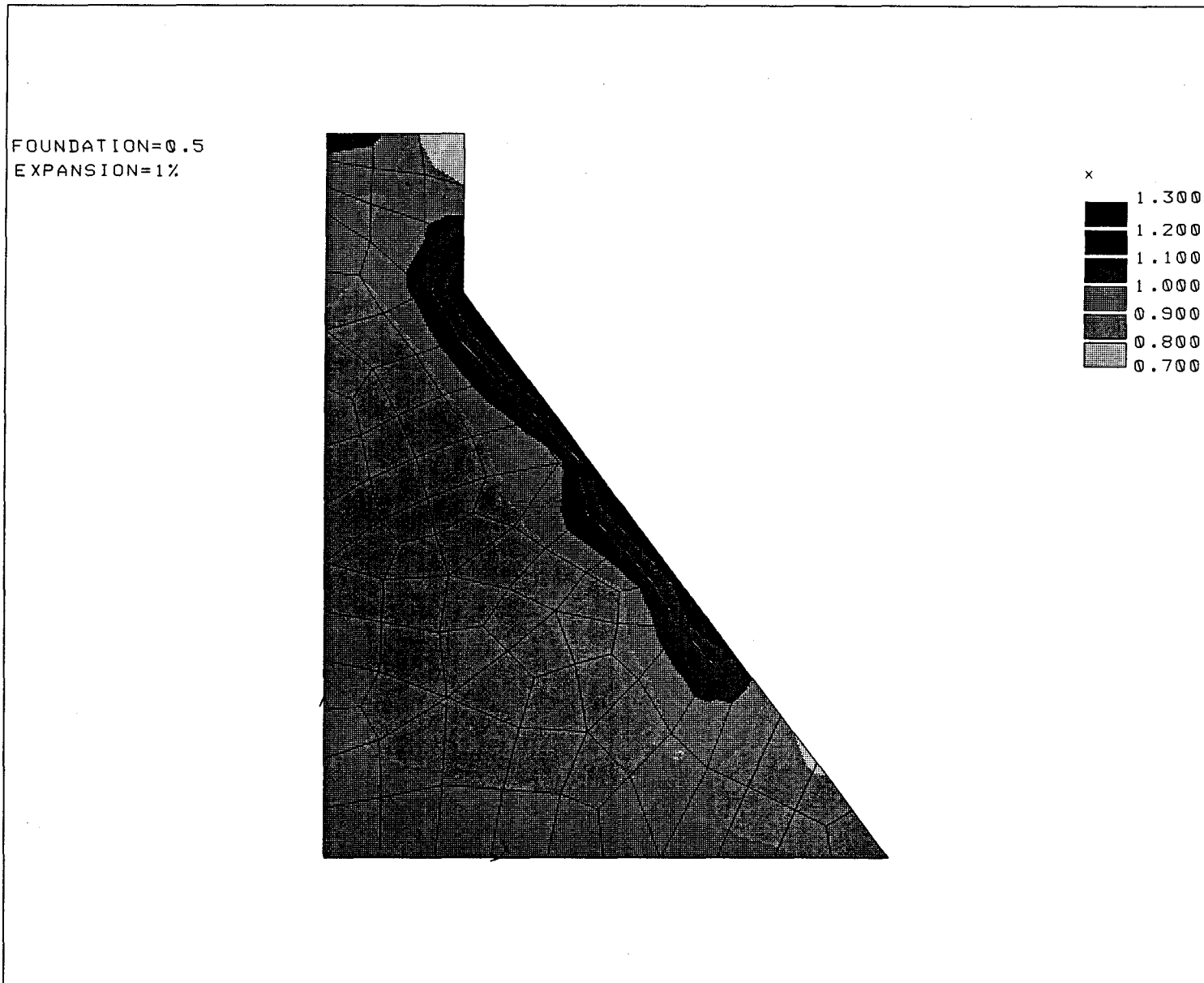
Figure 5.23 The distribution of β for dam-foundation system (0% expansion rate near the exposed surface).

FOUNDATION=0.5
EXPANSION=30%

1.300
1.200
1.100
1.000
0.900
0.800
0.700
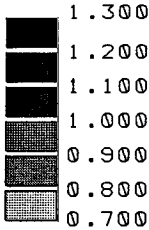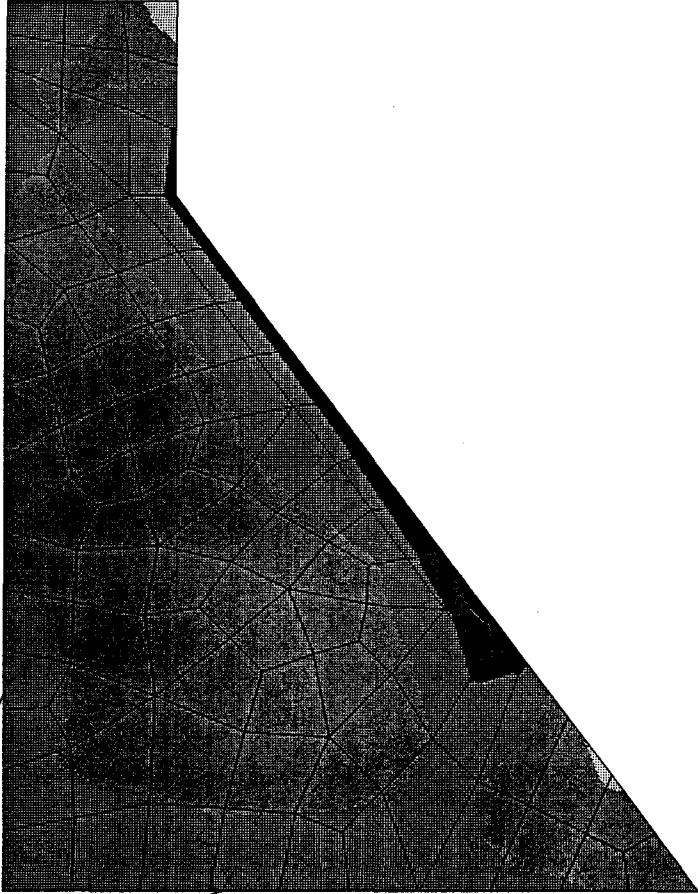
Figure 5.24 The distribution of β for dam-foundation system (30% expansion rate near the exposed surface).

FOUNDATION=0.5
EXPANSION=100%

1.300
1.200
1.100
1.000
0.900
0.800
0.700
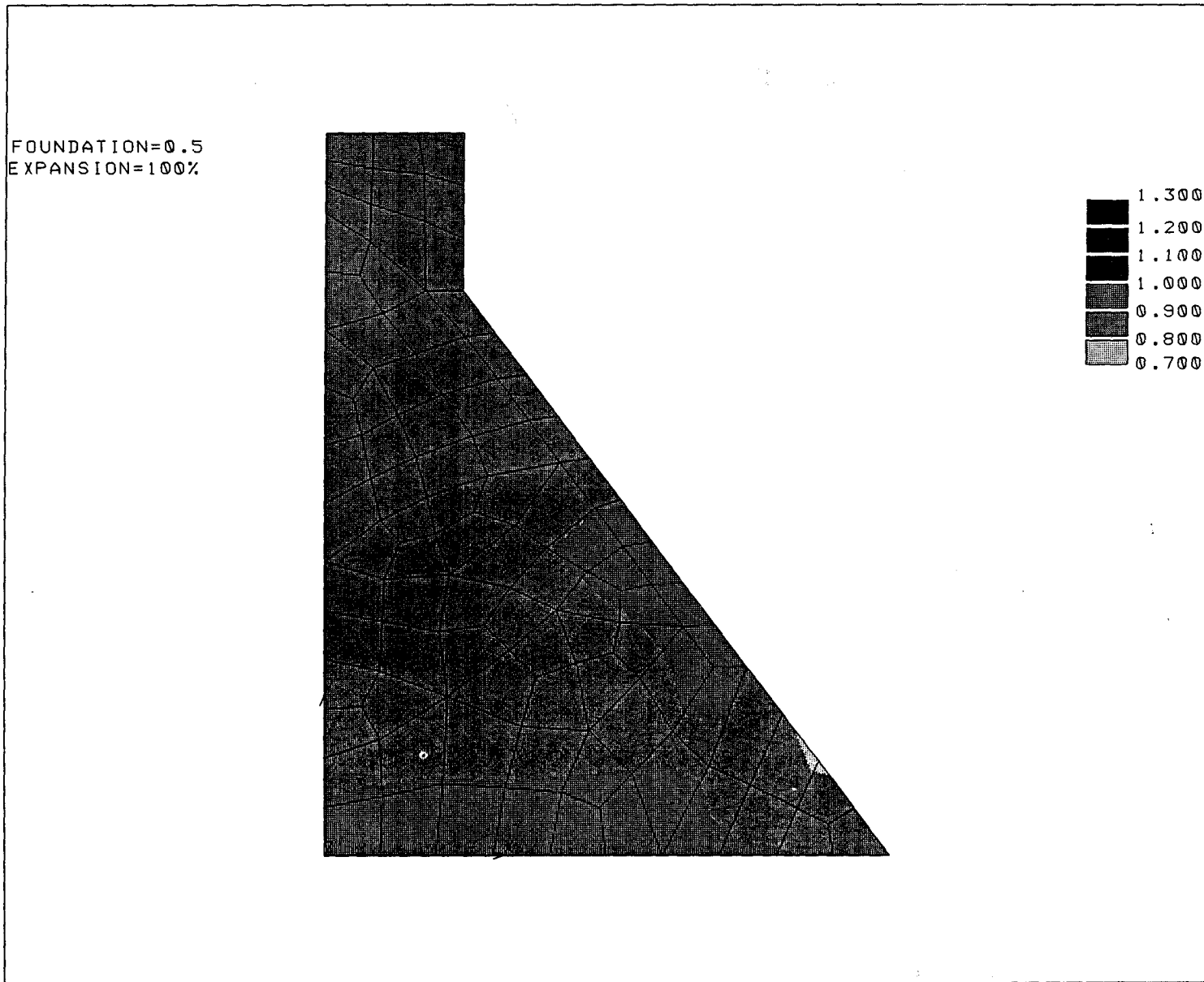
Figure 5.25 The distribution of β for dam-foundation system (100% expansion rate near the exposed surface).
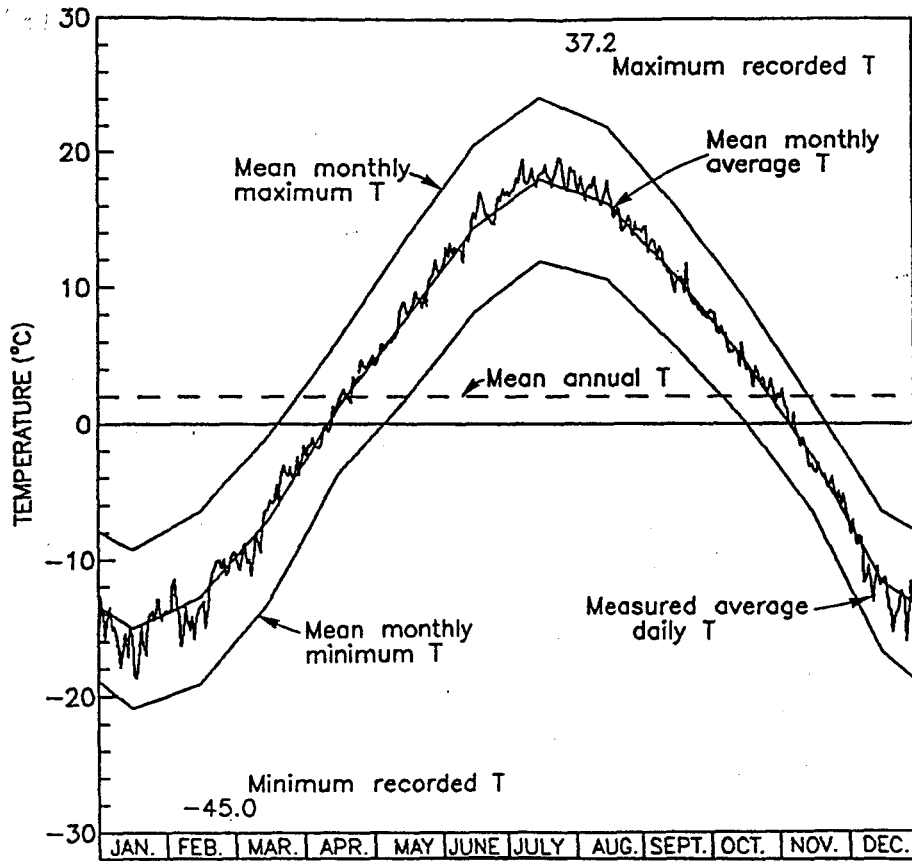
(a) Mean daily and monthly average air temperature record (Leger et al, 1993).
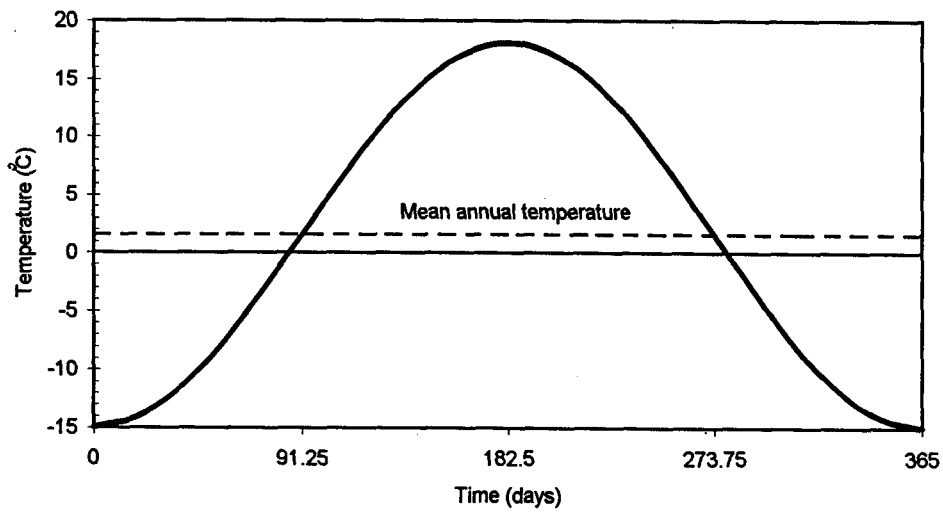
(b) Simplified mean monthly average air temperature.

Figure 5.26 The monthly average temperature of the air.
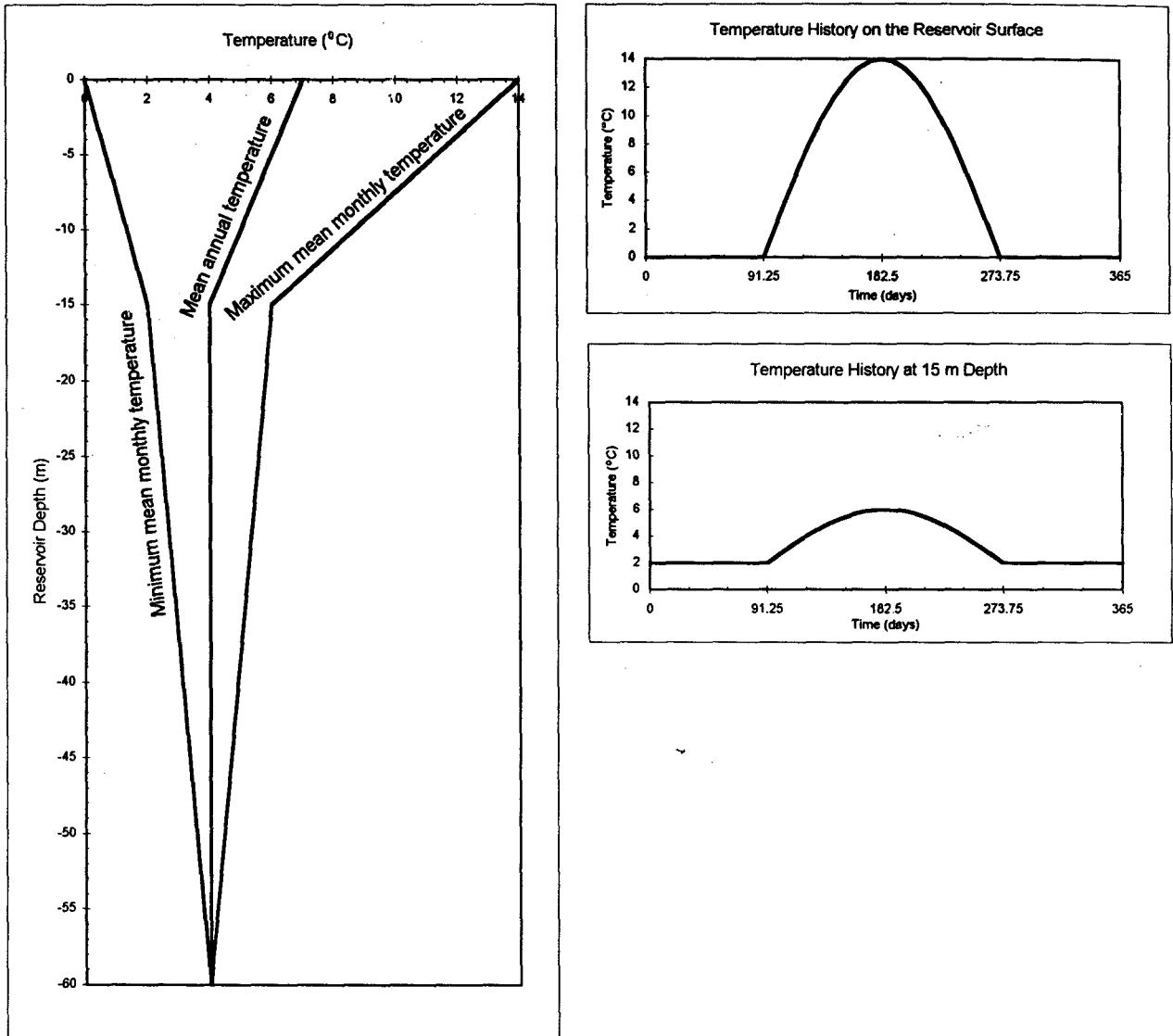
Figure 5.27 The monthly average temperature for the dam-reservoir boundary (Leger *et al.*, 1993).
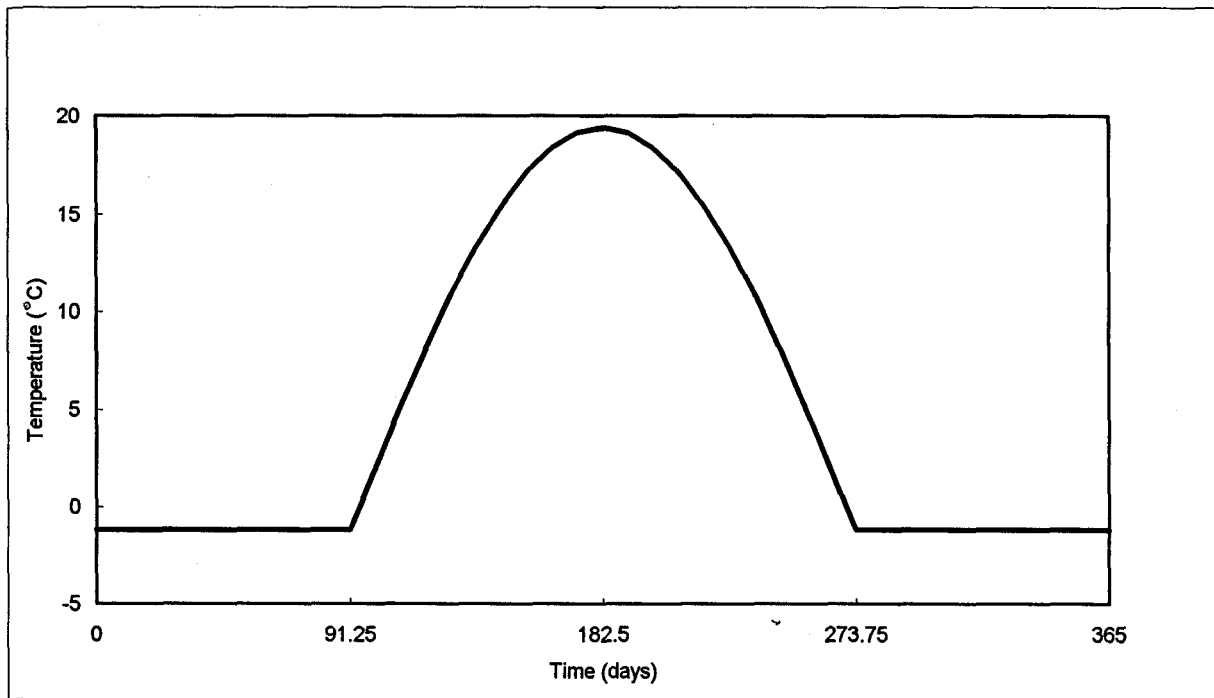
Figure 5.28 The temperature variation on the ground surface.

EG   CLR
1
2

PRESCRIPTED
TEMPERATURE
BOUNDARY

CONVECTION AND RADIATION BOUNDARY

ADIABATIC BOUNDARY
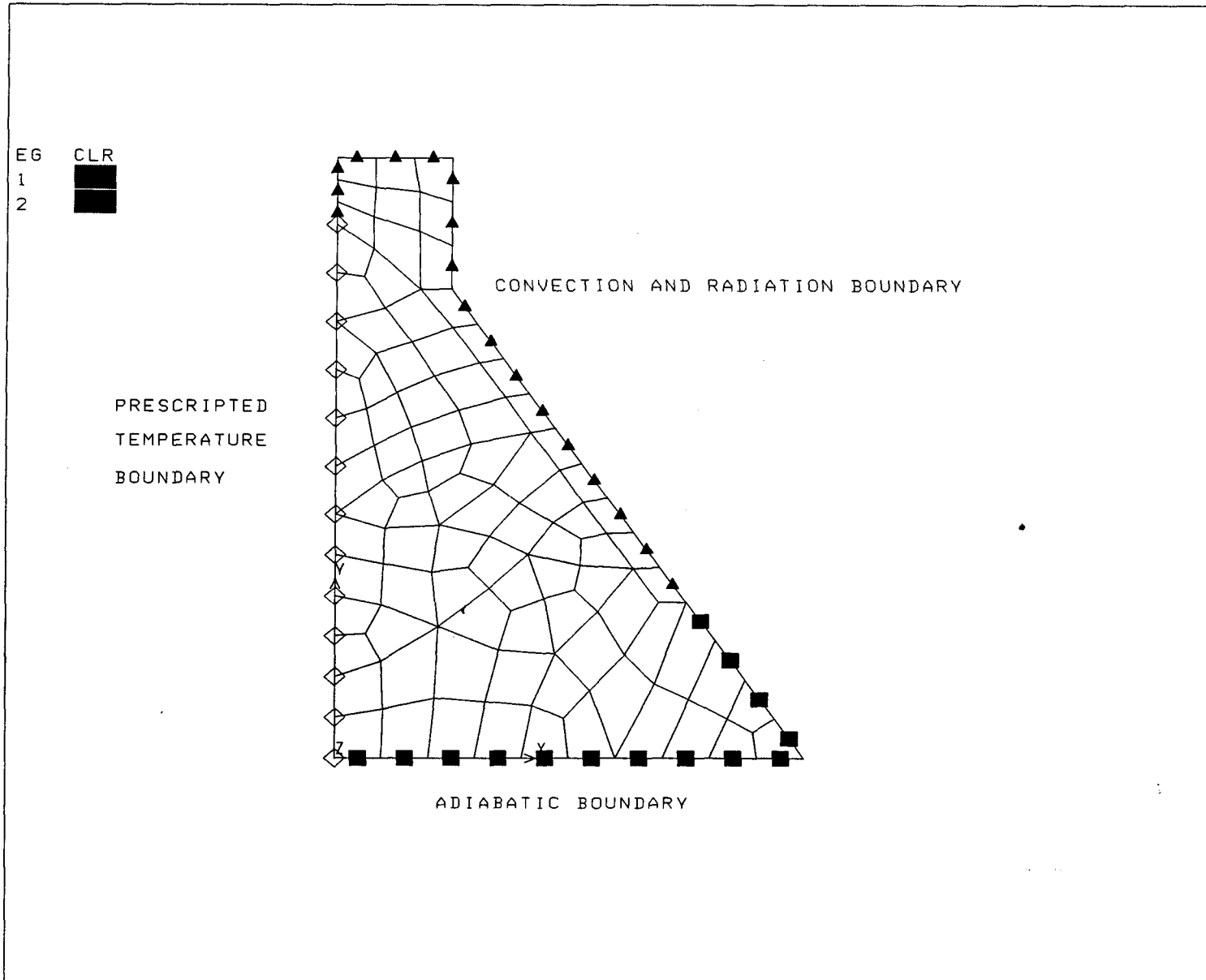
Figure 5.29   The dam model for thermal analysis.

EG CLR
1
2
3
4

CONVECTION AND RADIATION BOUNDARY

PRESCRIPTED TEMPERATURE BOUNDARY

PRESCRIPTED TEMPERATURE BOUNDARY

ADIABATIC BOUNDARY
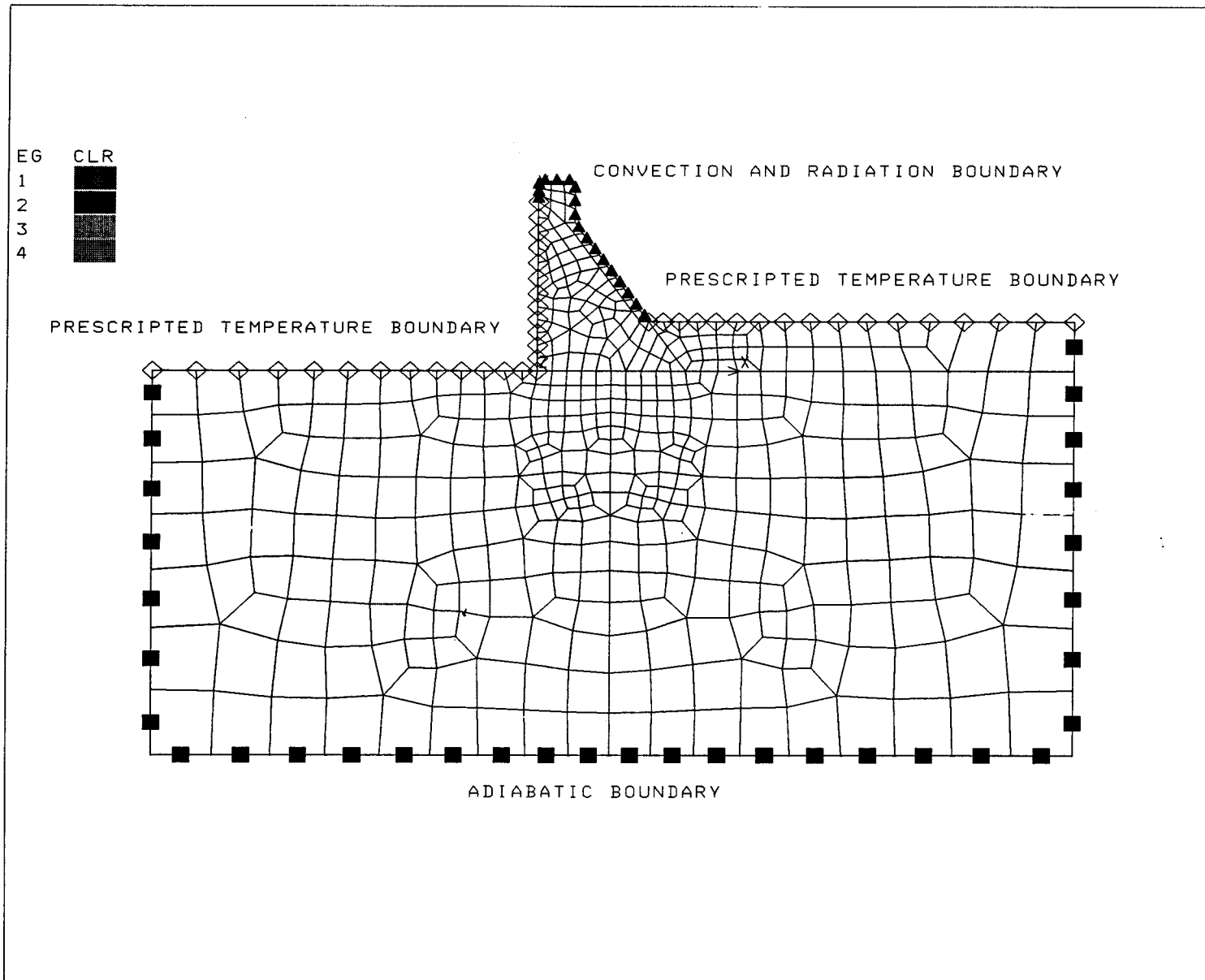
Figure 5.30 The dam-foundation model for thermal analysis.

TEMPERATURE CONTOURS
IN WINTER (MODEL1)

Legend
2.2100
-0.917
-4.040
-7.170
-10.30
-13.40
-16.50
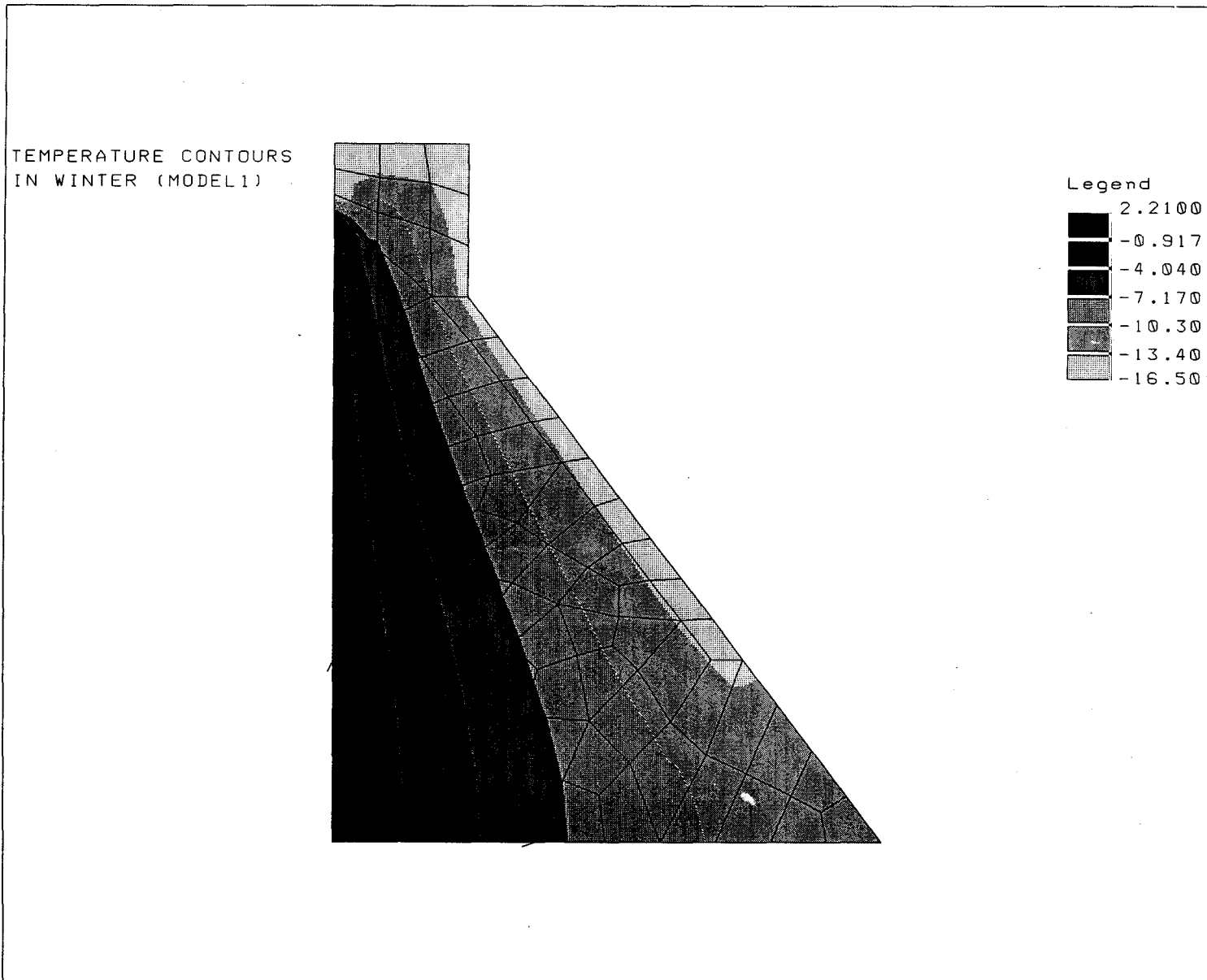
Figure 5.31 Temperature contours in winter (Model 1).

TEMPERATURE CONTOURS
IN WINTER (MODEL2)

Legend
2.2100
-0.908
-4.030
-7.140
-10.30
-13.40
-16.50
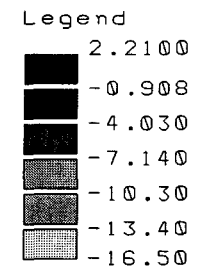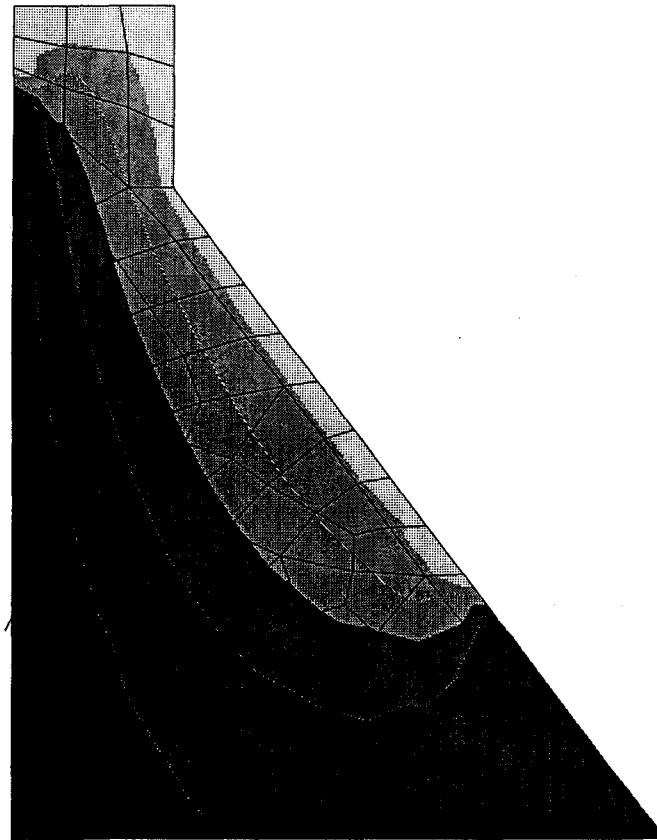
Figure 5.32 Temperature contours in winter (Model 2).

TEMPERATURE CONTOURS
IN SPRING/FALL (MODEL1)
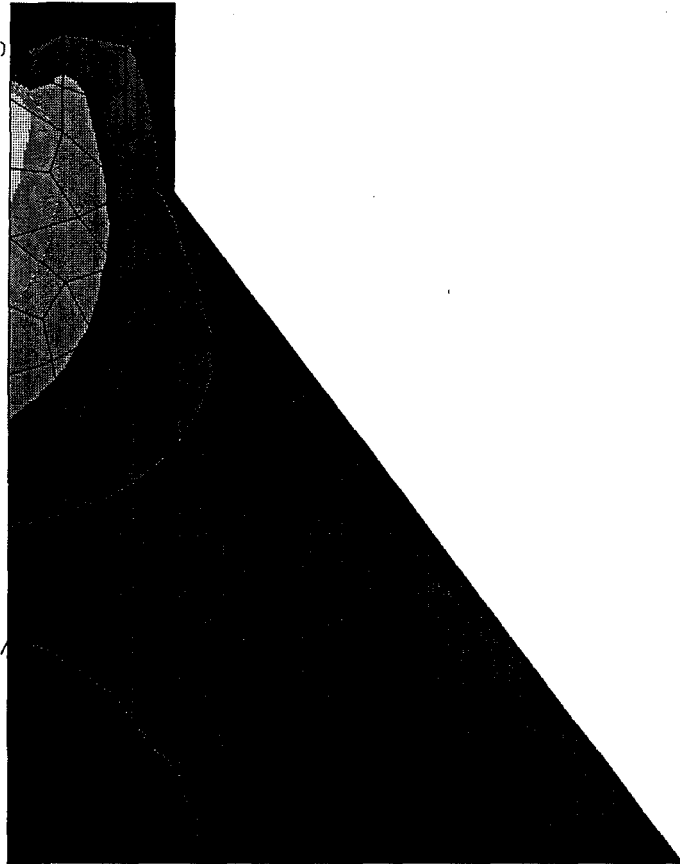
Legend
2.210
1.840
1.470
1.100
0.736
0.368
0.000

Figure 5.33   Temperature contours in spring/fall (Model 1).

Figure 5.34 Temperature contours in spring/fall (Model 2).

TEMPERATURE CONTOURS
IN SUMMER (MODEL1)
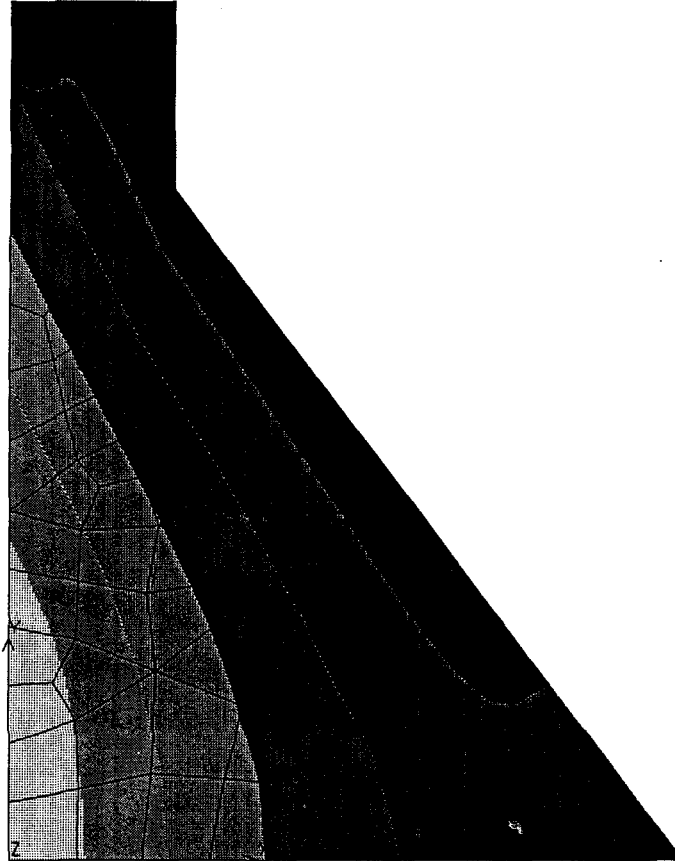
Legend
18.60
16.40
14.30
12.20
10.00
7.920
5.790

Figure 5.35 Temperature contours in summer (Model 1).

TEMPERATURE CONTOURS
IN SUMMER (MODEL2)
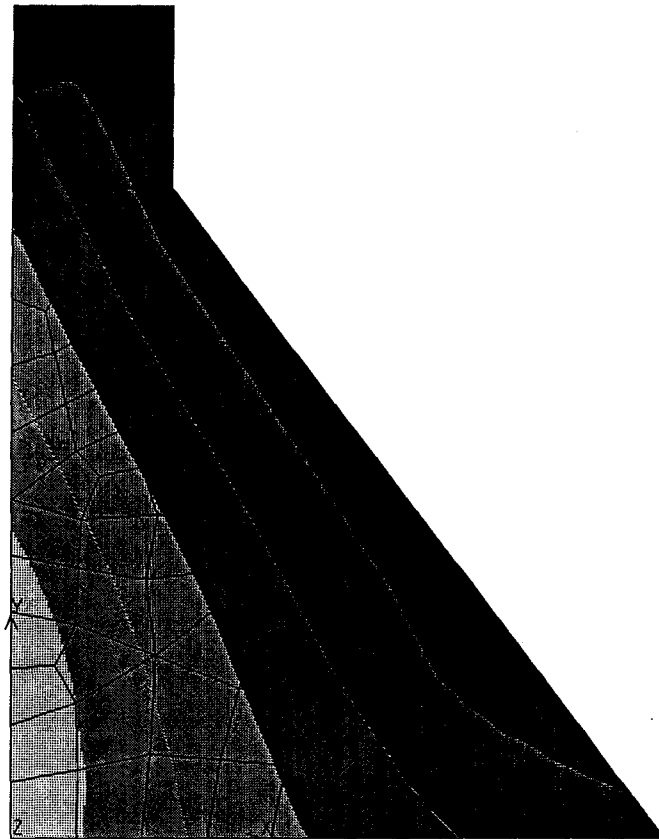
Legend

18.60
16.50
14.30
12.20
10.10
7.930
5.790

Figure 5.36   Temperature contours in summer (Model 2).

HORIZONTAL DISP

FIXED BOTTOM

	0.012100
	0.005250
	-0.00161
	-0.00846
	-0.01530
	-0.02220
	-0.02900
	-0.03590
	-0.04270
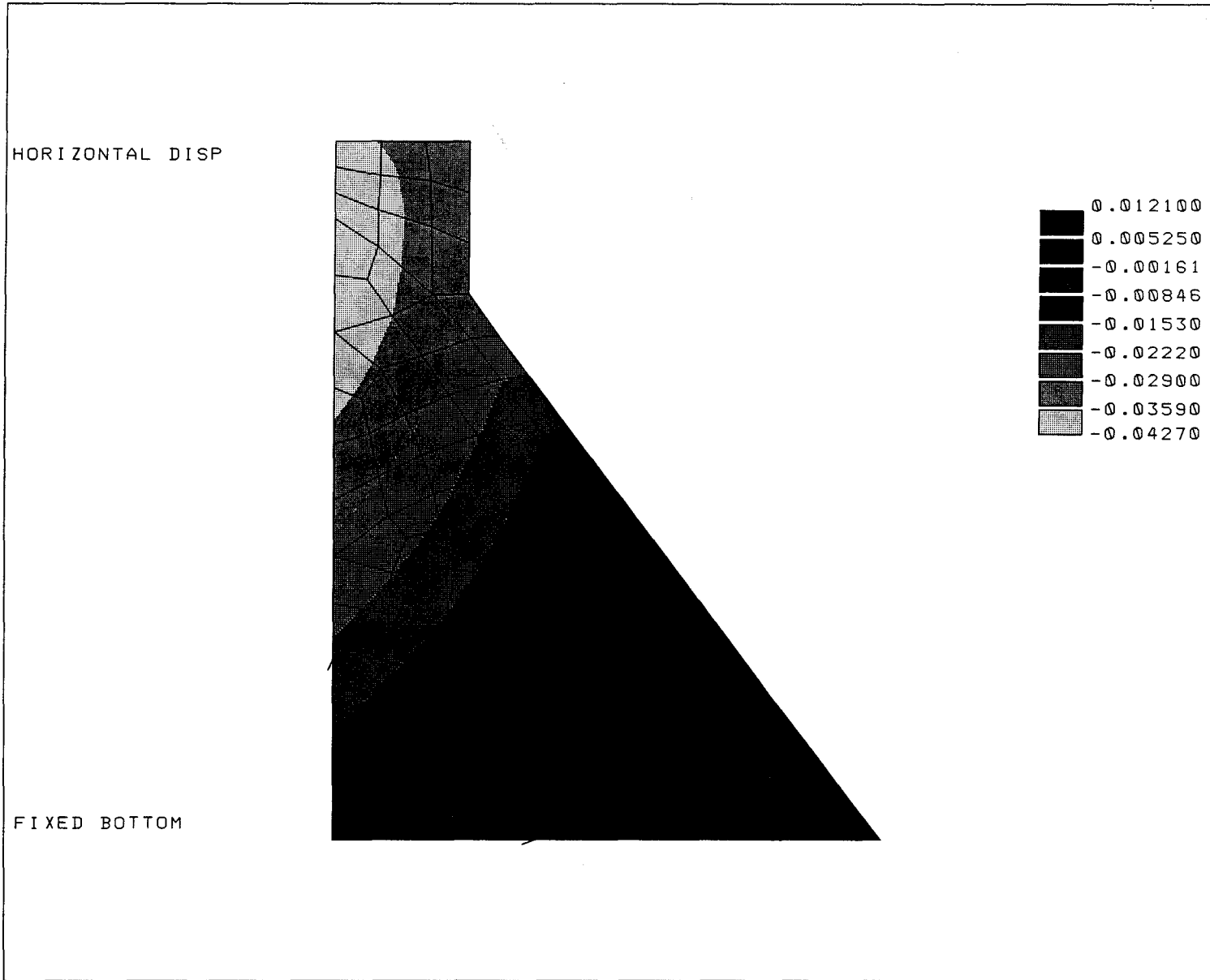
Figure 5.37 The horizontal displacement field after 25 years of AAR (Model 1).

VERTICAL DISP

0.05850
0.05120
0.04390
0.03660
0.02930
0.02200
0.01460
0.00732
0.00000

FIXED BOTTOM

z   x
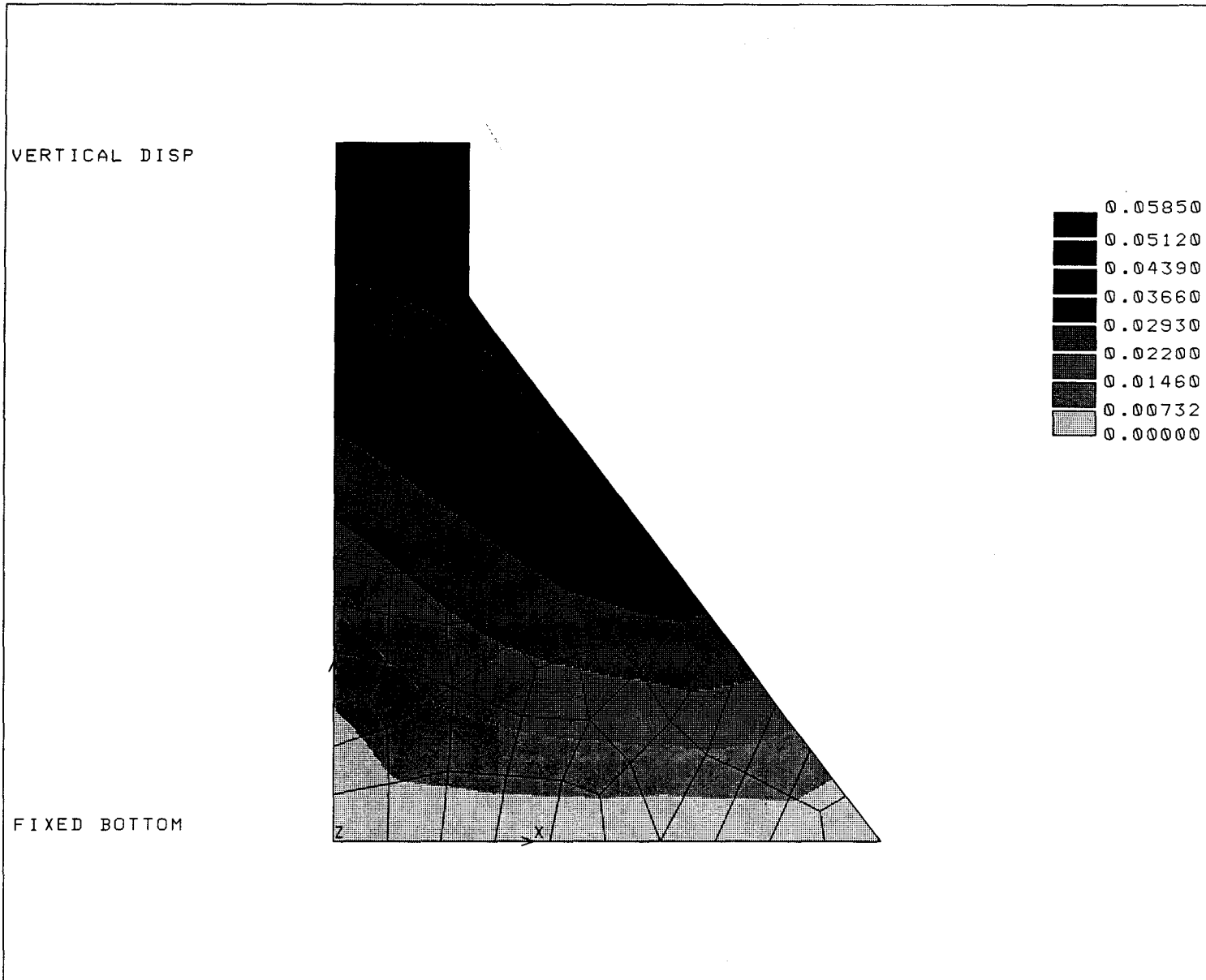
Figure 5.38 The vertical displacement field after 25 years of AAR (Model 1).

BETA

FIXED BOTTOM

1.300
1.200
1.100
1.000
0.900
0.800
0.700

152
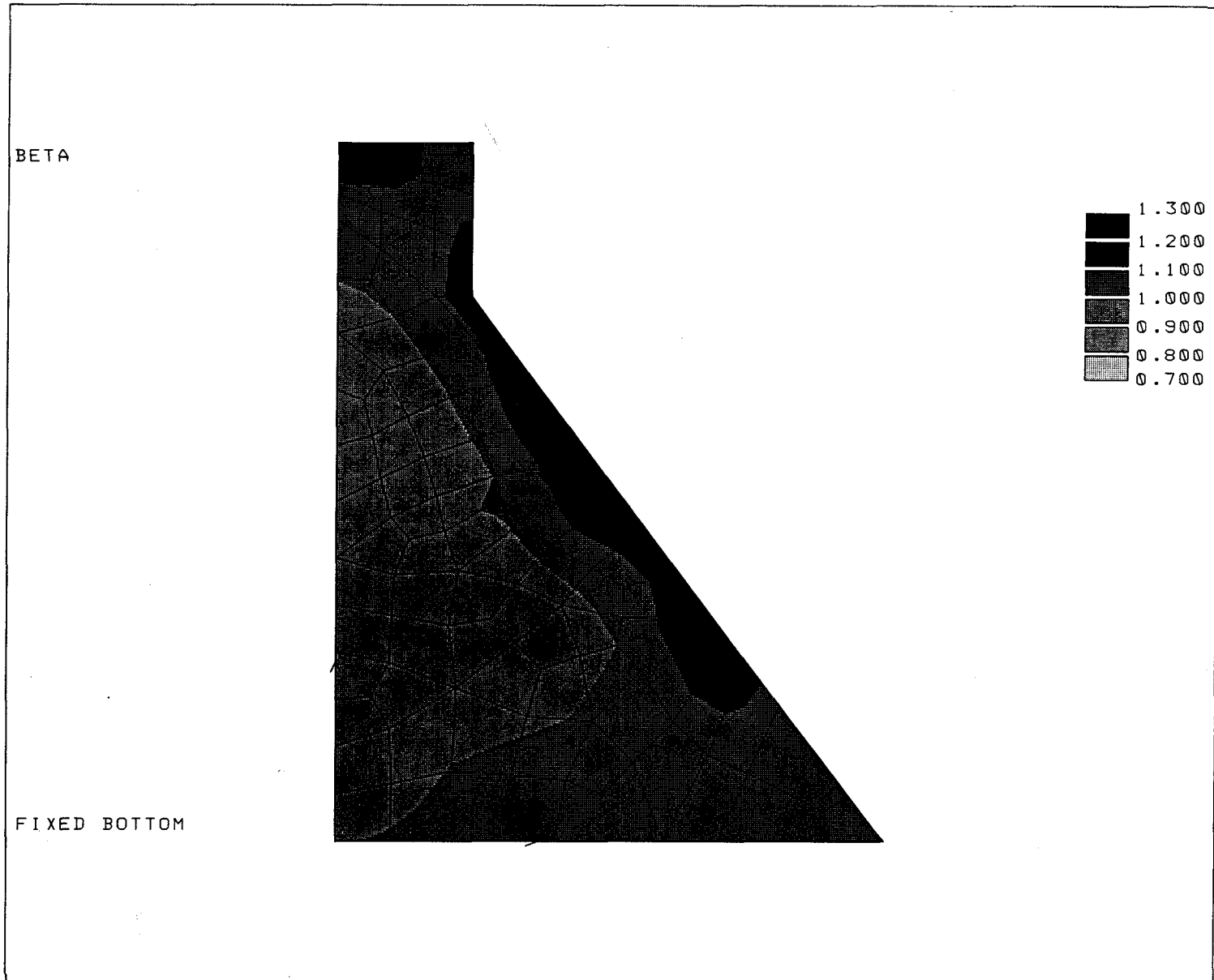
Figure 5.39   The distribution of β after 25 years of AAR (Model 1).

HORIZONTAL DISP

0.011700
0.004760
-0.00220
-0.00917
-0.01610
-0.02310
-0.03010
-0.03700
-0.04400

153
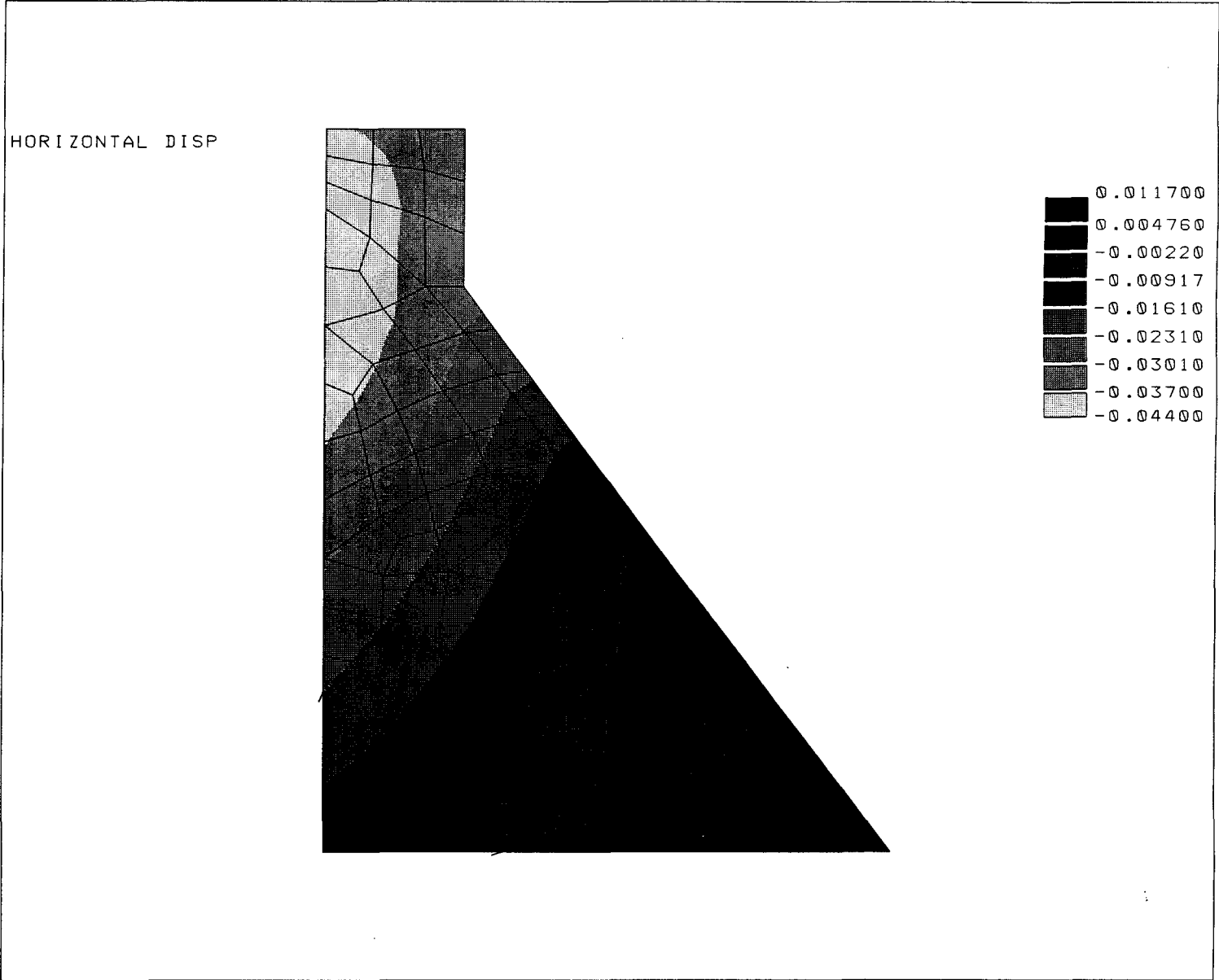
Figure 5.40 The horizontal displacement field after 25 years of AAR (Model 2).

VERTICAL DISP

0.05840
0.05080
0.04330
0.03580
0.02820
0.02070
0.01320
0.00564
-0.0019

Z   X

154
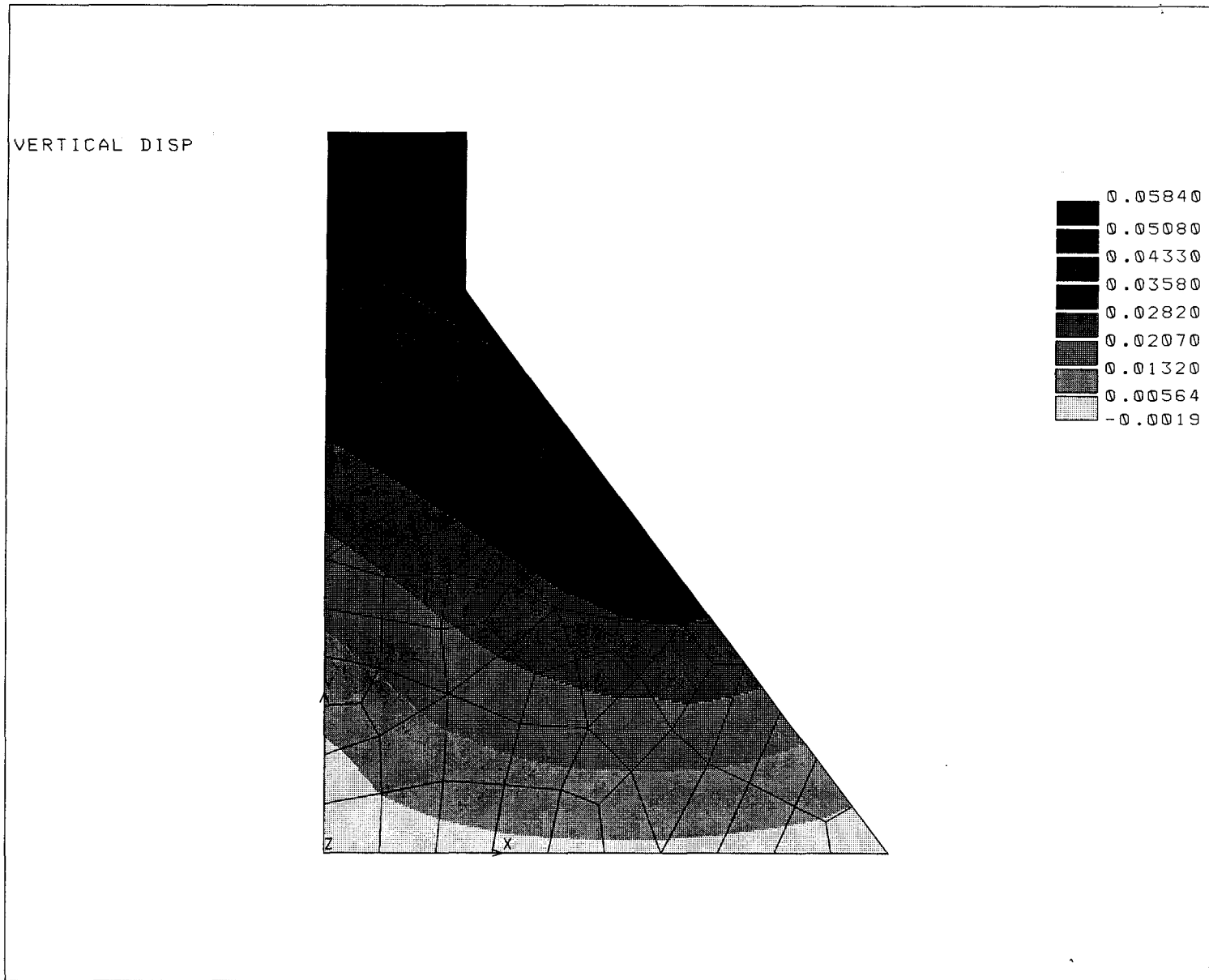
Figure 5.41   The vertical displacement field after 25 years of AAR (Model 2).

EG   CLR
1
2
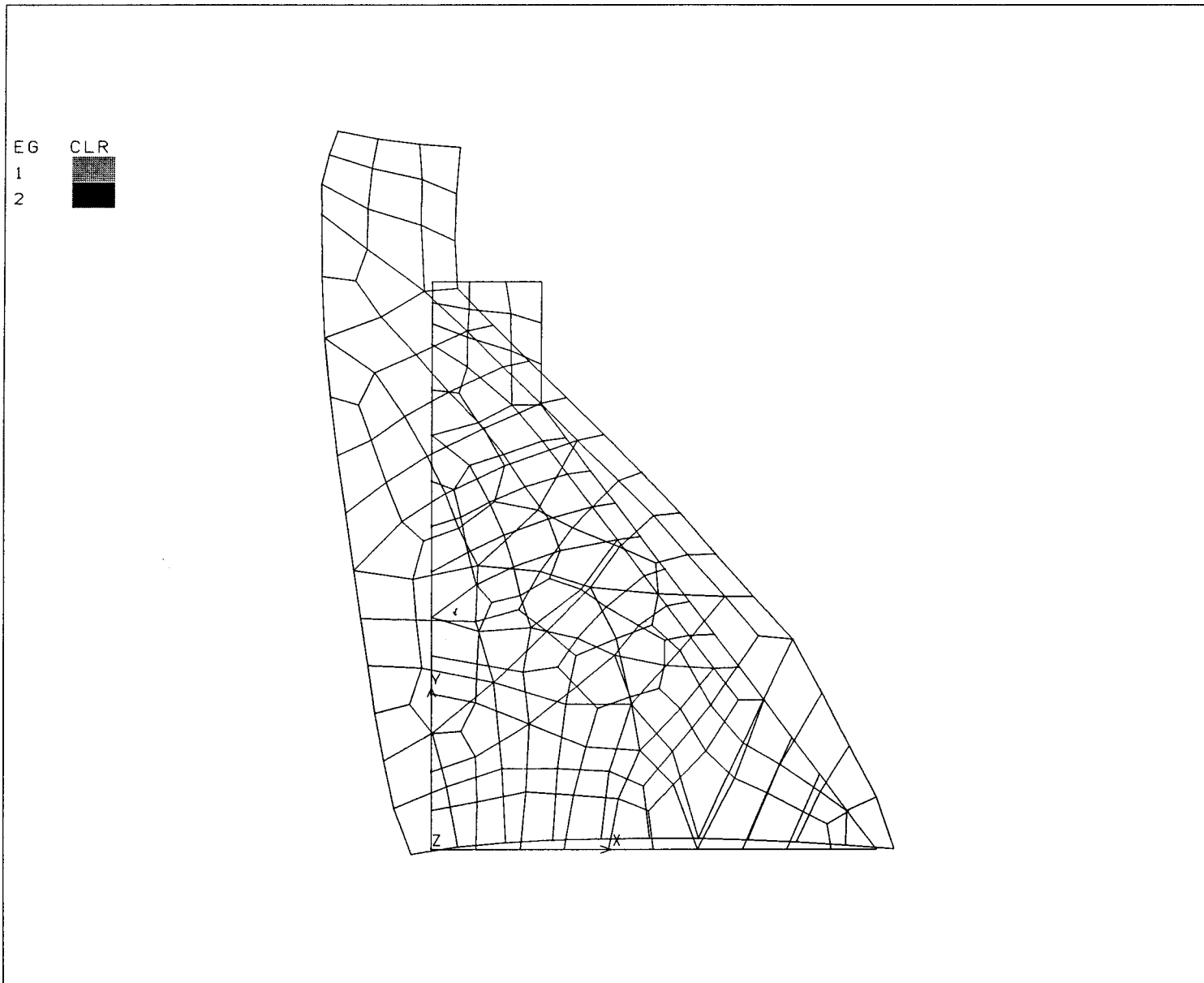
Figure 5.42 The deformed mesh for Model 2.

BETA
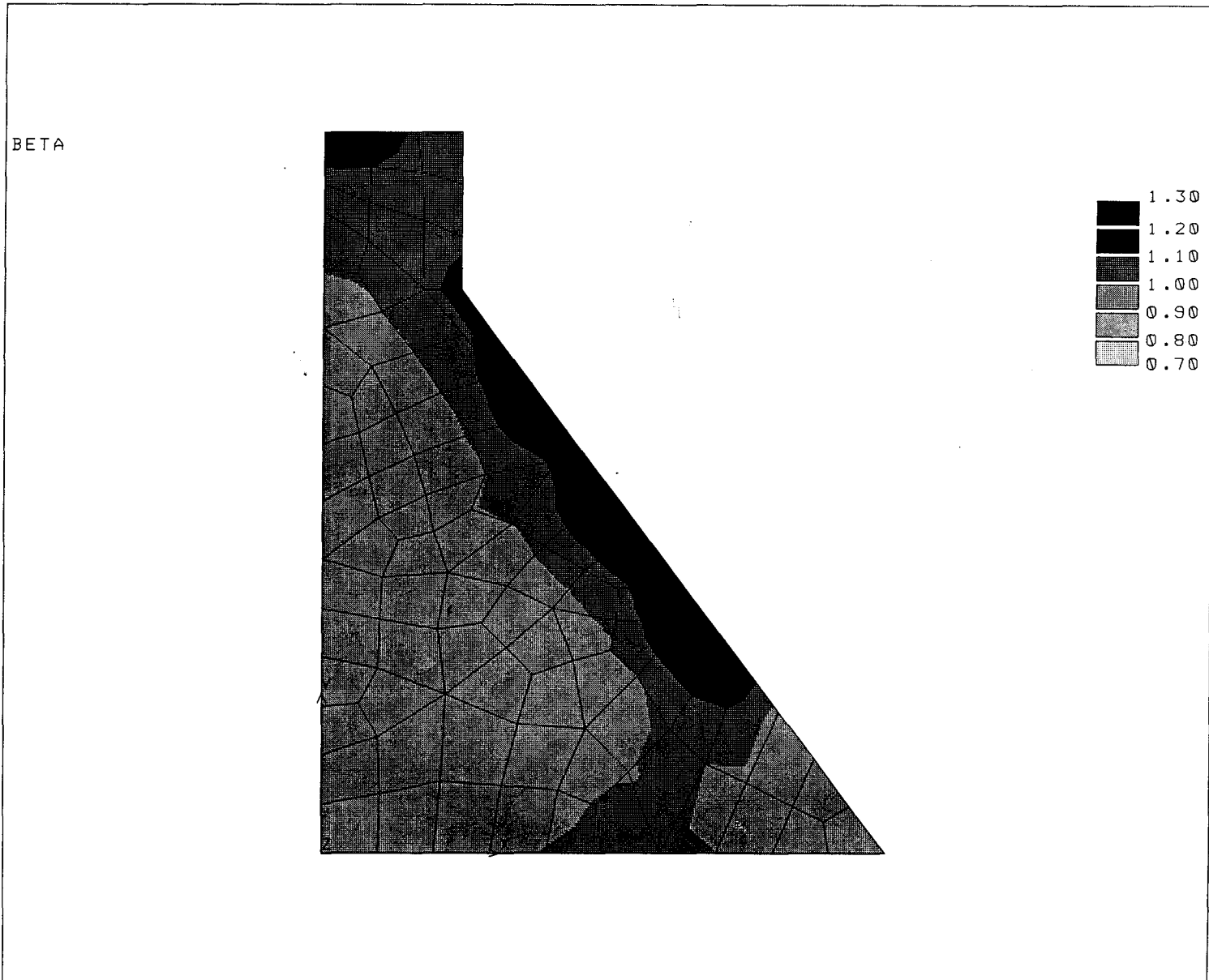
Figure 5.43   The distribution of β after 25 years of AAR for Model 2.
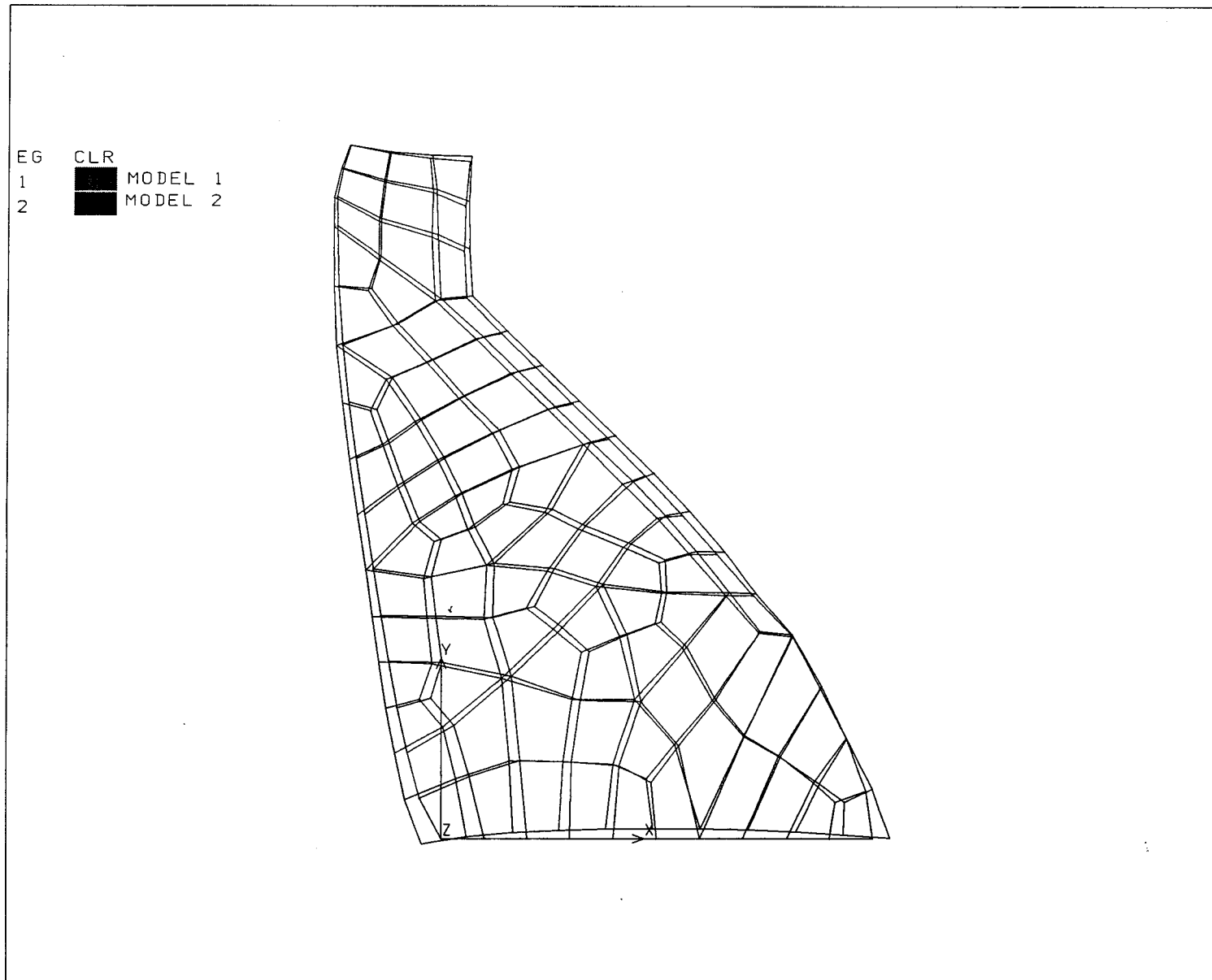
Figure 5.44 Comparison of deformed meshes of the dam for Models 1 and 2.

EG CLR
1   ■ ISOTHERMAL MODEL
2   ■ WITH SEASONAL
      TEMPERATURE VARIATION

DEFORMED MESH COMPARISON
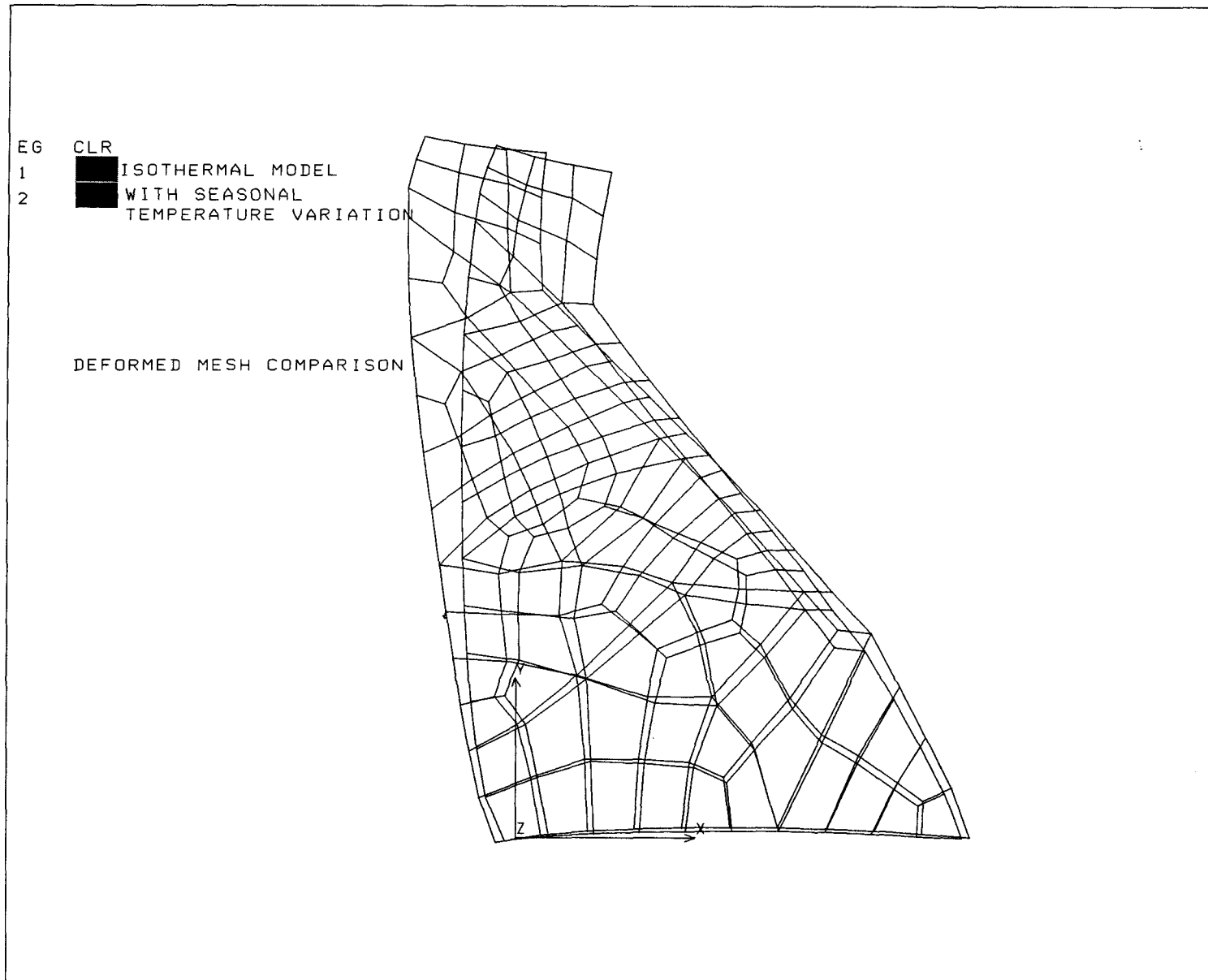
Figure 5.45 Comparison of deformed mesh for Model 2 with that corresponding to isothermal conditions.
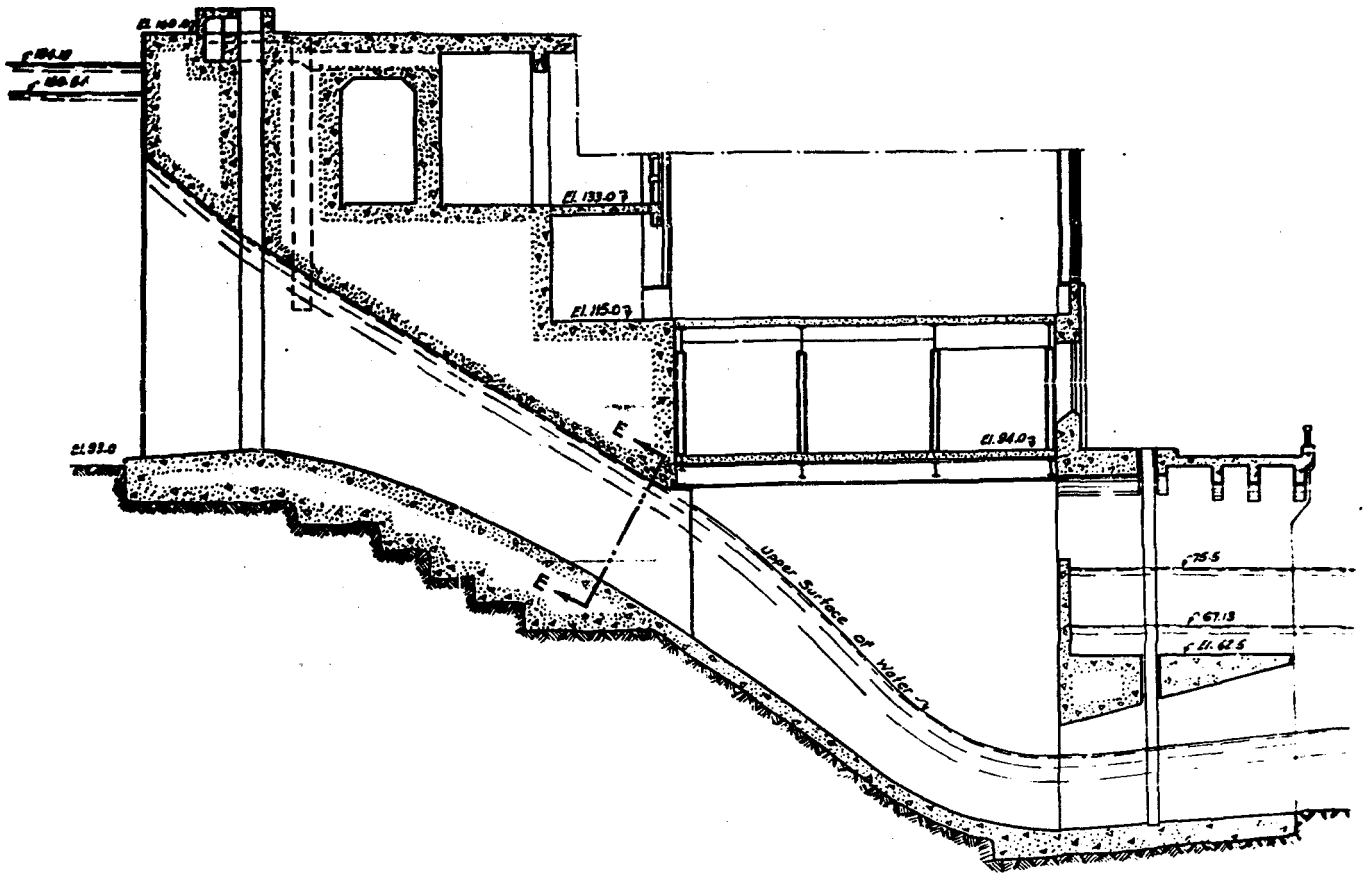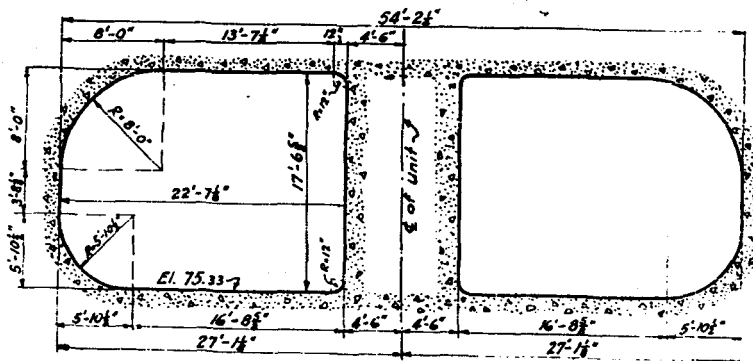
Figure 5.46   The geometry of water intake structure.

EG   CLR
1   ▨
2
3   ▬
4   ▨

ZONE 1
NO EXPANSION

ZONE 2
0% TO 30% OF FULL
EXPANSION DUE TO
LOW RELATIVE HUMIDITY

ZONE 1
FULL EXPANSION DUE TO
HIGH RELATIVE HUMIDITY

y
x
z
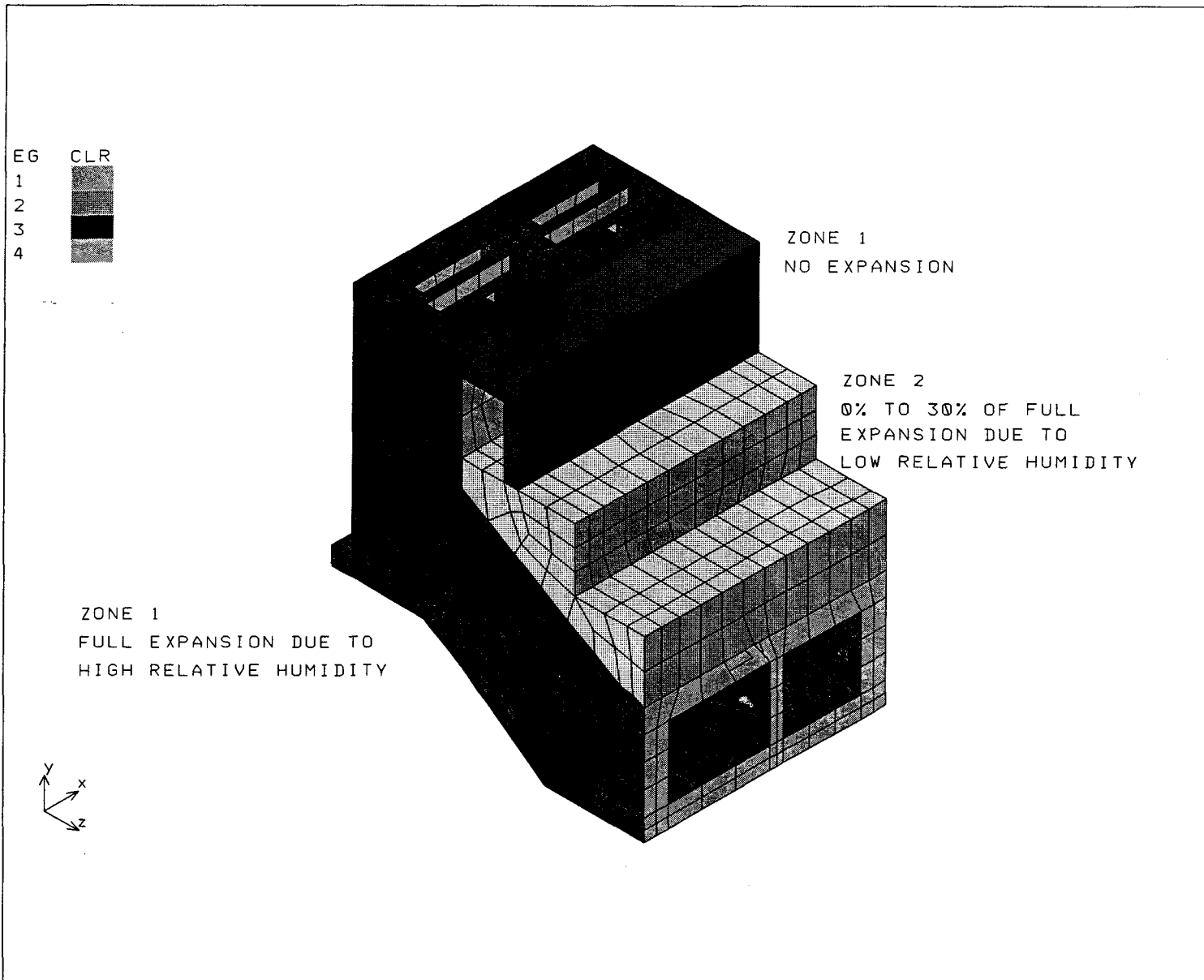
Figure 5.47   The assumed expansion rate distribution in the water intake structure.
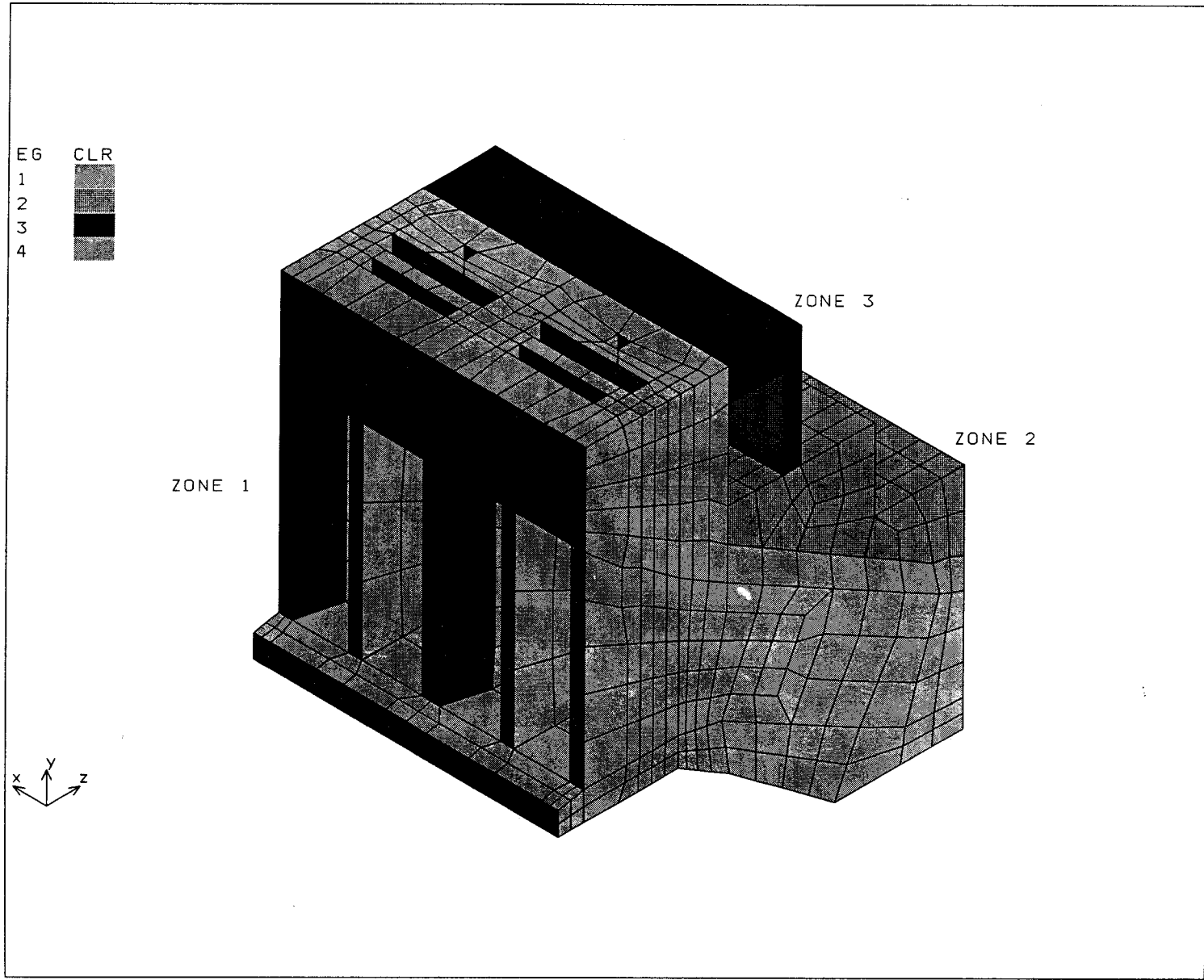
Figure 5.48 The finite element descritization of water intake structure.
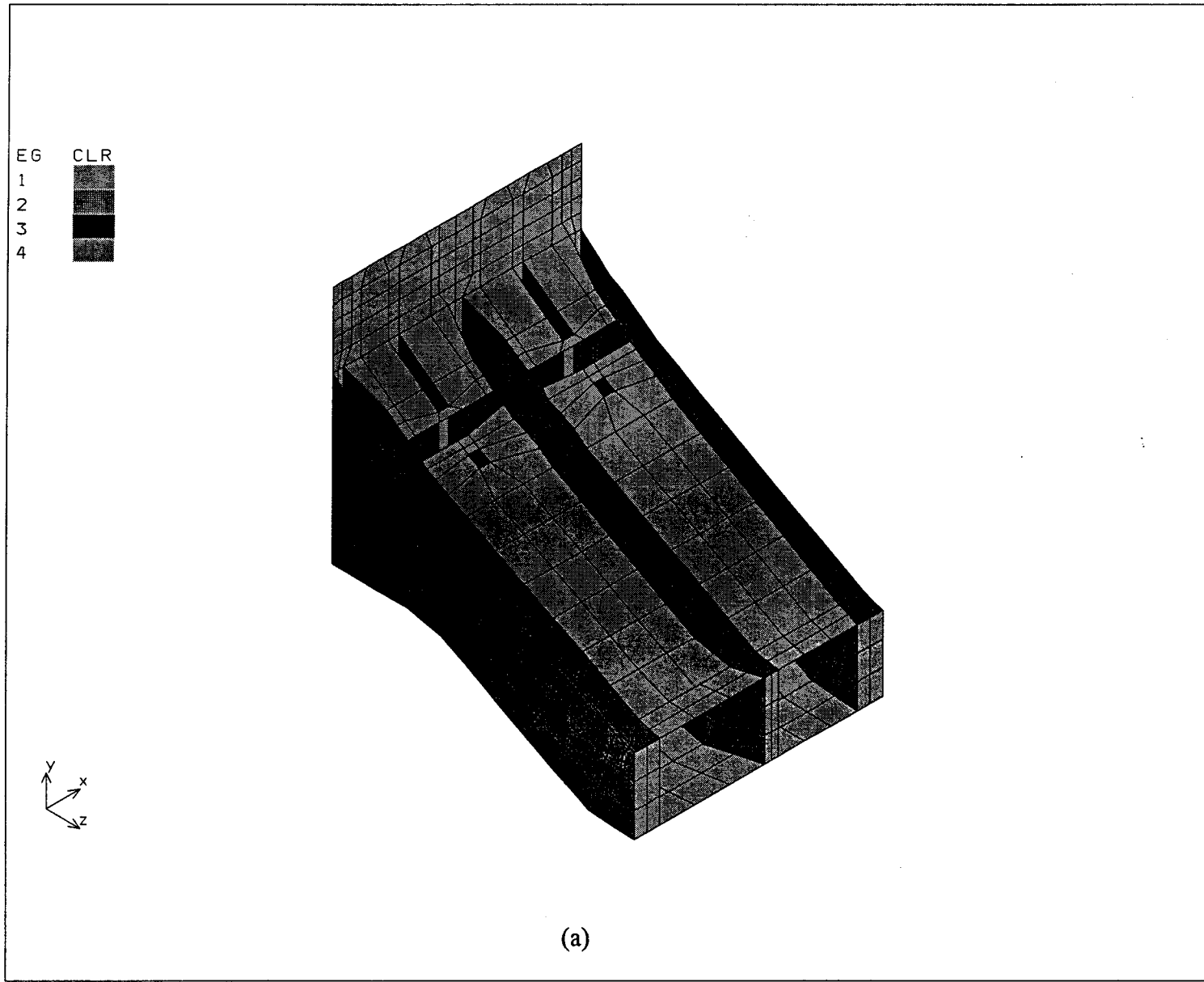
Figure 5.49 The finite element descritization of reinforcement.

(b)
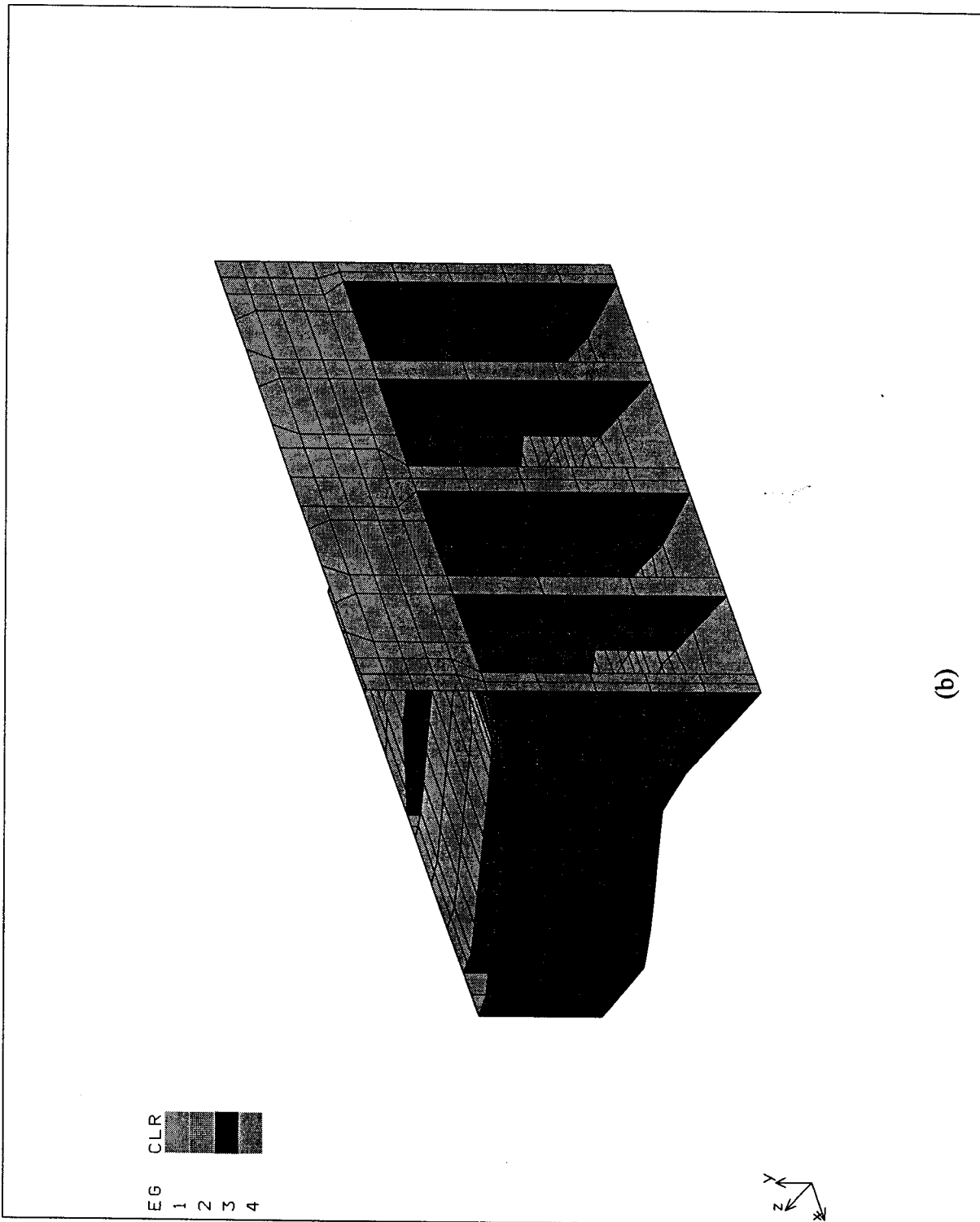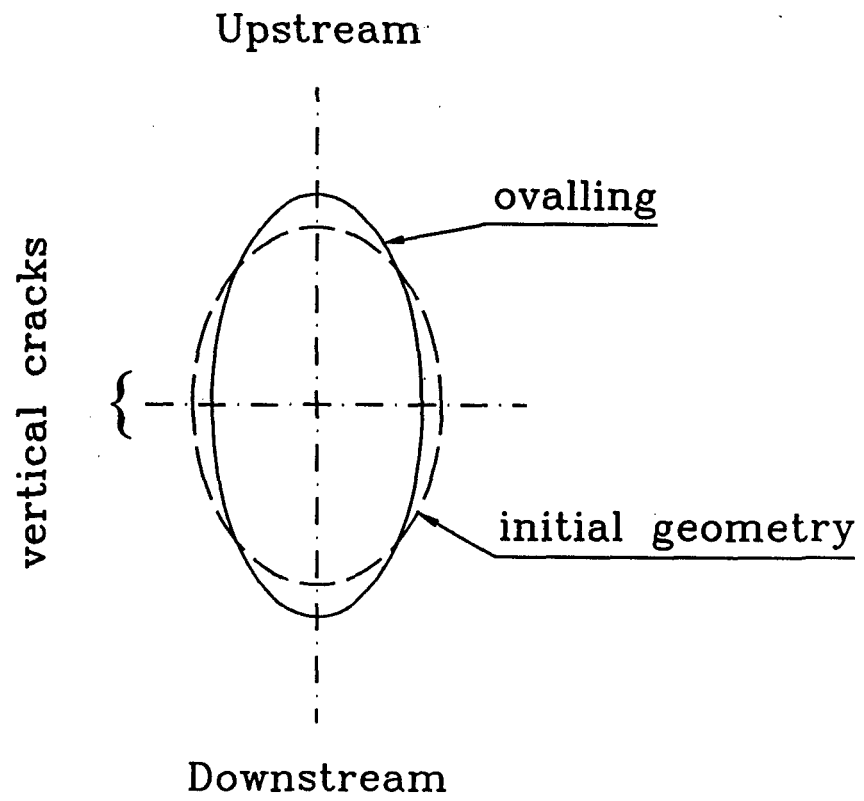
Figure 5.50   Ovalness of the throat ring in the powerhouse (Shawinigan Lavalin Inc., 1992)

VERTICAL DISPALCEMENT (Y-DIRECTIO   (EXPANSION:100%&30%)

■	0.05820
■	0.05090
■	0.04370
■	0.03640
▨	0.02910
▨	0.02180
▨	0.01460
▨	0.00728
▨	0.00000
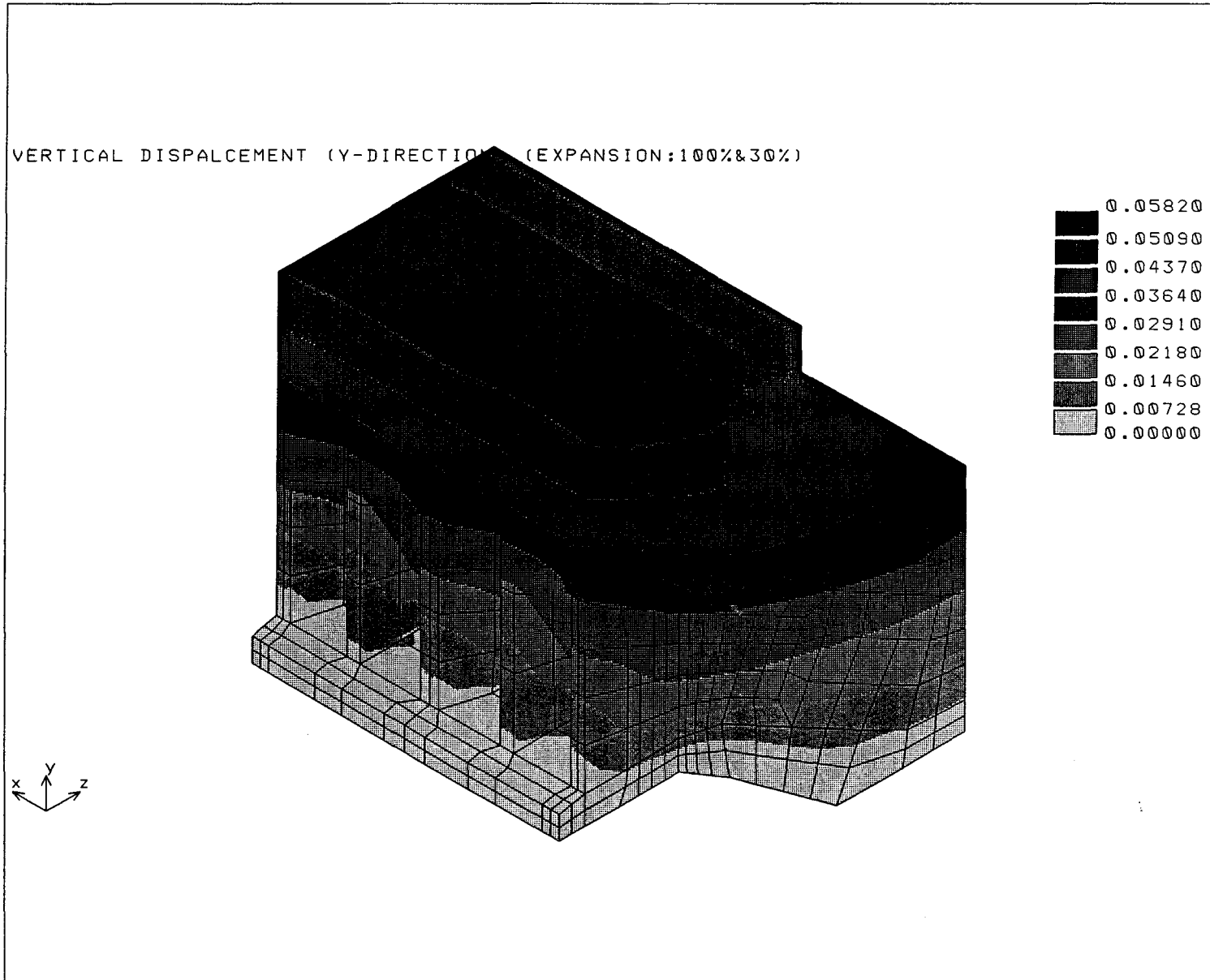
Figure 5.51 The vertical displacement field after 25 years of AAR.
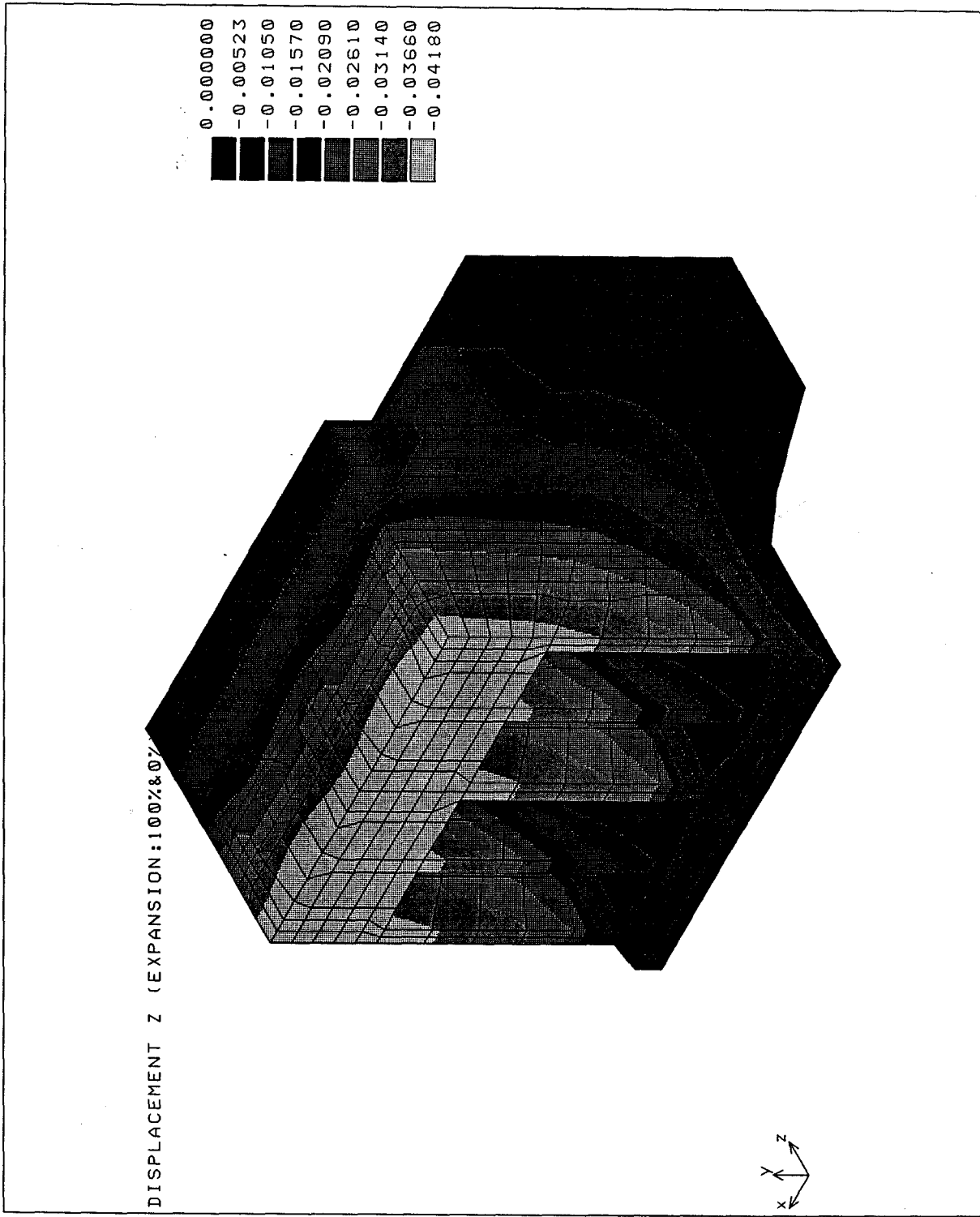
Figure 5.52 The lateral displacement in the z-direction after 25 years of AAR.

BETA (EXPANSION:100%&30%)

■	1.12
■	1.07
■	1.02
■	0.97
■	0.92
■	0.87
■	0.82
■	0.77
□	0.72
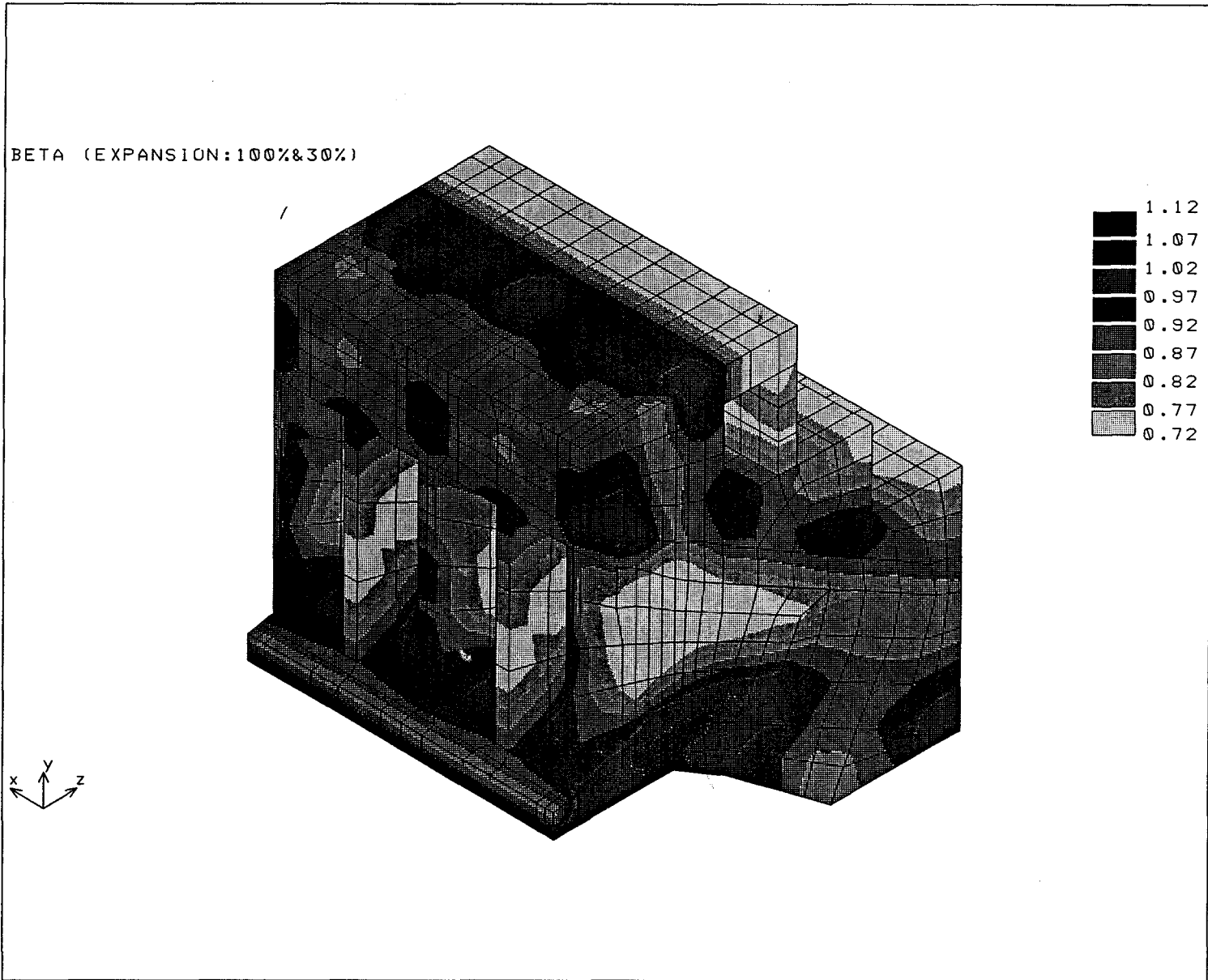
Figure 5.53 The distribution of β after 25 years of continuing AAR (30% expansion rate in zone 2).

BETA (EXPANSION:100%0%)

	1.12
	1.07
	1.02
	0.97
	0.92
	0.87
	0.82
	0.77
	0.72
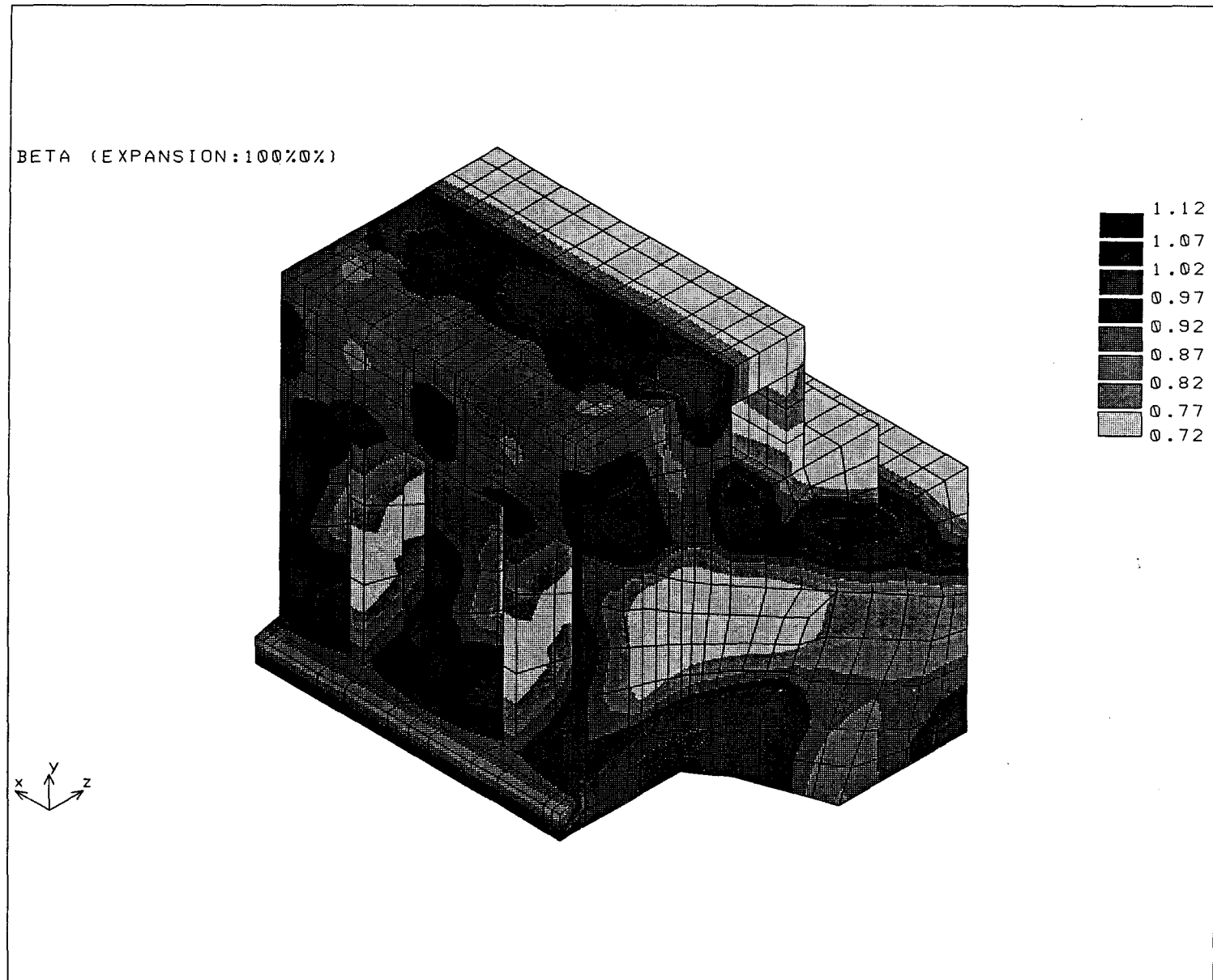
Figure 5.54 The distribution of β after 25 years of continuing AAR (0% expansion rate in zone 2).

Chapter 6

Summary and Recommendations for Future Research

6.1 Summary of the Present Study

Since alkali-aggregate reaction was first identified in early 1940's, an increasing number of concrete structures have been found suffering from durability problems due to AAR. Presently, there is virtually no country which can claim immunity from AAR-induced concrete deterioration in existing structures. Over the last decade, extensive interdisciplinary research has been carried out. One of the important aspects in the research pertains to the modeling of the effect of AAR on the mechanical response of existing structures, in particular to what extent a further progress in the reaction threatens the stability of these structures. This has been the main focus of the study presented here.

First, the existing literature on the response of concrete subjected to AAR was extensively reviewed. The emphasis was placed on those aspects which were considered the most important in the formulation of the constitutive model and the finite element analysis of AAR-damaged structures.

A constitutive model was presented based on the framework proposed by Pietruszczak (1996). The expansion rate was assumed to be influenced by the confining pressure, the age of concrete and the temperature. The progress in reaction was coupled with the degradation of mechanical properties. The concrete was assumed as an elastoplastic medium and the constitutive model proposed by Pietruszczak et al. (1988) was adopted in

medium and the constitutive model proposed by Pietruszczak *et al.* (1988) was adopted in the formulation. Numerical examples were provided for both the isothermal and non-isothermal conditions. The procedures for generating the finite element model and the interfacing operations were then presented.

A typical cross-section of south wing dam of the Beauharnois complex was chosen for a finite element analysis. The constitutive model was implemented in the finite element code and the structural response under isothermal conditions and seasonal temperature variation was simulated. Parametric studies of the effect of the foundation stiffness and relative humidity of the concrete were carried out. A three-dimensional finite element model was developed for a water intake structure, and a finite element analysis was performed simulating the effects of 25 years of continuing reaction.

6.2 Conclusions

The simulations of the mechanical response of concrete subjected to AAR under isothermal conditions and seasonal temperature variation have been carried out. The constitutive model describing the progress in AAR has been successfully used in predicting long-term response of concrete structures. The results of this research are still preliminary, and no definite quantitative conclusions can be draw. This is mainly due to the lack of experimental data pertaining to identification of material parameters involved.

Seasonal temperature variation causes non-uniform reaction in concrete. Thus, the rates of expansion and degradation of material properties are not uniformly distributed within the

Most severe cracking occurs near the exposed surfaces due to low relative humidity and high temperature in the summer. The geometry of the structure will influence the degree and location of cracking. In general, severe cracking occurs in the bulkly and concave sections of the structure.

For thermal analysis, the foundation has little effect on the distribution of temperature in the structure. In mechanical simulations, however, the stiffness of the foundation will significantly effect the response in the lower part of the structure. In particular, the stress intensity factor, β, near the bottom of the structure increases significantly with an increase in the stiffness of the foundation.

6.3 Recommendations for Future Research

The behavior of concrete subjected to AAR is comprised of a complex interaction of many effects. In the present research, some most important aspects, including degradation of material properties, influence of confining stress, temperature and relative humidity, have been studied. In the following, some recommendations for future research are draw from the present study.

An extensive experimental program is required. Several material parameters in the constitutive model have been chosen on purely intuitive basis. Although there are numerous test results currently available, these are not based on a systematic study involving one specific material. The results of numerical simulations may be significantly affected by the choice of material parameters.

A large scale multi-unit finite element model is required to improve the accuracy of the analysis. In this study, only single-unit structures were analyzed. The results of the simulations may be affected by the approximation of the boundary conditions. The main difficulty for modeling the entire structure is to generate a workable finite element model.

An analysis of the response of AAR-damaged structures to earthquake excitation would be desirable. The continuing AAR causes severe cracking and degradation of material properties. It would be of interest to investigate if the stability of these structures is at risk under typical seismic load.

A common strategy to release the AAR-induced pressures and leave tolerance for the further AAR expansion is to cut slots in the structure. The location and dimension of the slots are determined by the structural expansion behavior and the existing damage condition. It would be desirable to perform an appropriate numerical investigation of the long-term effects of this procedure.

Finally, the method of the graphical representation of the numerical results needs to be improved. In this study, the contours of the hardening parameter β were approximated to be an average value within each element. This assumption may reduce the accuracy of the results in the graphical representation. Better approximation techniques could be developed.

Appendix A

COS2PLAS.C

```c
#include <stdio.h>

#include <string.h>

#include <process.h>


#define MAXNODE 2000

#define MAXELEM 2000

#define MAXCONSTRAIN 500

#define MAXPRESS 30


#define NTYPE 2 /* 1=Plane stress; 2=Plane strain; 3=Axial symmetry. */

#define NMATS 4

#define NGAUS 4

#define NALGO 3 /* 1=Initial stiffness method; 2=Tangential stiffness method;
                    3=Combined algorithm (v.1); 4=Combined algorithm (v.2). */

#define NCRIT 5 /* 1=Tresca; 2=Von Mises; 3=Mohr-Coulomb; 4=Drucker-Prager;
                    5=User defined Model drive*/

#define STEP_STATIC 2

#define STEP_CREEP 25


struct Node{

  float x,y;

};

struct Element{

  int node[4],mtl;

};
```

```
int detJ();

char Modes[11][5]={"EG", "ND,", "EL,", "DND,",  "PEL,"},

     GPS[6]="GPS",UX[4]="UX,",UY[4]="UY,";

FILE *inf,*opf,*newf,*n12f,*tmpf;



/* * * * * * * * * * * * * * * * * * * * * * * * * * * * * * * * * * * * * *

 *                          COS2PLAS.C                                    *

 *                      ----- 2D Version -----                            *

 *                                                                        *

 *   This program reads data from COSMOS/M GFM and RMN files, then,       *

 *   optimizes nodes and converts the data format into the PLASTEX input  *

 *   file format. The optimized COSMOS/M Model is saved in the NEW file.  *

 *   The new model for material sets 1 & 2 is saved in the N12 file.      *

 *                                                                        *

 *   Use:  COS2PLAS [cosmos problem name] > [plastex input file name].    *

 *                                                                        *

 * * * * * * * * * * * * * * * * * * * * * * * * * * * * * * * * * * * * * */

                         '

main(argc,argv)

int argc;

char *argv[];

{

  float LocalX[8],LocalY[8];

  int   NumNode,NumEle,NumDisp,NumPres,i,j,k,NpE,Mode,nnm,EleGrp,

        OptND[MAXNODE],DispN[MAXNODE],n12[MAXNODE];

  char  gfm[13],rnm[13],new[13],s[18],

        pel[MAXPRESS][5],Pressure[MAXPRESS][12],

        Face[MAXPRESS],ch;

  struct Node OldND[MAXNODE], NewND[MAXNODE], Constrain[MAXCONSTRAIN];

  struct Element Ele[MAXELEM];
```

```
strcpy(gfm,argv[1]);

strcat(gfm,".GFM");

if((inf=fopen(gfm,"r"))==NULL){

  printf("Can't open %s",gfm[1]);

  exit(1);

}

strcpy(rnm,argv[1]);

strcat(rnm,".RNM");

if((opf=fopen(rnm,"r"))==NULL){

  printf("Can't open %s",rnm[1]);

  exit(1);

}

strcpy(new,argv[1]);

strcat(new,".NEW");

if((newf=fopen(new,"w"))==NULL){

  printf("Can't open %s",new[1]);

  exit(1);

}

strcpy(n12,argv[1]);

strcat(n12,".N12");

if((n12f=fopen(n12,"w"))==NULL){

  printf("Can't open %s",n12[1]);

  exit(1);

}

for(i=0;i<MAXNODE;i++){

  OldND[i].x=0;

  OldND[i].y=0;

  NewND[i].x=0;

  NewND[i].y=0;

  Constrain[i].x=0;
```

```
      Constrain[i].y=0;

}

EleGrp=0;

NumNode=0;

NumEle=0;

NumDisp=0;

NumPres=0;

while(fscanf(inf,"%s\n",s)!=EOF){

   Mode=99;

   for(i=0;i<7;i++){

      if(strcmp(s,&Modes[i][0])==NULL) Mode=i;

   }

   switch(Mode){

      case 0: fscanf(inf,"%d",&EleGrp);

              break;

      case 1: NumNode++;

              fscanf(inf,"%s",&s);

              nnm=atoi(s);

              fscanf(inf,"%f %f",&OldND[nnm].x,&OldND[nnm].y);

              break;

      case 2: fscanf(inf,"%d %c %s %s %d",&j,ch,s,s,&NpE);

              Ele[j].mtl=EleGrp;

              for(i=0;i<NpE;i++) fscanf(inf,"%d",&Ele[j].node[i]);

              NumEle++;

              break;

      case 3: fscanf(inf,"%s",&s);

              j=atoi(s);

              fscanf(inf,"%s ",&s);

              if(strcmp(&s,&UX[0])==NULL) Constrain[j].x=1;

              if(strcmp(&s,&UY[0])==NULL) Constrain[j].y=1;
```

```
                    break;

        case 4: fscanf(inf,"%s %s %d ",

                pel[NumPres],Pressure[NumPres],&Face[NumPres]);

                NumPres++;

                break;

    }

}

NumDisp=0;

for(i=1;i<=NumNode;i++){

    if((Constrain[i].x==1)||(Constrain[i].y)==1)NumDisp++;

}

while(fscanf(opf,"%s",&s)!=EOF){        /* Search optimized node order. */

    if(strcmp(s,&GPS[0])==NULL){

        for(i=0;i<13;i++) fscanf(opf,"%s",&s);

        for(i=1;i<=NumNode;i++){

        fscanf(opf,"%d",&j);

        fscanf(opf,"%d %s",&OptND[j],&s);

        }

    }

}

fprintf(newf,"ACTSET CS 0\n");

fprintf(n12f,"ACTSET CS 0\n");

switch(NTYPE) {

    case 1:

        j=3;

        break;

    case 2:

        j=3;

        break;

    case 3:
```

```
      j=4;

      break;

    defaut:

      printf("Problem type paremeter NTYPE defination error.");

      exit(1);

  }

  printf("Title\n");

  printf(" %d  %d  %d  %d  %d  %d  %d  %d  %d  %d  %d\n",

          NumNode, NumEle, NumDisp, NTYPE, NpE, NMATS, NGAUS, NALGO, NCRIT,

          STEP_STATIC+STEP_CREEP, j);

/* Convert node order into optimized order. */

  for(i=1;i<=NumNode;i++){

    j=OptND[i];

    NewND[j].x=OldND[i].x;

    NewND[j].y=OldND[i].y;

  }

/* Print node coordinates to the NEW file. */

  for(i=1;i<=NumNode;i++){

    fprintf(newf,"ND,  %d,  %f  %f \n",i,NewND[i].x,NewND[i].y);

  }

/* Convert and print element nodal order.

   The element nodal order is counter-clockwise in PLASTEX.  */

  for(i=0;i<=MAXNODE;i++) n12[i]=0;

  for(i=1;i<=NumEle;i++){

    for(k=0;k<NpE;k++){

      LocalX[k]=OldND[Ele[i].node[k]].x;

      LocalY[k]=OldND[Ele[i].node[k]].y;

    }

    printf(" %d   %d  ", i+1,Ele[i].mtl);

    if(detJ(LocalX,LocalY)>0)
```

```
     for(k=0;k<NpE;k++) printf(" %d   ",OptND[Ele[i].node[k]]);

   else

     printf(" %d   %d   %d   %d",

     OptND[Ele[i].node[0]],OptND[Ele[i].node[3]],

     OptND[Ele[i].node[2]],OptND[Ele[i].node[1]]);

   printf("\n");

   fprintf(newf,"EL, %d, SF %d, %d",i+1,Ele[i].mtl,NpE);

   for(k=0;k<NpE;k++) fprintf(newf," %d ",OptND[Ele[i].node[k]]);

   fprintf(newf,"\n");

   if((Ele[i].mtl==1)||(Ele[i].mtl==2)) Mode=1;

   else Mode=0;

   for(k=0;k<NpE;k++) if(n12[OptND[Ele[i].node[k]]]==0)
n12[OptND[Ele[i].node[k]]]=Mode;

   }

/* Print node coordinates to the PLASTEX input file. */

   for(i=1;i<=NumNode;i++){

     printf(" %d    %f    %f \n",i,NewND[i].x,NewND[i].y);

     if(n12[i]==1) fprintf(n12f,"ND,  %d,  %f  %f \n",i,NewND[i].x,NewND[i].y);

   }

/* Print element to the N12 file. */

   for(i=1;i<=NumEle;i++){

     if((Ele[i].mtl==1)||(Ele[i].mtl==2)){

       fprintf(n12f,"EL, %d, SF %d, %d",i+1,Ele[i].mtl,NpE);

       for(k=0;k<NpE;k++) fprintf(n12f," %d ",OptND[Ele[i].node[k]]);

       fprintf(n12f,"\n");

     }

   }

/* Print constrain conditions. */

   for(i=1;i<=MAXNODE;i++){

     if((Constrain[i].x==1)||(Constrain[i].y==1))
```

```
        printf("%d  %d %d   0.0   0.0\n",OptND[i],Constrain[i].x,Constrain[i].y);

    }

  printf("Material:\n");
/* Print pressure loads. */

  printf("Load title\n");

  printf("0 1 1\n");

  printf("180 1\n");

  printf("%d \n",NumPres);

  for(i=0;i<NumPres;i++){

    j=atoi(pel[i]);

    printf(" %d   ",j);

    switch(Face[i]){

      case 1: printf(" %d  %d \n",

                 OptND[Ele[j].node[1]], OptND[Ele[j].node[0]]);

              break;

      case 2: printf(" %d  %d \n",

                 OptND[Ele[j].node[2]], OptND[Ele[j].node[1]]);

              break;

      case 3: printf(" %d  %d \n",

                 OptND[Ele[j].node[3]], OptND[Ele[j].node[2]]);

              break;

      case 4: printf(" %d  %d \n",

                 OptND[Ele[j].node[0]], OptND[Ele[j].node[3]]);

              break;

    }

    printf("%s   0.0   %s   0.0\n",Pressure[i],Pressure[i]);

  }

  printf("%d*%f  %d*0.0\n", STEP_STATIC, 0.5, STEP_CREEP);

  printf("1.0e-03 20 1 3 3 0\n");

  fclose(inf);
```

```
   fclose(opf);

   fclose(newf);

   fclose(n12f);

}


int detJ(X,Y)

float X[3],Y[3];

{

   float J[2][2];

   J[0][0] = -X[0]+X[1]+X[2]-X[3];

   J[0][1] = -Y[0]+Y[1]+Y[2]-Y[3];

   J[1][0] = -X[0]-X[1]+X[2]+X[3];

   J[1][1] = -Y[0]-Y[1]+Y[2]+Y[3];

   return (J[0][0] * J[1][1] - J[1][0] * J[0][1])/4;

}
```

Appendix B

DEFOMESH.C

```c
#include <stdio.h>

#include <stdlib.h>

#include <string.h>

#include <process.h>


#define MAXNODE 2000

#define MAXELEM 2000


struct Node{

  float x,y;

};

struct Element{

 int node[4],mtl;

};


char modes[11][3]={"ND,", "EL,"};

FILE *newf,*dl2f,*plaf,*deff;


/* * * * * * * * * * * * * * * * * * * * * * * * * * * * * * * * * * * * * * *

 *                              DEFOMESH.C                                  *

 *                        -----  2D Version  -----                          *

 *                                                                          *

 *    Use:   DEFOMESH [COSMOS/M Problem Name]                               *

 *                                                                          *

 * * * * * * * * * * * * * * * * * * * * * * * * * * * * * * * * * * * * * * */
```

```
main(argc,argv)

int argc;

char *argv[];

{

   float Scale,dx,dy,d;

   int    Def12[MAXNODE],NumNode,NumEle,i,j,k,l,nnd,mode,MatlSet;

   char   new[13],d12[13],def[13],s[18],ch;

   struct Node Node[MAXNODE],Disp[MAXNODE];

   struct Element Ele[MAXELEM];

   strcpy(new,argv[1]);

   strcat(new,".NEW");

   if((newf=fopen(new,"r"))==NULL){

      printf("Can't open %s",new[1]);

      exit(1);

   }

   strcpy(d12,argv[1]);

   strcat(d12,".D12");

   if((d12f=fopen(d12,"w"))==NULL){

      printf("Can't open %s",d12[1]);

      exit(1);

   }

   if((plaf=fopen("plas.cos","r"))==NULL){

      printf("Can't open PLAS.COS.");

      exit(1);

   }

   strcpy(def,argv[1]);

   strcat(def,".DEF");

   if((deff=fopen(def,"w"))==NULL){

      printf("Can't open %s",def[1]);

      exit(1);
```

```
}

for(i=0;i<MAXNODE;i++){

   Node[i].x=0;

   Node[i].y=0;

   Def12[i]=0;

}

MatlSet=0;

NumNode=0;

NumEle=0;

while(fscanf(newf,"%s\n",s)!=EOF){

   mode=99;

   for(i=0;i<2;i++){

      if(strcmp(s,&modes[i][0])==NULL) mode=i;

   }

   switch(mode){

      case 0: fscanf(newf,"%d",&i);

              fscanf(newf,"%c",ch);

              fscanf(newf,"%f %f",&Node[NumNode].x,&Node[NumNode].y);

              NumNode++;

              break;

      case 1: fscanf(newf,"%d %c %s %d %c %d",&j,ch,s,&k,ch,&nnd);

              Ele[NumEle].mtl=k;

              for(i=0;i<nnd;i++) fscanf(newf,"%d",&Ele[NumEle].node[i]);

              NumEle++;

              break;

   }

}

fscanf(plaf,"%d %d %d",&NumNode,&j,&j);

for(i=0;i<j;i++) fscanf(plaf,"%s",s);

for(i=0;i<NumNode;i++){
```

```
      fscanf(plaf,"%d %f %f",&k,&Disp[i].x,&Disp[i].y);

      for(k=0;k<j-2;k++) fscanf(plaf,"%f",&d);

   }

   for(i=0;i<NumEle;i++){

      if((Ele[i].mtl==1)||(Ele[i].mtl==2)) mode=1;

      else mode=0;

      for(k=0;k<nnd;k++){

         j=Ele[i].node[k]-1;

         if(Def12[j]==0) Def12[j]=mode;

      }

   }

   Scale=100;

   fprintf(deff,"ACTSET CS 0\n");

   fprintf(d12f,"ACTSET CS 0\n");
/* Offset and print deformed node coordinates to the DEF file. */
   for(i=0;i<NumNode;i++){

      fprintf(deff,"ND, %d, %f %f \n",

         i+1+NumNode,Node[i].x+Scale*Disp[i].x,Node[i].y+Scale*Disp[i].y);

      if(Def12[i]==1)

         fprintf(d12f,"ND, %d, %f %f \n",

         i+1+NumNode,Node[i].x+Scale*Disp[i].x,Node[i].y+Scale*Disp[i].y);

   }

/* Offset and print element nodal order.*/
   for(i=0;i<NumEle;i++){

      fprintf(deff,"EL, %d, SF %d, %d  %d %d %d %d\n",

            i+1+NumEle, Ele[i].mtl, nnd,

      NumNode+Ele[i].node[0],NumNode+Ele[i].node[1],

      NumNode+Ele[i].node[2],NumNode+Ele[i].node[3]);

      if((Ele[i].mtl==1)||(Ele[i].mtl==2)){

      fprintf(d12f,"EL, %d, SF %d, %d",i+1+NumEle,Ele[i].mtl,nnd);
```

```
        for(k=0;k<nnd;k++) fprintf(d12f," %d ",NumNode+Ele[i].node[k]);

        fprintf(d12f,"\n");

        }

    }

    fclose(newf);

    fclose(plaf);

    fclose(d12f);

    fclose(deff);

}
```

References

Albert, P., and Raphael, S., 1987, Alkali-Silica Reactivity in the Beauharnois Powerhouses, Beauharnois, in Grattan-Bellew, P.E. (ed.), *Concrete Alkali-Aggregate Reaction*, Grattan-Bellew, Noyes, Park Ridge, pp. 10 - 16.

Anon, 1989, Dam Replacement and Powerplant Uprating at Maentwrog, UK, *International Water Power and Dam Construction*, Vol. 41, No. 10, pp. 53 - 54, 56.

Bangash, M.Y.H., 1989, *Concrete and Concrete Structures: Numerical Modeling and Applications*, Elsevier Applied Science, London.

Bathe, K.-J., 1982, *Finite Element Procedures in Engineering Analysis*, Prentice-Hall, Englewood Cliffs.

Blacker, T.D., and Stephenson, M.B., 1991, Paving: A New Approach to the Development of Automatic Quadrilateral Mesh Generation, *International Journal for Numerical Methods in Engineering*, Vol. 32, No. 4, pp. 811 - 847.

Blacker, T.D., Meyers, R.J., 1993, Seams and Wedges in Plastering: A 3D Hexahedral Mesh Generation Algorithm, *Engineering with Computer*, Spring Verlag, Vol. 2, No. 9, pp. 83 - 93.

Blight, G.E., Alexander, M.G., Ralph, T.K., and Lewis, B.A., 1989, Effect of Alkali-Aggregate Reaction on the Performance of a Reinforced Concrete Structure over a Six-Year Period, *Magazine of Concrete Research*, Vol. 41, No. 147, pp. 69 - 77.

Bonzel, V.J., and Dahms, J., 1973, Alkalireaktion im Beton, *Beton*, Vol. 23, No. 11, P. 495, Vol. 23, No. 12, P. 547.

Carey, G.F., and Oden, J.T., 1984, *Finite Elements: Computational Aspects, Volume III*, Prentice-Hall, Englewood Cliff.

Cass, R.J., Benzley, S.E., Mayers, R., and Blacker, T.D., 1996, Generalized 3-D Paving: An Automated Quadrilateral Surface Mesh Generation Algorithm, *International Journal for Numerical Methods in Engineering*, Vol. 39, No. 9, pp. 1475 - 1489.

Cervera, M., Oliver, J., and Galindo, M., 1992, Numerical Analysis of Dams with Extensive Cracking Resulting from Concrete Hydration: Simulation of a Real Case, *Dam Engineering*, Vol. 3, No. 1, pp. 1 -22.

Cervera, M., Oliver, J., Herrero, E., and Onate, E., 1990, A Computational Model for Progressive Cracking in Large Dams Due to the Swelling of Concrete, *Engineering Fracture Mechanics*, Vol. 35, Nos. 1/2/3, pp. 537 - 585.

Chatteryi, S., and Christensen, P., 1990, Studies of Alkali-Silica Reaction. Part 7. Modeling of Expansion, *Cement and Concrete Research*, Vol. 20, No. 2, Pergamon, pp. 285 - 290.

Chen, W.F., 1982, *Plasticity in Reinforced Concrete*, McGraw-Hill, New York.

Chen, W.F. , Han, D.J., 1988, *Plasticity for Structural Engineers*, Springer-Verlag, New York.

Clark, L.A., 1991, Modeling the Structural Effects of Alkali-Aggregate Reactions on Reinforced Concrete, *ACI Material Journal*, March - June, pp. 271 - 277.

Clark, L.A., 1993, Assessment of Concrete Bridges with ASR, in *Bridge Management 2: Inspection, Maintenance Assessment and Repair. Papers Presented at the Second International Conference on Bridge Management Held 18 -21 April 1993, University of Surrey*, Thomas Telford.

Curtil, L., and Habita, M.F., 1994, Study of the Alkali-Aggregate Reaction on Concrete Prisms, *Cement and Concrete Research*, Vol. 24, No. 3, pp. 473 - 478.

Dahms, J., 1976, Influences on the Alkali-Aggregate Reaction under Field Conditions, *Proceedings of a Symposium on the Effect of Alkali on the Properties of Concrete*, London, September 1976, Wexham Springs, Cement & Concrete Association, P. 277.

Danay, A., 1994, Structural Mechanics Methodology in Diagnosing and Assessing Long-Term Effects of Alkali-Aggregate Reactivity in Reinforced Concrete Structures, *ACI, Materials Journal*, Vol. 91, No. 1, January - February, 1994, pp. 54 -62.

Danay, A., Adeghe, L., and Hindy, A., 1993, Diagnosis of the Cause of the Progressive Concrete Deformations at Saunders Dam, *Concrete International, ACI*, Vol. 15, No. 9, pp. 25 - 35.

Davis, C.E., 1957, Studies in Cement-Aggregate Reaction, XXV: Comparison of the Expansions of Mortar and Concrete, *Australian Journal of Applied Science*, Vol. 8, No. 1, P. 222.

Desai, C.S., and Siriwardane, H.J., 1984, *Constitutive Laws for Engineering Materials*, Prentice-Hall, Englewood Cliffs.

Diamond, S., Barneyback, R.S. Jr, and Struble, L.J., 1981, On the Physics and Chemistry of Alkali-Silica Reactions, *Proceedings of 5th International Conference on Alkali-aggregate Reaction in Concrete, S252/22*, Cape Town, National Building Research Institute, pp. 1 - 11.

Fournier, B., Berube, M.A., and Vezina, D., 1988, Condition Survey of Concrete Structures Built with Potentially Alkali-Reactive Limestone Aggregate from the Quebec City Area, *RTAC 1988 Annual Conference Proceedings*, Transport and Road Research Laboratory, Road and Transportation Association of Canada.

Gillott, J.E, and Rogers, C.A., 1994, Alkali-Aggregate Reaction and Internal Release of Alkalis, *Magazine of Concrete Research*, Vol. 46, No. 167, pp. 99 - 112.

Gillott, J.E., and Soles, J.A., 1993, Petrography of Concrete Cores from New Brunswick, Relating to the Durability Problem, *Cement & Concrete Composites*, Vol. 15, No. 1-2, pp. 101 - 114.

Gocevski, V., 1993, *Modernisation des infrastructures et des travaux connexs, Centrale Beauharnois avant-projet, Partie 1*, TLABA-904-099, Hydro-Quebec.

Grattan, P.E., 1981, Canadian Experience of Alkali-Expansivity in Concrete, *Proceeding of the 5th International Conference on Alkali-aggregate Reaction in Concrete, Cape Town, March 30 - April 3*, National Building Research Institute.

Hamilton, C.H., 1995, Surveying the Field of FEA Modelers, *Computer-Aided Engineering*, Vol. 14, No. 6, pp. 30, 32, 36 - 37, 40.

Haavik, D.J., and Mielenz, R.C., 1991, Alkali-Silica Reaction causes Concrete Pipe to Collapse, *Concrete International*, Vol. 13, No. 5, ACI, pp. 54 - 57.

Hobbs, D.W., 1984, Expansion of Concrete due to Alkali-Silica Reaction, *The Structural Engineer*, Vol. 62, No. 1, pp. 26 - 34.

Hobbs, D.W., 1988, *Alkali-Silica Reaction in Concrete*, Thomas Telford, London.

Hobbs, D.W., 1990, Cracking and Expansion Due to the Alkali-Silica Reaction: Its Effect on Concrete, *Structural Engineering Review*, Vol. 2, pp. 65 - 79

Hobbs, D.W., 1990, Alkali-Silica Reaction: Its Effect on Concrete Members and Structures, in *Developments in Structural Engineering, Proceedings of the Forth Rail*

Bridge Centenary Conference, Heriot-Watt University, Endinburgh, Scotland, August 21 - 23. Vols. 1 and 2, Spon.

Hoffmann, C.M., 1989, *Geometric and Solid Modeling: An Introduction*, Morgan Kaufmann, San Mateo Calif.

Huang, M., Pietruszczak, S., 1996, Numerical Analysis of Concrete Structures Subjected to Alkali-Aggregate Reaction, *Mechanics of Cohesive-Frictional Materials*, Vol. 1, Num. 4, pp. 305 - 319.

Imai, H., Yamasaki, T., and Maehara, H., 1986, The Deterioration be Alkali-Silica Reaction in Hanshin Expressway Concrete Structures: Investigation and Repair, *Proceeding of 7th International Conference on Concrete Alkali-Aggregate Reactions*, Ottawa, Canada, pp. 131 - 135.

Jiang, J., and Pietruszczak, S., 1988, Convexity of Yield Loci for Pressure Sensitive Materials, *Computers and Geotechnics*, Vol. 5, No. 1, pp. 51 - 63.

Jones, A.E.K., Clark, L.A., and Amasaki, S., 1994, The Suitability of Cores in Predicting the Behaviour of Structural Members Suffering from ASR, *Magazine of Concrete Research*, Vol. 46, No. 167, pp. 145 - 150.

Kennerley, R.A., St John, D., and Smith, L.M., 1981, A Review of Thirty Years of Investigation of Alkali-Aggregate Reaction in New Zeeland, in *Proceeding of the 5th International Conference on Alkali-aggregate Reaction in Concrete*, Cape Town, March 30 - April 3, National Building Research Institute, pp. 1 - 10.

Kladek, I., Pietruszczak, S., and Gocevski, V., 1995, Modelling of Mechanical Effect of Alkali-Silica Reaction in Beauharnois Powerhouse, in: Pande, G.N., and Pietruszczak, S. (eds.), *Proceedings of 5th International Symposium on Numerical Models in Geomechanics - NUMOG*, Davos, Switzerland, pp. 639 - 644.

Kordina, K., and Schwick, W., 1981, Investigation on Additives to Concrete for Prevention of Alkali-Aggregate Reaction, *Betonwerk und Fertigteil-Technik*, Vol. 47, No. 6, P. 328.

Lai, Y.-C., Liang, T.C.S., and Jia, Z., 1992, Implementation of 0 and h-p Versions of the Finite Element Method, *Computer in Engineering, Volume 2, Proceedings of the 1992 ASME International Computers in Engineering Conference and Exposition*, August 2 - 6, San Francisco, ASME.

Leger, P., Cote, P., and Tinawi, R., 1995, Numerical Analysis of Concrete Dams Affected by Alkali-Aggregate Reactions, *Proceedings of International Symposium on Research and Development in the Field of Dams*, Switzerland, September 7 - 9, pp. 323 - 334.

Leger, P., Tinawi, R., and Mounzer, N., 1995, Numerical Simulation of Concrete Expansion in Concrete Dams Affected by Alkali-Aggregate Reaction: State-of-the-Art, *Canadian Journal of Civil Engineering*, Vol. 22, No. 4, pp. 692 - 713.

Leger, P., Venturelli, J., and Bhattacharjee, S. S.,1993, Seasonal Temperature and Stress Distribution in Concrete gravity Dams. Part 1: Modelling, *Canadian Journal of Civil Engineering*, Vol. 20, No. 4, pp. 999 - 1017.

Leger, P., Venturelli, J., and Bhattacharjee, S. S.,1993, Seasonal Temperature and Stress Distribution in Concrete gravity Dams. Part 2: Behaviour, *Canadian Journal of Civil Engineering*, Vol. 20, No. 4, pp. 1018 - 1029.

Magni, E.R., Rogers, C.A., and Grattan-Bellew, P.E., 1987, The Influence of the Alkali-Silicate Reaction on Structures in the Vicinity of Sudbury, Ontario, in Grattan-Bellew, P.E. (ed.), *Concrete Alkali-Aggregate Reaction*, Noyes, Park Ridge, pp. 17 - 22.

Mantyla, M., 1988, *An Introduction to Solid Modeling*, Computer Science Press, Rockville.

McLeish, A., 1990, Structural Implications of the Alkali Silica Reaction in Concrete, *TRRL Contractor Report, CR 177*, Transport and Road Research Laboratory, UK.

Newell,V.A., Tanner, D.T., and Wagner, C.D., 1994, Checking Concrete Growth, *Civil Engineering*, New York, Vol. 64, No. 1, pp. 70 - 72.

Nishibayasshi, S., Okada, K., Kawamura, M., Kobayashi, K., Kojima, T., Miyagawa, T., Nakano, K., and Ono, K., 1992, Alkali-Silica Reaction - Japanese Experience, in Swamy, R.N. (ed.), *The Alkali-Silica Reaction in Concrete*, Van Nostrand Reinhold, New York

Nixon, P.J., and Bollinghaus, R., 1985, The Effect of Alkali Aggregate Reaction on the Tensile and Compressive Strength of Concrete, *Durability of Building Materials*, Vol. 2, pp. 243-248.

Okada, K., Nishibayashi, S., and Kawamura, M. (eds.), 1989, *Alkali-Aggregate Reaction* , 8th International Conference, Kyoto, Elsevier Applied Science, London.

Olafsson, H., The Effect of Relative Humidity and Temperature on Alkali Expansion of Mortar Bars, in Gratten-Bellew, P.E. (ed.), *Concrete Alkali-aggregate Reaction*, Noyes Publications, Park Ridge, pp. 461 - 465.

Owen, D.R.J., and Hinton, E., 1980, *Finite Elements in Plasticity: Theory and Practice*, Pineridge, Swansea.

Pietruszczak, S., 1996, On the Mechanical Behaviour of Concrete Subjected to Alkali-Aggregate Reaction, *International Journal of Computer & Structures*, Vol. 58, No. 6, pp. 1093 - 1097.

Pietruszczak, S., Jiang, J., and Mirza, F.A. 1988, An Elastoplastic Constitutive Model for Concrete, *International Journal of Solids Structures*, Vol. 24, No. 7, pp. 705 - 722.

Pleau, R., Berube, M.A., Pigeon, M., Fournier, B., and Raphael, S., 1989, Mechanical Behavior of Concrete Affected by ASR, in Okada, K., Nishibayashi, S., Kawamura, M. (eds.), *Alkali-Aggregate Reaction, Proceedings of 8th International Conference on Alkali-Aggregate Reaction in Concrete*, Kyoto, Elsevier Applied Science, London, pp. 721 - 725.

Poole, A.B., 1992, Introduction to alkali-aggregate reaction in concrete, in Swamy, R.N. (ed.), *The Alkali-Silica Reaction in Concrete*, Van Nostrand Reinhold, New York, pp. 8 - 75.

Prevost, J.H., 1987, Modeling the Behavior of Geomaterial, in Sayed, M.S. (ed.), *Geotechnical Modeling and Applications*, Gulf, Houston.

Rogers, C.A., 1987, Alkali-Aggregate Reactivity in Ontario, in Grattan-Bellew, P.E. (ed.), *Concrete Alkali-Aggregate Reaction*, Noyes, Park Ridge, pp. 5 - 9.

Rogers, C.A., 1993, Alkali-Aggregate Reactivity in Canada, *Cement & Concrete Composites*, Vol. 15, No. 1-2, pp. 13 - 19.

Rotter, H.M., 1995, *Alkali-Aggregate Reaction: From Basic Principles to Structural Behaviour - A Literature Review*, Ecole Polytechnique, Montreal.

Schnelders, R., 1995, A Grid-Based Algorithm for the Generation of Hexahedral Element Meshes, *Engineering with Computers*, Feb. 1995.

Shayan, A., 1989, Re-Examination of AAR in an Old Concrete, *Cement and Concrete Research*, Vol. 19, No. 3, pp. 434 - 442.

Shayan, A., and Quick, G.W., 1992, Microscopic Features of Cracked and Uncracked Concrete Railway Sleepers, *Cement & Concrete Composites*, Vol. 89, No. 4, pp. 348 - 361.

Shephard, M.S., and Yerry, M.A., 1984, Finite Element Mesh Generation for Use with Solid Modeling and Adaptive Analysis, in Pickett, M.S. and Boyse, J.W., (eds.) *Solid Modeling by Computers, From Theory to Applications*, Plenum Press, New York.

Stanton, D.E., 1940, The Expansion of Concrete though Reaction between Cement and Aggregate, *Preceedings of the American Society of Civil Engineering*, Vol. 66, pp. 1781 - 1811.

Stark, D., 1985, *Alkali-Silica Reactivity in Five Dams in Southwestern United States*, United States Department of the Interior, Bureau of Reclamation, Engineering and Research Center.

Structural Research & Analysis Corp., 1994, *COSMOS/M UserGuide, Vol. 1*, 2nd Edition, Santa Monica.

Structural Research & Analysis Corp., 1994, *COSMOS/M Command Reference*, Vol. 2, 2nd Edition, Santa Monica.

Structural Research & Analysis Corp., 1994, *COSMOS/M basic FEA System UserGuide Part 1, Vol. 3*, 2nd Edition, Santa Monica.

Structural Research & Analysis Corp., 1994, *COSMOS/M Advanced Modules User Guide, Part 1, Vol. 4*, 2nd Edition, Santa Monica.

Swamy, R.N. (ed), 1992, *The Alkali-Silica Reaction in Concrete*, Van Nostrand Reinhold, New York

Swamy, R.N., and Al-Asali, 1988, Expansion of Concrete Due to Alkali-Silica Reaction, *ACI Materials Journal*, Vol. 85, No. 1, pp. 33 - 40.

Swamy, R.N., and Al-Asali, 1988, Engineering Properties of Concrete Affected by Alkali-Silica Reaction, *ACI Materials Journal*, Vol. 85, No. 5, pp. 367 - 374.

Talbert, J.A. and Parkinson, A.R., 1990, Development of an automatic two-dimensional finite element mesh generator using quadrilateral elements and Bezier curve boundary definition. *International Journal for Numerical Methods in Engineering*, Vol. 29, pp. 1551 - 1567.

Tautges, T.J., Mitchell, S.A., 1996, Progress Report on the Whisker Weaving All-Hexahedral Meshing Algorithm, *5th International Conference on Numerical Grid Generation in Computational Field Simulations*, Mississippi State University, pp. 659 - 670.

The Institution of Structural Engineers, 1992, *Structural Effects of Alkali-Silica Reaction, Technical Guidance on the Appraisal of Existing Structures*, The Institution of Structural Engineers, London.

Vivian, H.E., 1950, Studies in Cement-Aggregate Reaction, Parts X to XV, CSIRO, Australia, *Bulletin* No. 256, P. 13.

Weller, F., Schindler, R., Schnelders, R., 1996, Automatic Geometry-Adaptive Generation of Quadrilateral and Hexahedral Element Meshes for FEM, *5th International Conference on Numerical Grid Generation in Computational field Simulations*, Mississippi State University, pp. 689 -697.

Wesley, M.A., and Markowsky, G., 1984, Generation of Solid Models from Two-Dimensional and Three-dimensional Data, in Pickett, M.S. and Boyse, J.W., (eds.) *Solid Modeling by Computers, From Theory to Applications*, Plenum Press, New York.

Wood, J.G.M., Young, J.S., and Ward, D.E., 1986, The Structural Effects of Alkali-Aggregate Reaction on Reinforced Concrete, *Proceeding of 7th International Conference on Concrete Alkali-Aggregate Reactions*, Ottawa, Canada, pp. 157 - 162.

Xin, D., Zollinger, D.G., and James, R.W., 1992, One-Dimensional Model for Analysis of CRC Pavement Growth, *Journal of Transportation Engineering*, Vol. 118, No. 4, ASCE, pp. 557 - 575.

Xu, Z., and Hooton, R.D., 1993, Migration of Alkali ions in Mortar due to Several Mechanisms, *Cement & Concrete Composites*, Vol. 23, No. 4, pp. 951 - 961.

Yeh, C.H., Zipparro, V.J., Kaltsouni, M., Wagner, C., and Niznik, J., 1993, Fontana Emergency Spillway, Case Study, *International Workshop on Dam Safety Evaluation*, Grindelwald, Switzerland, April 26 - 28, Vol. 1, pp. 187 - 198.

Zienkiewicz, O.C., and Taylor, R.L., 1983, *The Finite Element Method*, 4th Edition, Vol. 2, McGraw-Hill, London.